Alma Mater Studiorum · University of Bologna

School of Science
Department of Physics and Astronomy
Master Degree in Physics

Commissioning of the third n_TOF spallation target: characterization of the neutron flux and beam profile using PPACs

Supervisor:
Prof. Cristian Massimi

Co-supervisor:
Dr. Alice Manna

Submitted by:
Michele Spelta

Academic Year 2020/2021

Abstract

Beyond their application in fundamental nuclear physics and nuclear astrophysics research, neutron-induced reactions play an increasingly important role in emerging nuclear technologies. For instance, in the fields of sustainable low-carbon power production (ADS, generation four fission and fusion reactors), medicine and industry, neutron data are required with high accuracy in a wide energy range. The measurement of neutron-induced reaction cross sections is therefore crucial and it is indeed the main objective of the n_TOF facility, a pulsed white neutron spallation source at CERN.

Recently the facility has been upgraded with the installation of its new third-generation spallation target and a subsequent commissioning was carried out in order to characterize the performances of the experimental areas in terms of neutron flux, energy resolution and background in view of the future experimental campaigns.

I was involved in the first phase of the commissioning at CERN, testing the DAQ system and taking care in particular of one of the employed detectors: a fission chamber based on Parallel Plate Avalanche Counters (PPACs). The data collected in the first experimental area (EAR1) were analyzed to obtain the neutron flux from near thermal energy (0.025 eV) to 1 GeV and the spatial beam profile. The flux from the present analysis is compared to the Monte Carlo simulations and to the preliminary results of another flux detector, while the spatial beam profile is compared to the one obtained with a Timepix Quad detector. In addition, a preliminary analysis of the data collected in the second experimental area (EAR2) was also carried out.

Un grazie particolare al Prof. Massimi e ad Alice, a Simone, Alberto e a tutto il local team di n_TOF al CERN.

Contents

Introduction

Neutron-induced reactions represent an important class of nuclear reactions and are discussed in the first chapter of this thesis. Since neutrons directly interact with the atomic nuclei at whatever kinetic energy, after their discovery neutron-induced reactions were soon exploited in fundamental research in nuclear physics and in the synthesis of artificial radioisotopes. Currently, they find application in a broad variety of research fields, ranging from nuclear astrophysics to industry and medicine. Some of these applications are described with a particular emphasis on the emerging nuclear technologies for power production and nuclear waste management, such as IV generation fission reactors and ADS (Accelerator Driven Systems), very current issues to face the increasing demand for sustainable low-carbon electricity generation. All these applications rely on the accurate knowledge of the neutron-induced reaction cross sections, that describe the probability for the reactions to occur. Operational and theoretical definitions, simple models for their calculation, a description of their energy dependence and notable examples are also included in Chapter 1.

Neutron cross section data are sometimes scarce and not so accurate especially at high energy, where their improvement is urgently required. Since nuclear theories cannot provide predictions with the required accuracy, their evaluation relies ultimately on the experiments carried out at the neutron time-of-flight facilities. Among them, the n_TOF facility at CERN is a notable example, operating since 2001.

Here, the spallation of high energy protons induced in a lead massive target produces a large number of neutrons collimated towards two different experimental areas (EAR1 and EAR2), where the time-of-flight technique is used to accurately measure neutron-induced reaction cross sections as a function of the neutron kinetic energy. In particular, the combination of its extremely wide neutron energy distribution, its high instantaneous flux and its excellent energy resolution makes n_TOF unique and one of the most active neutron facilities worldwide. Its detailed description is the topic of the second chapter.

During the last CERN long shutdown the previous spallation target, come to the end of its scheduled lifetime, was replaced with a new-generation nitrogen-

cooled one, designed in order to solve the problems of erosion-corrosion and water contamination occurred in the past. In addition, it was conceived to improve even more the performance of the facility, especially in the second experimental area. This work deals in particular with the subsequent commissioning, planned in order to characterize the new neutron beams in both the experimental areas in terms of neutron flux, beam profile, energy resolution and background in view of the future experimental campaigns. The third chapter, after a general introduction about neutron detection and flux measurements, provides a detailed description of the experimental setup and of the detectors employed in the commissioning. A particular attention is devoted to the description of the PPAC Monitor, a fission chamber based on Parallel Plate Avalanche Counters (PPACs) that enables the measurement of the neutron flux and the determination of the beam profile in a wide energy region (from meV to GeV).

The analysis of the data from this detector in the first experimental area is the topic of the fourth chapter. The different steps in the data analysis are accurately discussed and the resulting neutron flux and spatial beam profile in EAR1 are presented. The neutron flux is compared to the Monte Carlo simulations and to the results from another flux detector (SiMon), while the spatial beam profile is compared to the one obtained with a Timepix Quad detector during the beam-detector alignment procedures. A preliminary analysis of the data collected in the second experimental area (EAR2) is also carried out and the resulting neutron flux and spatial beam profile are presented as well, together with the aforementioned comparisons.

Chapter 1

Neutron physics and applications

The first hypothesis about the existence of the neutron was suggested by E. Rutherford in 1920 in his Bakerian lecture about the nuclear constitution of atoms [1]. At that time the atomic nucleus was supposed to be "built up ultimately by hydrogen nuclei and electrons" [1] held together by a very strong force. Protons were indeed found to be ejected from the nuclear fragmentation induced by α particle bombardment (Rutherford, 1919 [2]), while the nuclear electrons were assumed to bound the nucleus, to provide the right nuclear electric charge and to explain the beta radioactivity.

However, in similar experiments, Rutherford observed that the fragmentation of some nuclei (specifically oxygen and nitrogen) seemed to eject an apparent new particle with A=3 and Z=2, interpreted as a particular stable compound of three protons and a nuclear electron. Even if this apparent discovery turned out to be false some years later, it led Rutherford to suggest the existence of secondary fundamental nuclear units made of particularly stable combinations of protons and nuclear electrons besides the already known α particles. In particular, the existence of a so-called *neutron* was suggested: a "neutral doublet" composed of an electron and a proton closely coupled, deemed necessary for the synthesis of heavy nuclei in stars [1].

However, this prediction was not widely accepted and thus ignored by many scientists as W. Bothe, H. Becker, I. Curie and F. Joliot who first unwittingly observed the neutron [3].

In fact, in 1930 Bothe and Becker observed a very penetrating *secondary radiation* emitted by beryllium when bombarded by alpha particles [4], but they wrongly interpreted it as very high energy γ rays emitted after the capture of the α particles to release the exceeding binding energy. Curie and Joliot further observed that this secondary radiation was able to knock protons out from hydrogenous material (specifically paraffin). Exploiting this phenomenon ascribed to Compton scattering, they estimated the energy of the assumed photons emitted

by beryllium to be approximately 50 MeV [5].

In this way, a contradiction was found: 50 MeV photons could not be produced after the α capture in beryllium since the Q-value of the reaction is only 10.6 MeV. J. Chadwick, a Rutherford's collaborator and thus well aware of the neutron hypothesis, soon pieced together all these information, recognized the contradiction and correctly identified the *secondary radiation* with neutrons emitted from beryllium according to $\alpha + {}^{9}Be \rightarrow {}^{12}C + n$ [6, 7]. In this way the high penetration power was still guaranteed by the particle neutrality and the proton recoil in paraffin could be also consistently explained in terms of collision between massive particles.

Neutrons were later assumed to be elementary particles and took the place of nuclear electrons, definitely abandoned, as nuclear constituents.

Moreover, because of their neutrality neutrons interact directly with the nuclei at whatever energy since they were unaffected by the Coulomb barrier. Therefore, soon after their discovery neutrons were employed to investigate the nuclear structure, test nuclear models and artificially synthesize new radioactive isotopes, eventually leading to the discovery of neutron induced fission. Primarily for this reason a broad field of *neutron physics* was born, contrasted to which an equally wide field of proton physics cannot exist [8].

1.1 Interaction of neutrons

Neutron physics has been roughly defined by P. Reuss as "the study of the travel of neutrons through matter" and their resulting interactions [9]. As previously mentioned, because of their neutrality neutrons are unaffected by the electric interaction responsible for both the particle interaction with electrons and the potential barrier surrounding the charged nucleus. This is the reason for the two main distinctive features of neutron interactions: they involve almost exclusively atomic nuclei and at whatever energy, even at very low one. On one side, the exclusive interaction with nuclei, five orders of magnitude smaller than atoms, implies the great penetrability of neutrons in matter. On the other side, the wide energy range over which they can cause nuclear interaction accounts for the variety of phenomena occurring in their interaction with matter.

As a matter of fact, from quantum mechanics, a neutron impinging on matter can be associated to a wavelength depending on the inverse of its momentum p, $\lambda = h/p$. When the neutron has energy lower than 50 MeV, its wavelength is larger or comparable at most with the nuclear dimensions and thus it interacts with the nucleus as a whole. In this situation it can be absorbed and share its energy with all the nucleons creating a new unstable *compound nucleus* or it can be scattered by the nuclear potential in the process called *potential* or *shape elastic scattering*.

In this second case, the scattered neutrons can undergo interference and produce diffraction patterns that are the realm of *neutron optics*.

In particular, when the neutron energy is very low, between some tenths and some tens of meV (the so-called cold and thermal neutrons), their wavelenghts are so large (around 10^{-10} m) to be comparable even with the inter-atomic distances in crystals and molecules and to make neutron diffraction capable of providing information on the atomic structures [8].

On the other hand, increasing the energy above 50 MeV (the so called *relativistic* or *high energy neutrons*), the neutron wavelength decreases well below the dimension of the nucleus until it becomes similar to the dimension of nucleons (around 1 fm). Thus, neutrons do not interact with the whole nucleus, but only with a portion or even with a single nucleon: these are the so-called *direct* or *peripheral reactions*.

Going on increasing the energy of the neutron above some GeV, the wavelength becomes so small that the internal structure of nucleons becomes relevant. In other words, interactions must be thought in terms of quarks and gluons, but this mechanism is beyond the aim of this work.

1.1.1 Compound nucleus reactions

The *compound nucleus* model was the first theory for nuclear reactions, suggested by N. Bohr in 1936 [10, 11]. Its basic assumption is that reactions proceed through two independent steps: the fusion of the incoming neutron n and the target nucleus A in an excited intermediate state C^* (the *compound nucleus*) and its subsequent de-excitation through the emission of radiation or particles b. This can be written as:

$$A + n \longrightarrow C^* \longrightarrow b + B.$$

More in details, the incoming neutron entering the nucleus undergoes several collisions with the single nucleons, transferring part of its kinetic energy in each of them until it is trapped in the nucleus as well. In turn, the excited nucleons collide with the neighbours transferring part of the excitation. Eventually, the kinetic energy of the incoming neutron is completely shared among all the nucleons so that none has a sufficient energy to escape and the identity of the impinging neutron is completely lost.

The result, as anticipated, is the formation of a compound nucleus that has one neutron more than the original target nucleus and lies in an excited state whose energy corresponds to the sum of the binding energy of the neutron (between 5 and 8 MeV depending on the nucleus) and its initial kinetic energy.

The compound nucleus is therefore unstable and its decay represents the second step of the reaction mechanism. It has some important properties.

Firstly, the compound nucleus mean lifetime is some order of magnitudes longer than the 10^{-22} s *characteristic nuclear time*, defined as the time necessary for a few MeV neutron to cross a medium-weight nucleus. This implies a relatively long time duration of the compound-nucleus reactions, that ranges from 10^{-18} s to 10^{-16} s and is one of their distinctive features.

Secondly, since the impinging neutron loses its identity, the compound nucleus has no memory of the entrance channel of the reaction, except of course for the quantities that have to be conserved in the reaction such as energy, total angular momentum, parity and the number of protons and neutrons (separately conserved at least for the low energies the model deals with). This implies that the relative probability for the compound nucleus to decay in a particular output channel is independent of the way it was formed. Two other typical properties of compound-nucleus reactions result as consequence. One is the isotropic angular distribution in the center of mass frame of the particles eventually emitted by the de-excitation, just as in the decay of an isolated nucleus. The other, anticipating the subject of the next section, is the possibility of factorizing the cross section of compound-nucleus reactions in two independent terms: the cross section for the formation of the compound nucleus from the entrance channel of the reaction $\sigma_{IN,C}$ and the probability for the compound nucleus to decay in a particular output channel $\sigma_{C,OUT}$:

$$\sigma_{IN,OUT} = \sigma_{IN,C} \cdot \sigma_{C,OUT}.$$

The last term can be further written as the ratio between the width of the particular output channel Γ_{OUT} and the total width of the compound nucleus Γ according to

$$\sigma_{C,OUT} = \Gamma_{OUT}/\Gamma = \Gamma_{OUT}/\sum_{pos}\Gamma_{pos},$$

explicitly showing all the competing output channels *pos* that result from the different decay modes of the compound nucleus.

De-excitation of the compound nucleus

Among the different competing de-excitation processes, the most likely, especially at higher energies [12], is the re-emission of nucleons. In fact, as the impinging neutron shares its energy among all the nucleons through successive collisions, it can happen that in the same way the extra energy is re-concentrated in a single or a group of nucleons that are enabled to escape the nucleus carrying away part of its excitation energy. This mechanism is described just as the evaporation of molecules from a hot liquid: it is indeed called *evaporation model* and it is studied with the same statistical formalism [13].

Additional proofs that this analogy is really appropriate can be found in the energy spectrum of the emitted neutrons shown in Figure 1.1 that clearly resem-

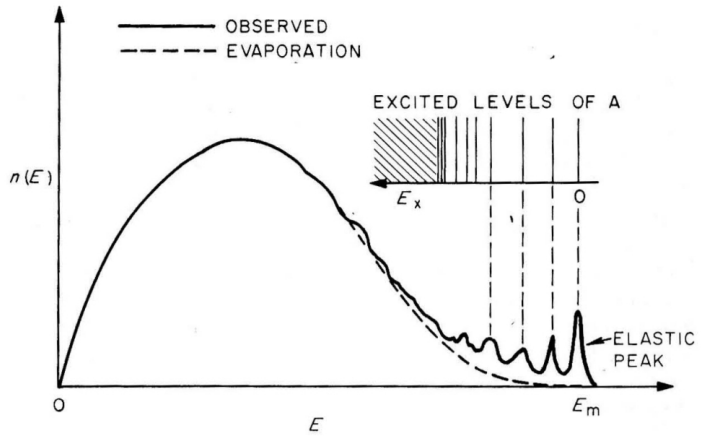

Figure 1.1: The energy spectrum of neutrons from the evaporation of the compound nucleus. While at low energy the classical maxwellian distribution is well reproduced, the high energy region of the spectrum is affected by the low-lying discrete excitation levels of the nucleus. From [14].

bles a Maxwellian distribution and in the fact that the more energy is given to the compound nucleus the higher is the number of particles expected to evaporate, see Figure 1.2.

The evaporated particles can be nucleons or even α particles, but neutrons are the most likely emitted, especially at low energies, since their emission is never prevented by the Coulomb barrier. In particular, when only one neutron is emitted the reaction is called *scattering*, or, more spefically including the reaction mechanism, *compound-nucleus scattering*. Furthermore, if the neutron is emitted with the maximum energy possible, that is an energy equal to that of the impinging neutron, the scattering is said to be *elastic*, otherwise it is called *inelastic* because it leaves the target nucleus in an excited state. However, scattering as well as charged-particle emission reactions do not occur exclusively as compound-nucleus reactions, as discussed later on.

Other possibilities for the de-excitation of the compound nucleus are the emission of γ radiation and fission. The former, referred to as *radiative capture reaction*, occurs at low energy where the discrete energy levels are relevant (see next paragraph). The γ spectrum resulting from these reactions is usually made of two components. The primary component consists of high energy (5-10 MeV) radiation that corresponds to the de-excitation from the capture state to the low-lying energy states. The secondary low energy component is due to de-excitation of the latter. Radiative capture reactions are particularly important to study the spin-parity and the energy of the nuclear excited states and to synthesize heavy nuclei and radioisotopes [15].

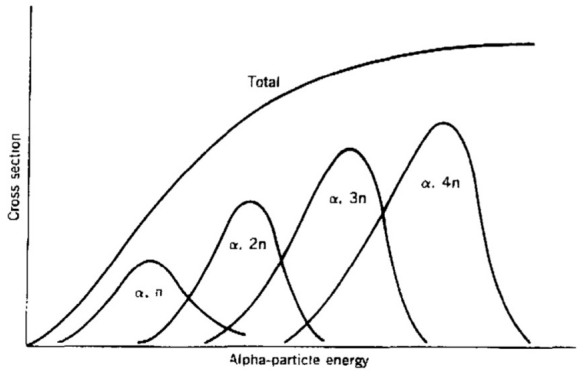

Figure 1.2: Cross sections for the evaporation of neutrons as function of the incident kinetic energy. Increasing the energy, a higher number of neutrons is likely to evaporate. The total evaporation cross section is also shown. From [15].

Fission occurs exclusively with some heavy nuclei and will be analyzed in details in the paragraph 1.1.3. At low energy, these two types of reaction proceed exclusively through the compound-nucleus model and they are the ones mostly studied at n_TOF.

Resonance reactions

An other important feature of the compound nucleus is that, from quantum mechanics, it cannot exist with an arbitrary energy content, but only in definite discrete energy states resulting from the solution of the Schrödinger equation in the nuclear potential well. Furthermore, since excited states are unstable, each level has a certain width related to the inverse of its average lifetime.

As shown in Figure 1.3, at low excitation energy the energy levels are well separated, but increasing the excitation energy they become closer and closer until their separation gets lower than their width: at this point the different states overlap creating a structureless continuum.

Thus, it is necessary to distinguish two energy regimes for the compound nucleus model. At high excitation energies, generally corresponding to kinetic energies of the impinging neutron higher than 10 - 100 keV for intermediate and heavy nuclei, the compound nucleus reaches the energy levels in the continuum region of its spectrum. In this case, the compound nucleus and its nucleons can assume whatever value in the energy continuum as in classical mechanics, thus both the analogy with evaporation and the statistical treatment of the de-excitation previously described make completely sense. This is called the *statistical compound nucleus model*.

However, as already shown in Figure 1.1, the predicted Maxwellian spectrum

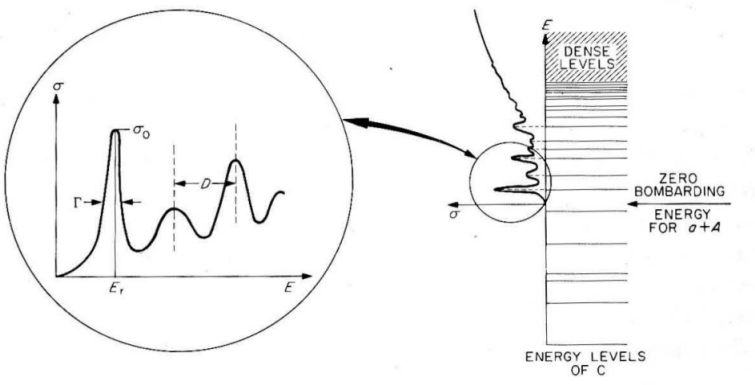

Figure 1.3: The energy spectrum of the compound nucleus excited states. At high energy their overlap creates a continuum, while at low energy the nuclear levels are well separated in a discrete spectrum. On the left the consequent effect on the compound nucleus reaction cross section, characterized by resonances. From [14].

is well reproduced only by the low-energy evaporated neutrons. The emission of high energy neutrons indeed de-excites the compound nucleus to the levels lower than the continuum band. Therefore, the emitted particles can assume only the energies matching these excitation levels and this explains the discrete peaks appearing in the spectrum.

This is similar to what happens at lower excitation energies. When the kinetic energy of the impinging neutron is lower than 10 - 100 keV only discrete energy levels are available for the excitation of the compound nucleus. Hence, only when the energy of the projectile matches one of these levels the compound nucleus can be formed and it is called *nuclear resonance*. For this reason, the corresponding reactions are called *resonance reactions* and their probability, as will be shown in the section 1.2.3, is characterized by sharp peaks with a characteristic shape and occurring at well defined energies. These nuclear states are unstable and eventually decay through the emission of a neutron (*resonance scattering*), a γ ray or fissioning; of course, the evaporation of more nucleons is prevented by the low energy available.

1.1.2 Direct reactions

At the very opposite side of compound-nucleus reactions, *direct reactions* dominate at energies above 20 - 50 MeV [15].

At those energies two points are important and influence the reaction mechanism: the neutron wavelength is definitely lower than the nuclear dimension and the nucleon-nucleon scattering cross section decreases. For its short wavelegth

the fast impinging neutrons are assumed to "see" the individual nucleons, but for the low cross section they have a low probability to interact with them. The result is that in many cases the projectile gets out from the target nucleus without interacting or after a small number of collisions with a few or even one single nucleon. In turn, if the struck nucleons receive a high energy they can leave the nucleus without interacting as well, otherwise they undergo multiple collisions and share the excitation with the whole nucleus [13].

Notable examples of direct reactions that can be induced by neutrons are *inelastic scattering*, *transfer reactions* and *knock-out reactions*. In particular, in *inelastic scattering* the impinging neutron gets out from the target nucleus leaving it in an excited state, in *transfer reactions* the neutron can typically strip a proton from the target nucleus, while in *knock-out reactions* it knocks out particles from the nucleus with three or more reaction products resulting.

The characteristics of the particles outgoing direct reactions can be used to study and characterize the low-lying excited states of the target nuclei, such as rotational and vibrational bands for what regards scattering [12]. Among these characteristics, the angular distribution deserves a special attention. In fact, it usually allows one to access information on the spin and parity of the excited states involved in the reaction. Moreover, it is typically sharply peaked in the forward direction and this is a very distinctive feature of direct reactions, opposed to the isotropic angular distribution resulting from the compound-nucleus mechanism. The other distinctive feature of direct reactions is their short duration, comparable with the characteristic nuclear time of 10^{-22} s since the reaction typically proceeds through just a very few collisions inside the nucleus.

Sharing these two common characteristics, *shape elastic scattering* or *potential scattering* can be also included among the direct reactions [13]. However, as the name suggests, in this case neutrons are thought to interact just with the nuclear potential without entering the nucleus, just as the collision with a hard sphere. Moreover, *shape elastic scattering* occurs at whatever impinging neutron energy.

1.1.3 Neutron induced fission

Neutron induced fission was already considered among the compound nucleus reactions, but it deserves a particular attention since it is the reaction exploited in this work to measure the neutron flux.

Fission was discovered by chance in the thirties. In those years E. Fermi and other scientists were bombarding uranium with neutrons in the attempt to produce transuranic elements, but surprisingly found the emission of lighter nuclei such as barium, the first recognized by O. Hahn and H. Strassmann. In order to explain these results L. Meitner and O. Frisch suggested nuclear fission [16].

Fission occurs roughly because of the competition between Coulomb repulsion and nuclear interaction. When a neutron is captured, a heavy nucleus gets excited and deformed until it splits into two lighter nuclei in order to release its excitation energy. Fission of heavy nuclei is indeed an exothermic process since the binding energy per nucleon decreases when the nuclear mass increases after ^{56}Fe. In particular, fission usually releases about 200 MeV energy mainly in the form of kinetic energy of the fission fragments.

However, a fission process occurs only if the fission fragments overcome (or tunnel according to a more refined theory) the nuclear Coulomb barrier and this is why fission usually needs an activation energy. In particular, *fissile* nuclei are those for which the neutron capture alone supplies the needed excitation energy: they can undergo fission with high probability even at thermal energy (as ^{235}U or ^{239}Pu). The other *fissionable* nuclei (i.e. that can undergo fission) may need some extra energy in the form of kinetic energy of the incoming neutron to supply the activation energy: this implies a neutron energy threshold under which fission cannot occur (as for ^{238}U) or is particularly improbable. In general, odd-neutron nuclei usually belong to the first category, while even-neutron nuclei to the second one because of the pairing effect [15].

The shell model modifies the shape of the fission barrier from a single barrier to a double-humped barrier as shown in Figure 1.4. This modification implies an increased probability of fission for the nuclei excited just above the bottom of the well between the humps because quantum tunneling becomes more probable through the two thinner barriers encountered. Moreover, the existence of excited states in the potential well between the humps also accounts for the *fission isomers*, isomeric states that, for the reasons already described, show unusually short half-lives for spontaneous fission.

The shell model also explains the mass distribution of the fission fragments, usually showing two peaks corresponding to a light fission fragment and a heavy fission fragment. Indeed, this latter lies in correspondence of the double magic number nuclei (Z=50 and N=82), particularly stable just according to the shell model. In the following it will be also useful to remember that the conservation of momentum implies the kinetic energy of the fission fragments to be inversely proportional to their mass.

In addition to fission fragments, prompt and delayed γ rays and fast neutrons (in number dependent on the fissioning nucleus and on energy) are also emitted in fission reactions. In particular, an average of about 2.4 prompt neutrons with a mean energy of 2 MeV are emitted per thermal fission in ^{235}U. The neutron yield slightly increases with the incident neutron energy, for instance it is 2.6 at 2 MeV. These neutrons are particularly important since, suitably moderated, enable the initiation of the chain reaction exploited both for power production (see section 1.3.1) and for nuclear weapons. Delayed neutrons are emitted in a definitely

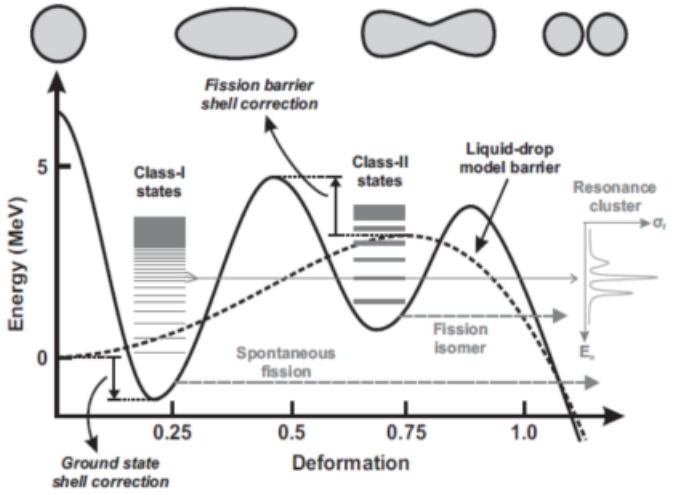

Figure 1.4: Sketch of the nuclear energy as a function of the deformation of a typical fissionable nucleus. The dashed line shows the "classical" single barrier, while the solid line shows the double-humped barrier predicted by the shell model and able to explain the existence of fission isomers. From [17].

lower number (about 0.016 per thermal fission in ^{235}U) by the de-excitation of some fission fragments and play a crucial role in the control of thermal reactors.

1.2 Neutron cross sections

In the previous section, reactions have been primarily classified according to their mechanism. However, describing some examples, another more immediate classification has been implicitly introduced, the one according to the output channels of the reactions. In fact, *elastic* and *inelastic scattering*, *fission* and *radiative neutron capture* reactions have been defined.

The important point outlined in this section is that each of these reactions occurs with a different probability that depends on the nucleus and on the excitation energy. *Cross sections*, and more specifically *neutron cross sections*, are exactly a measure of these probabilities of the different interactions of neutrons with matter. They are the very heart of neutron physics, in the sense that "the whole neutron physics is just the study of cross sections" [8]. In fact, since they can be measured through collision experiments on one side and theoretically deduced by assuming a particular nuclear model on the other, cross sections are the experimental quantitative way to access the inner structure of nuclei, hence a fundamental point of contact, comparison and test between experiments and nuclear theories.

1.2.1 Classical model

A simplified classical model for collisions can be used in order to give a formal and more rigorous definition of cross section [8]. Suppose to have a beam of monoenergetic neutrons of velocity v, volumetric density n' and transversal section A colliding with a thin target characterized by an areal density n, that is the number of nuclei per unit area. The neutron cross section σ, as its name suggests, is defined as the target area that each nucleus exposes perpendicularly to the approaching neutrons for the collision.

In particular, σ is said *total cross section* when it refers to a whatever kind of neutron-nucleus interaction, while if it refers only to a particular reaction it is called *partial cross section* for the reaction. The sum of all the partial cross sections is the total cross section, of course. What is said in the following, if not specified, can be applied to both, thus the terms "cross section" and "reaction" will be generally used.

According to this model, the number of neutrons per unit time involved in a particular reaction $\Delta N/\Delta t$ can be expressed as:

$$\frac{\Delta N}{\Delta t} = n'\, v \cdot n\, A \cdot \sigma, \tag{1.1}$$

where $n' \cdot v$ is the neutron flux Φ, i.e. the number of neutrons flowing across a unit area in the unit time. From the equation (1.1) the cross section can be expressed as:

$$\sigma = \frac{\Delta N}{\Delta t} \cdot \frac{1}{\Phi\, A\, n}. \tag{1.2}$$

This simple classical model cannot justify neither the dependence of the cross section on the energy of the projectile nor the huge diversity of its values for different close isotopes. Moreover, the values of the cross sections are often very different from the actual nuclear geometric dimensions. In fact, only a quantum mechanical treatment that considers the internal structure of nuclei will be able to explain these issues, as it will be shown.

Nevertheless, the simple formula (1.2) can be regarded as an "operational definition" of cross sections. Adding *a posteriori* the dependence on the energy of the incoming neutron, it is indeed largely used both for the experimental evaluation of cross sections and in the applicative fields of neutron physics.

Moreover, it also highlights the probabilistic interpretation of the cross section given in the first definition. As a matter of fact, if the equation (1.2) is restricted to one target nucleus only ($n = 1$) it just becomes the ratio between the number of neutrons involved in the considered reaction and the total number of incident neutrons. This ratio, in spite of being dimensionally an area, is the probability for a neutron sent on the nucleus to undergo the reaction.

1.2.2 Quantum model

The quantum mechanical treatment of cross sections [15, 18], as anticipated in the previous paragraph, is necessary to link them to the nuclear structure and thus to deduce them theoretically from the nuclear models, energy dependence included. Moreover, because of the the interpretation of quantum mechanics itself, it stresses even more the pure probabilistic meaning of cross sections, discussed just above.

In the collision model used in the previous paragraph, monoenergetic neutrons can be described now by a plane wave of wavenumber $k = p/\hbar$ assuming a neutron with momentum p hitting a target nucleus (both considered spinless for simplicity). the momentum of the neutron hitting with momentum p approaching a target nucleus, both considered spinless for simplicity. Assuming a central nuclear potential, the plane wave can be written in the *partial wave expansion* as:

$$\Psi_{in} = A\, e^{ikz} = A \sum_{l=0}^{\infty} i^l\, (2l+1)\, J_l(kr)\, P_l(\cos\theta), \tag{1.3}$$

where A is a normalization constant, l is related to the angular momentum of each partial wave, $P_l(\cos\theta)$ is the l-th Legendre polynomial and J_l is the Bessel function of order l. Using the asymptotic expansion of these latter, equation (1.3) can be rewritten as:

$$\Psi_{in} = A \sum_{l=0}^{\infty} i^{l+1}\, (2l+1) \frac{e^{-i(kr-l\frac{\pi}{2})} - e^{+i(kr-l\frac{\pi}{2})}}{2kr} P_l(\cos\theta) \tag{1.4}$$

in order to recognize, for each l, the combination of an incoming spherical wave converging on the target (e^{-ikr}/r) and an outgoing one emerging from it (e^{+ikr}/r). In this way, it is easy to consider the effect of the collision with the nucleus simply adding a complex coefficient η_l to the outgoing wave so that

$$\Psi_{out} = A \sum_{l=0}^{\infty} i^{l+1}\, (2l+1) \frac{e^{-i(kr-l\frac{\pi}{2})} - \eta_l\, e^{+i(kr-l\frac{\pi}{2})}}{2kr} P_l(\cos\theta). \tag{1.5}$$

The nucleus is indeed modelled as a localized perturbation and it can have two effects on the colliding neutron wave: change its phase or decrease its amplitude, effects respectively related to the phase and the module of the complex number η_l. However, at this point it is necessary to distinguish between *elastic scattering* and all the other possible reactions.

Elastic scattering cross section In the elastic scattering, assuming that the target nucleus is heavy enough to remain at rest, neutrons conserve their wavenumber: this means that the collision does not affect the amplitude of the incoming neutron wavefunction and η has unitary module.

Therefore, the elastic cross section can be computed using the definition (1.2) under the assumptions $n\,A = 1$ and substituting the total and the scattered numbers of neutrons per unit time respectively with the quantum incoming and scattered neutron current densities j computed as:

$$j = \frac{1}{2\,m\,i}\left(\Psi^* \frac{\partial \Psi}{\partial r} - \Psi \frac{\partial \Psi^*}{\partial r}\right), \tag{1.6}$$

where m is the neutron mass and Ψ is the incoming wavefunction of equation (1.4) in the first case and the scattered wavefunction in the second one. The latter can be obtained in turn from the difference between equations (1.5) and (1.4):

$$\Psi_{sc} = \Psi_{out} - \Psi_{in} = A\,\frac{e^{ikr}}{r}\left(\frac{1}{2k}\sum_{l=0}^{\infty} i\,(2l+1)\,(1-\eta_l)\,P_l(\cos\theta)\right), \tag{1.7}$$

where the terms in brackets is called *scattering amplitude* $f(\theta)$. Once integrated over the total solid angle, the elastic scattering cross section eventually results:

$$\sigma_{el} = \pi \lambda\!\!\!^{-2} \sum_{l=0}^{\infty} (2l+1)\,|1-\eta_l|^2, \tag{1.8}$$

where $\lambda\!\!\!^{-} = \lambda/2\pi = 1/k$ is the reduced neutron wavelength. Since, as discussed above, η_l has unitary module, it is conventionally written only in terms of a *phase shift* δ_l as $\eta_l = e^{2i\delta_l}$. Therefore, the equation (1.8) can be written equivalently as:

$$\sigma_{el} = 4\pi \lambda\!\!\!^{-2} \sum_{l=0}^{\infty} (2l+1)\,\sin^2\delta_l. \tag{1.9}$$

Non elastic cross section For all the other non elastic reations, neutrons change their energy or are absorbed by the nucleus, in any case "disappearing" from the elastic channel characterized by the same wavenumber of the incoming neutron. This is the reason why the amplitude of the incoming wavefunction is decreased according to the module of η that in this case is smaller than one.

The non elastic cross section can be calculated in the same way as the elastic one with the previously discussed modification of the equation (1.2). However, instead of the scattered current density, the difference between the total outgoing and the ingoing current densities is used, still calculated according to the equation (1.6). Eventually, the non elastic cross section is given by:

$$\sigma_{ne} = \pi \lambda\!\!\!^{-2} \sum_{l=0}^{\infty} (2l+1)\,(1-|\eta_l|^2). \tag{1.10}$$

Adding this latter to the elastic cross section (1.8), the total cross section can be eventually calculated as:

$$\sigma_{tot} = 2\pi\lambda\!\!\!^{-2} \sum_{l=0}^{\infty} (2l+1)\,(1 - \Re\mathrm{e}(\eta_l)). \tag{1.11}$$

Alternatively, the *optical theorem* relates the total cross section to the only scattering amplitude $f(\theta)$ defined in the elastic scattering according to:

$$\sigma_{tot} = 4\pi\lambda\!\!\!^{-}\,\Im\mathrm{m}(f(\theta)). \tag{1.12}$$

This is of course a simplified formalism where only a rough separation in elastic and non elastic reactions has been taken into account, without the particular output channels of the reactions. To do so, the coefficient η must be generalized in a matrix as well as the term $1 - \Re\mathrm{e}(\eta)$ that becomes the so-called *R matrix* [18]. Each term of these matrices is indeed related to one of the different competing output channels for the compound nucleus decay and includes its relative probability.

Anyway, the important point about this paragraph is that η is the actual conjunction between the cross section and the inner nuclear structure. In fact, assuming a certain model for the nuclear potential, η results from the solution of the Schrödinger equation and determines the cross section carrying the dependence on the model assumed. As previously said, this allows the experimental test of nuclear theories. In the following two simple nuclear models will be discussed.

Black nucleus model

The first model assumed, coming indeed from a classical conception of the nucleus and basis for the compound-nucleus reaction model, is the so-called *black nucleus*. In this model, the nucleus was thought as a black disc of radius R absorbing all the particles arriving on its surface because of the strong interactions between the nucleons.

In details, if a semi-classical model is assumed [15], the angular momentum of an incoming neutron can be related to its impact parameter b and momentum p through the equation:

$$l\hbar = p\,b. \tag{1.13}$$

Therefore, assuming the nuclear radius R as the maximum impact parameter, the neutrons colliding with the nucleus must have $l < pR/\hbar$ or equivalently $l < R/\lambda\!\!\!^{-}$. According to the black nucleus model, all these partial waves are completely absorbed by the nucleus, thus have $\eta_l = 0$. The other partial waves are conversely unaffected by the nuclear potential and have $\eta_l = 1$. Substituting these values in

the equations (1.8), (1.10) and (1.11) and given $\sum_{l=0}^{R/\lambda\!\!\!^{-}}(2l+1) = (R+\lambda\!\!\!^{-})^2/\lambda\!\!\!^{-2}$ the black nucleus elastic, non elastic and total cross sections respectively become:

$$\sigma_{el} = \pi\,(R+\lambda\!\!\!^{-})^2 \tag{1.14a}$$

$$\sigma_{ne} = \pi\,(R+\lambda\!\!\!^{-})^2 \tag{1.14b}$$

$$\sigma_{tot} = 2\pi\,(R+\lambda\!\!\!^{-})^2 \tag{1.14c}$$

Even if coming from a semi-classical model, the formulae (1.14) already show two non-classical effects.

First, even if not properly correctly, in the term $\lambda\!\!\!^{-}$ they introduce the energy dependence of the cross sections, decreasing with increasing energy until they approach asymptotically to the geometrical nuclear cross section.

Secondly, the total cross section is twice the "geometric cross section", the classical expected value, because of the shadow thrown by the target nucleus. In fact, in order to suppress the incoming wave behind the nucleus, it is necessary for the whole area of the nucleus to act as a source of a wave with the same amplitude and opposite phase. Therefore, absorption is always accompanied by a diffraction scattering correspondent to about the same cross section [18].

Nevertheless, the described model is still extremely classical. A more quantistic and reasonable model for the black nucleus actually consists in assuming a potential well that, according to the strong absorption assumption, traps all the particles entering it. Since in quantum mechanics a particle crosses a potential discontinuity only with a finite probability, this assumption requires the presence of a *transmission coefficient* varying from 0 to 1. This can be indeed the interpretation of the term $1 - |\eta_l|^2$ in the non elastic cross section (1.10) [12, 18]. In particular, when it is 1 the classical model described above is found.

This model will be used in the following to explain the low energy behaviour of cross sections.

Optical model

The original conception of black nucleus was based on the assumption of a strong interaction between nucleons that guaranteed the absorption of any impinging neutron.

However, the introduction of the *shell model* depicted a quite different nuclear structure, where nucleons move independently in a mean nuclear potential in different energy levels according to the Pauli exclusion principle. For this reason, the nucleus turned out to be much more transparent to incident nucleons than initially thought and not only at higher energies as described for direct reactions, but also at lower ones. In fact, according to the shell model, the low-energy nuclear shells are occupied and thus not available for the absorption of low-energy

nucleons: even low-energy incident nucleons therefore have to cross many times the nucleus before having a chance of interacting [8, 13]. An other proof of the nuclear transparency will be found in the oscillating behaviour of cross sections at high energy, as will be discussed in the next section.

Eventually, the nucleus turned out to be a weak absorbing entity described by the *cloudy crystal ball* or *optical model*, named after the analogy with the interaction of light with a glass sphere and introduced in the fifties by Feshbach, Porter and Weisskopf [19]. In details, the nucleus is modeled by a complex potential acting on nucleons: $U(r) = V(r) + iW(r)$. The real part $V(r)$, that can be identified with the Saxon-Wood potential used in the shell model, mainly accounts for scattering. Conversely, the imaginary part $W(r)$ is responsible for the absorptive effects and depends on energy. Other terms regarding the spin-orbit interactions, the spin-spin interactions and the Coulomb interaction are added in a more advanced treatment [12].

The optical potentials have a set of adjustable parameters and can reproduce well cross sections even at high energy, however they can describe only average cross sections without describing the single resonances.

1.2.3 Energy dependence

The discussed quantum model allows one to deduce some common properties of the neutron cross section dependence on the energy of the incident neutrons. In Figure 1.5 some neutron partial cross sections for ^{238}U as function of the energy of the incident neutron are shown as an example. First of all, three different energy regions where cross section have a different behaviour can be distinguished: *slow neutrons* below eV, *resonance neutrons* in the range from eV and keV and *fast neutrons* above 10 - 100 keV.

Slow neutrons

According to the semi-classical model discussed in the previous section, at incident neutron energies far below 20 MeV, and that is the case of slow neutrons, only interactions involving the $l = 0$ partial wave are likely to occur [15]. Moreover, at these energies the compound nucleus reaction model can be assumed and the nucleus can be modeled as a square well potential according to the quantum black nucleus model previously discussed. Solving the Schrödinger equation for this configuration gives [18]:

$$\eta_0 = \frac{K - k}{K + k} e^{-2ikR} \tag{1.15}$$

where R is the nuclear radius, K and k are the wavenumbers respectively inside and outside the nucleus with $k << K$ due to the hypothesis of slow neutrons.

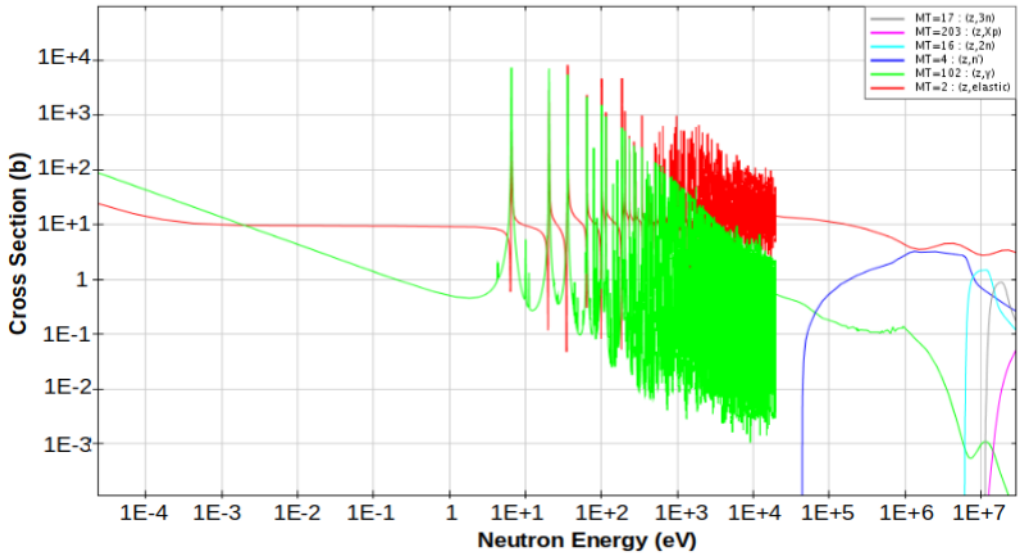

Figure 1.5: Example of partial neutron cross sections for ^{238}U. In red the elastic scattering cross section, the others are the dominant contributions to the non elastic one, in details: the violet is the (n,n') inelastic, the green (n,γ), the light blue (n,2n), the gray (n,3n), the purple (n,Xp). The three regions of slow, resonance and fast neutrons can be observed. The description in the text is well reproduced. Data from the ENDF/VIII.0 Library [20].

For what regards the elastic scattering, using η_0 from the equation (1.15) in the general formula (1.9) and considering the low energy limit ($k \to 0$) gives:

$$\sigma_{el} = \lim_{k\to 0} 4\pi \frac{\sin^2(kR)}{k^2} = 4\pi a^2, \tag{1.16}$$

a constant value depending on the finite limit $\lim_{k\to 0} \sin kR/k = a$ called *scattering length*. For slow neutrons, the elastic scattering cross section is indeed a constant function of energy and the potential scattering is the physical reason for this. Actually, the scattering cross section increases at very low neutron incident energies because of a thermal effect: in this region the neutrons are so slow that the thermal motion of the target nuclei affects the scattering increasing the probability of neutrons being hit by a moving nucleus. This effect disappears indeed decreasing the temperature of the target [8].

On the other hand, the total non elastic cross section has a completely different behaviour. In fact, using η_0 from (1.15) in the equation (1.10) and taking the low energy limit it can be written as:

$$\sigma_{ne} = \frac{\pi}{k^2} \frac{4\,K\,k}{(K+k)^2} \xrightarrow[k<<K]{} \frac{4\pi}{K} \frac{1}{k}. \tag{1.17}$$

Accordingly, the non elastic cross section at low energies depends on the inverse of k, i.e. depends on the inverse of the velocity of the incident neutron. A discussion about the separate cross section energy dependence of the different non elastic channels can be found later.

The described behaviours can be observed in the elastic and capture cross section in Figure 1.5.

Resonances

Increasing the energy of the incident neutrons, both the elastic and the non elastic cross sections show a succession of sharp peaks, superimposed to the tendency described above, that get closer and closer.

As anticipated in the section 1.1.1, this behaviour is due to the discrete excitation levels of compound nuclei: the peaks correspond indeed at the energies of the incident neutron that match exactly the energy of a resonance.

The actual shape of resonance cross sections can be deduced considering for simplicity the elastic scattering cross section (1.10) [15]. If a resonance at the energy E_R and involving only a particular partial wave is considered, then the cross section for that partial wave must have a maximum at that energy, meaning that $\delta_l(E_R) = \pi/2$. If, for convenience, the cotangent of the phase shift is Taylor expanded at the first order for energy around E_R and the width is defined as $\Gamma = 2\,(\partial\delta_l/\partial E)^{-1}_{E=E_R}$ so that:

$$\cot\delta_l(E) = \cot\delta_l(E_R) + (E - E_R)\,\frac{\partial\cot\delta_l(E)}{\partial E}\Big|_{E=E_R} = -\frac{E - E_R}{\Gamma/2}, \tag{1.18}$$

$\sin^2\delta_l$ can be retrieved from trigonometry and put in the formula (1.9). Replacing the factor $(2l + 1)$ with the more general factor $g = (2I + 1)/(2s_n + 1)(2s_t + 1)$ that takes into account both the total angular momentum of the resonance I and the spins of projectile s_n and target s_t and factorizing the width at the numerator distinguishing between the entrance (Γ_{in}) and the exit (Γ_{out}) widths that enables different input and decay channels, the formula can be generalized as:

$$\sigma(E) = \pi\lambda\!\!\!^{-2}\, g\,\frac{\Gamma_{in}\,\Gamma_{out}}{(E - E_R)^2 + \Gamma^2/4}. \tag{1.19}$$

This is the *Breit-Wigner formula* describing the shape of the cross sections in proximity of an isolated resonance both for elastic and non elastic reactions. Actually, the shape of the elastic scattering resonances usually differs from the Breit-Wigner formula because of a characteristic dip anticipating the resonance due to the interference between resonance and potential scattering. It is shown in Figure 1.6.

The extension of the resonance region depends on the distance between the excited levels of compound nuclei: light nuclei typically have well spaced excited states and then resonances occur at higher neutron energy, even MeV, while heavy nuclei, except for particularly stable ones, have closer excited states and the neutron energies matching the resonances are lower, from less than eV to even less than keV.

Fast neutrons

Increasing the neutron energy, resonances become so close that they merge in a continuum and the cross sections also become smooth functions of energy: this is typical of fast neutrons. In this energy region a particular behaviour is shown by the elastic cross section that fluctuates in energy, as shown again in Figure 1.5. These fluctuations are explained in terms of interference between the neutrons scattered passing inside the nucleus and around it [12]. For this reason, they were among the first evidences of the nuclear transparency leading to the optical model.

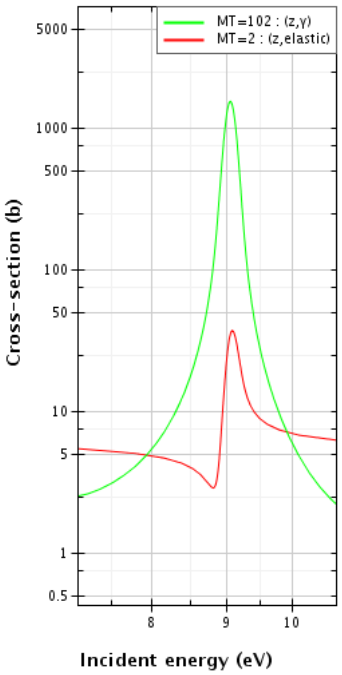

Figure 1.6: Enlargement of a resonance in the ^{115}In(n,γ) (green) and ^{115}In(n,n) (red) cross sections. The former reproduce the Breit-Wigner formula, while the latter shows the characteristic dip due to the interference with potential scattering. Data from the ENDF/VIII.0 Library [20].

Non elastic and total cross sections

Until now the total non elastic cross section has been always generally considered, that is nothing but the cross section for the formation of the compound nucleus, at least below 20 MeV where the compound nucleus reaction model is assumed. However, the non elastic cross section actually includes a lot of different reactions corresponding to the different decay modes of the compound nucleus whose cross sections are in general more difficult to provide a general behaviour separately, a part for some exceptions.

For example, neutron radiative capture is usually the dominant non elastic reaction at low energy, thus its cross section reproduces the total non elastic cross section described above, characterized by the $1/v$ behaviour and by the resonances. However, at higher energy it falls rapidly to 0. It is shown again in Figure 1.5.

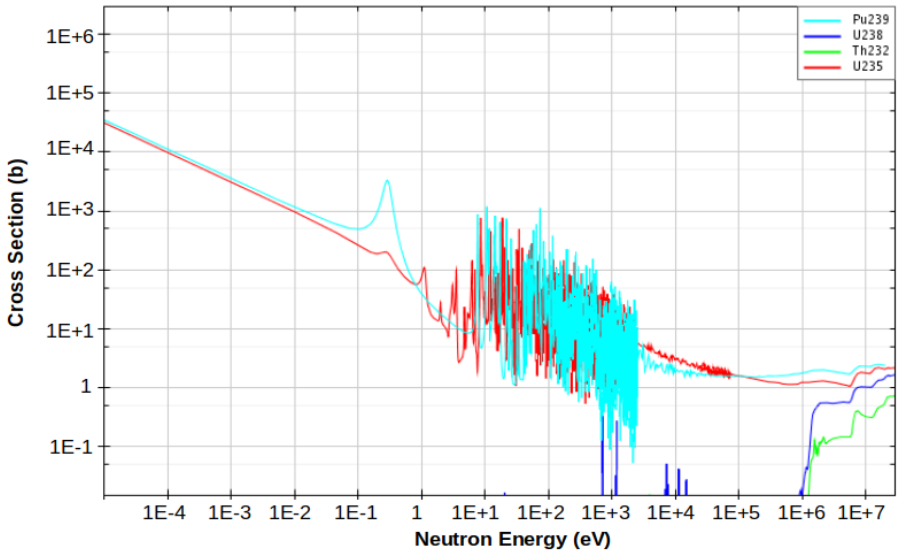

Figure 1.7: Comparison between the fission cross sections of ^{235}U (red), ^{239}Pu (light blue), ^{238}U (blue) and ^{232}Th (green). The two former are fissile nuclei with a high 1/v fission cross section at thermal energy, the others conversely show a threshold around 1 MeV. Data from the ENDF/VIII.0 Library [20].

Conversely, inelastic scattering and nucleon evaporation (except for the emission of only one neutron that is considered in elastic scattering) usually have a threshold and become the dominant non elastic reactions only at energy higher than some keV. In the same way as before, in this energy region their cross sections reproduce the smooth and nearly constant total non elastic one.

Fission is the other important non elastic reaction to be considered for some heavy nuclei, but its behaviour is different according to two different classes of nuclei as shown in Figure 1.7. For *fissile* nuclei it competes with neutron capture at low energy and thus their cross sections have the same behaviour, showing both the $1/v$ and the resonance regions. Conversely, the other *fissionable* nuclei usually have a threshold and thus fission competes only at high energy with inelastic scattering and nucleon evaporation and its cross section similarly has a smooth and nearly constant dependence on energy.

In conclusion, adding all the previously analyzed cross sections, the total neutron cross section is found. Its energy dependence depends of course on the reactions that are more likely to occur depending on the nucleus, especially at low energy where the behaviour of the partial cross sections is very different. Therefore, a nucleus whose total neutron cross section shows a $1/v$ trend at low energy will be a good neutron absorber (as ^{10}B) or a fissile nucleus (as ^{235}U or ^{239}Pu), while constant total cross sections will be found for good neutron scatterers, as

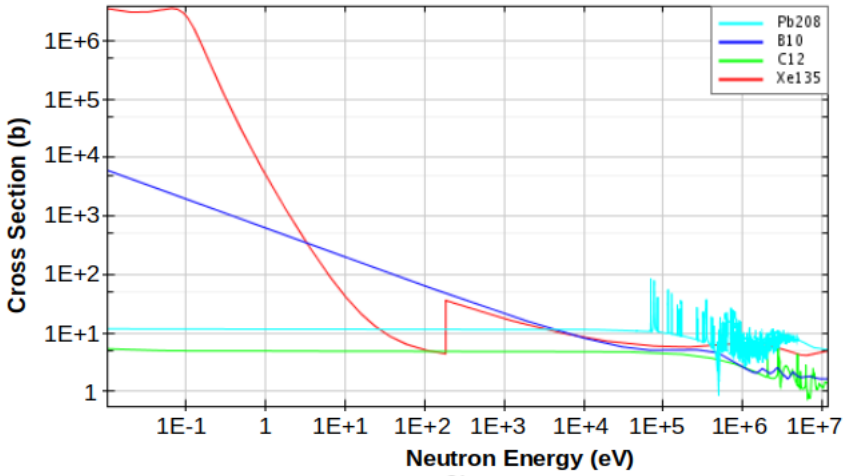

Figure 1.8: Comparison between the total neutron cross sections of two neutron absorbers, ^{135}Xe (red) and ^{10}B (blue), and two neutron scatterers, ^{208}Pb (light blue) and ^{12}C (green). The main difference regards the low energy behaviour where the former increase decreasing energy, while the latter are flat. Data from the ENDF/VIII.0 Library [20].

shown in Figure 1.8. In particular, if the latters are also light nuclei, they can receive considerable energy from neutron collisions, thus can be used as neutron moderators (as ^{1}H or ^{12}C).

1.3 Applications of neutron cross sections

The importance of neutrons in fundamental nuclear physics has been already outlined in the previous sections in terms of their capability of accessing directly the nuclear structure and then testing nuclear theories through the comparison between deduced and measured cross sections. However, neutron reactions have a great importance also concerning nuclear astrophysics and the nuclear technologies involved in power production as well as in the cancer therapy or in the industrial imaging. For these applications, the knowledge of neutron cross sections with increasing accuracy is needed, especially for fast neutrons (MeV) which innovative technologies mainly exploit, but, currently, the available data are often scarce.

1.3.1 Power production technologies and reactors

Neutron induced fission is exploited for electricity production since the fifties and nowadays produces approximately the 10% of the globally produced electricity,

percentage rasing to 18% considering only developed countries and even to 75% for France [21].

Most of the conventional fission reactors operating nowadays belong to the *LWR* (*Light Water Reactor*) type, that are thermal neutron reactors employing water both as moderator and coolant and using enriched uranium as fuel. More in details, ^{235}U (and in general fissile nuclei) has a higher neutron induced fission cross section for thermal neutrons, but those produced by fission are fast. The moderator is indeed needed in order to slow down neutrons so that a chain reaction can be sustained. A coolant is employed to drive the heat produced by the fission reactions away from the core both to prevent the meltdown and to convert it in electricity. Using light water for these purposes requires the enrichment of uranium with 3 or 5 % of ^{235}U (that is naturally present at 0.7%) to compensate for the absorption of neutrons by hydrogen in water. An other type of reactor, the *HWR* (*Heavy Water Reactors*), employs heavy water that, having a lower probability of capturing neutrons, allows the use of natural uranium as fuel.

These reactors have some common problems that are making them more and more unpopular among the public opinion: their increasing age especially in the advanced economies (the average age of reactors is respectively 39 and 35 years in the US and EU [22]) and the high costs for their replacements, the production of long-term radioactive waste that are difficult to handle and to store, the potential risks connected to nuclear accidents as those of Čhernobyl and Fukushima. For this reason, some developed countries are planning to phase out nuclear electricity production in the next years that, for instance, already decreased of more than 10% in the last 10 years in the EU. This tendency is inverted in the developing countries such as China and India, that alone host the 33% of reactors under construction in 2019 [23].

As a matter of fact, despite of the problems described, nuclear power can have a very important role in a clean energy transition being a carbon-free energy source. Leader among the carbon-free power sources since its introduction, the International Energy Agency (IEA) has estimated that without nuclear power the CO_2 emissions related to the global electricity generation would have been 20% higher in the last fifty years, a percentage raising up to 40% considering only Europe and even 50% for Canada [22]. The declining share of nuclear power in the global energy mix observed in recent years is thought indeed as one of the main reasons why the rapid expansion of renewables has failed to stop the increase in CO_2 emissions [23]. In conclusion, nuclear power could largely contribute in facing the increasing energy demand caused by the rising of the global population and by the developing countries. Moreover, it could also help to reduce the CO_2 emissions from the burning of fossil fuels, which still accounts for approximately the 80% of the global energy supply [21] and contributes to the global warming.

For these reasons, in this moment there seems to be a renewed interest on new

nuclear technologies and reactors capable of supplying efficiently carbon-free energy and electricity, but addressing the objectives defined by the GIF (Generation IV International Forum [24, 25]):

- sustainability (more efficient utilization of the resources and waste minimization),
- enhanced economics,
- safety and reliability,
- proliferation resistance (resistance against the spread of nuclear weapons).

This renewed interest is proved for example by the recent foundation of two new start-ups operating in this field: the italian-english *Newcleo*® [26] and the swiss *Transmutex* [27].

Nuclear waste management

Most of the conventional fission operating nuclear reactors (especially in the USA) adopt the so-called *once-through fuel cycle*, in which the uranium fuel is used only once and then stored. This strategy is not sustainable under different aspects.

First of all, it has a quite low efficiency in the uranium resources utilization. In fact, because of the neutron poisons increasing during the burn-up and decreasing the reactivity, the fuel has to be refreshed when there is still some fissile material inside, usually 0.8% of ^{235}U and 1% of ^{239}Pu. The majority of the spent nuclear fuel is made of ^{238}U (approximately the 95%), whose fertility is practically not exploited in thermal reactors. In this way, only the 1% of the mined uranium is effectively used to produce power and this low efficiency will lead to problems in the availability of uranium resources within 50–100 years [24].

The second critical aspect concerns the radio-toxicity of nuclear waste. In fact, a part from uranium, the nuclear spent fuel contains fission fragments that, although mostly stable (3.1% of the total waste), includes some short-lived radioactive isotopes with half-lives lower than 100 years (as ^{137}Cs or ^{90}Sr) whose decay heat and γ emission are the most limiting short-term factors in the repository designs. However, the main concern regards the smallest fraction of nuclear spent fuel that includes a few long-lived fission products (0.2%) and transuranic elements (1.1%). Specifically, ^{99}Tc, ^{129}I, ^{135}Cs, ^{93}Zr, ^{126}Sn and ^{79}Se belong to the former, while the latter include plutonium (1%) and minor actinides as americium, curium and neptunium (0.1%) that are produced through chains of neutron captures and beta decays from uranium. These elements indeed have extremely long lifetimes (hundreds of thousands of years) that are responsible for the long-term

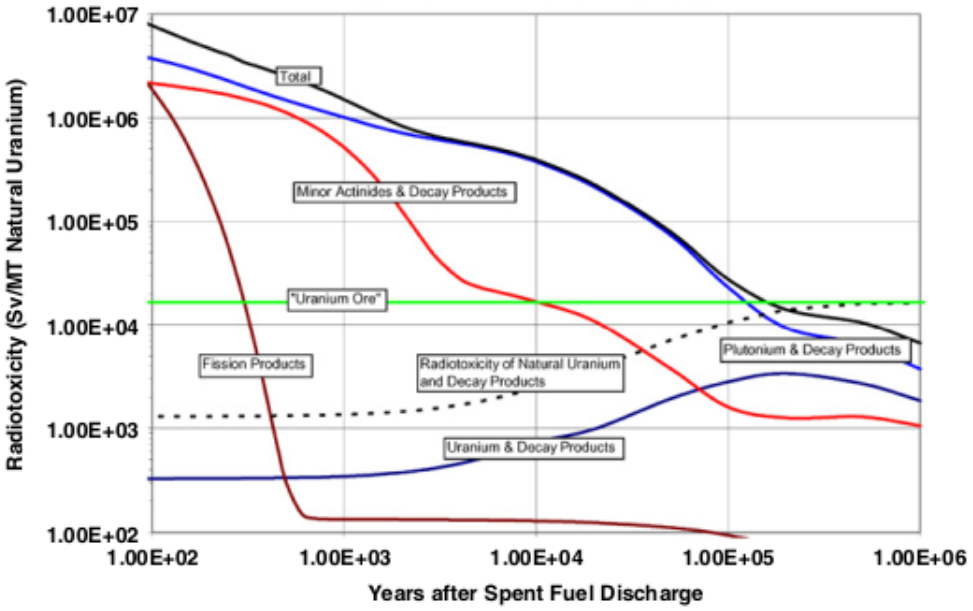

Figure 1.9: Radiotoxicity for the various component of a typical PWR nuclear waste in function of time. Transuranic elements, plutonium over all, are clearly responsible for the long-term radiotoxicity. From [24].

radio-toxicity of waste (Figure 1.9) and represent a significant radiological source term in the repository over hundreds of thousands of years.

Reprocessing spent nuclear fuel through partitioning and transmutation, according to the scheme of Figure 1.10, is regarded as one possible solution to these problems. In fact, it can lead to the recovery of fissile materials from the spent fuel in order to improve the resources utilization and to reduce the waste volume, its radio-toxicity (especially at long term) and the heat to be consigned to the geological disposal, impacting on its dimensions and characteristics. However, an important drawback is the risk of nuclear proliferation.

Partitioning, the first step, is referred as the chemical process applied to spent nuclear fuel to separate out the constituents. In particular, fissile and fertile uranium and plutonium can be separated and re-used even in conventional fission reactors through the so-called *MOX* fuel (*Metal OXide fuel*), as has been already happening in some countries such as France for years. Furthermore, long lived fission products and minor actinides can be also separated from stable fission products and short-lived ones. The former can undergo transmutation, while the latter are respectively directly disposed or temporary stored for heat decay before disposal.

Transmutation, the second step foreseen for long-lived radioactive waste, con-

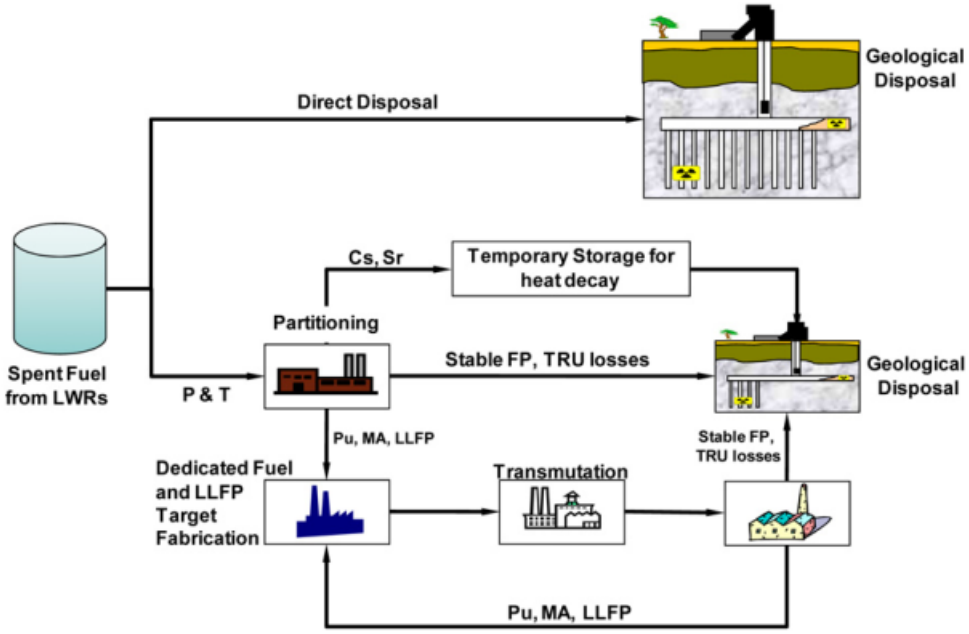

Figure 1.10: Scheme for the once-through open fuel cycle (above) and an advanced closed fuel cycle (below) employing partitioning and transmutation techniques. From [24].

sists in its "transformation" into short-live or stable isotopes through nuclear reactions. The most effective transmutation reactions seem to be neutron-induced reactions, specifically capture and fission [28].

In particular, neutron capture is particularly suitable for the transmutation of fission products since they cannot fission, but can be turned to stable isotopes capturing a neutron and then rapidly decaying as:

$$\begin{aligned} n + {}^{99}Tc(2.11 \cdot 10^5 y) &\xrightarrow[capture]{} {}^{100}Tc \xrightarrow[\beta(16s)]{} {}^{100}Ru(stable) \\ n + {}^{129}I\,(1.57 \cdot 10^7 y) &\xrightarrow[capture]{} {}^{130}I \xrightarrow[\beta(12.3h)]{} {}^{130}Xe(stable). \end{aligned} \tag{1.20}$$

In order to maximize the capture cross section fission products must be exposed to high neutron fluxes suitably moderated that can be provided for example by the reactors themselves.

Conversely, fission is the preferred process for the transmutation of transuranics and minor actinides since it produces, besides mostly stable or short-lived fission products, an energy gain and a surplus of neutrons that can be employed with different purposes. However, the fission cross section for the minor actinides has often a threshold at few hundred keV or MeV and it is always in competition with the unwanted neutron capture, that conversely transmutes nuclei into higher

actinides and is dominant at low neutron energies. For these reasons, fast neutrons are the most suitable to efficiently incinerate minor actinides.

Hence, accurate data on the fission and the capture cross sections of actinides and reactor structural materials at high energy are essential for the design of the fast systems required such as fast IV Generation reactors or ADSs. Lots of these cross sections with the needed accuracy were indeed inserted in the *Nuclear Data High Priority Request List* [29] by the Nuclear Energy Agency of the OECD as urgent measurements to perform.

Fast reactors

Fast reactors, as the name suggests, employ fast neutrons instead of the thermal neutrons used in the LWRs and represent the majority of the future IV Generation reactor designs.

In these reactors, in order to avoid the thermalization of neutrons from fissions, no moderator is used and water cannot be used neither as coolant. According to the different designs, it can be replaced by other materials as sodium (in the *SFR - Sodium-cooled Fast Reactor*), molten lead with or without bismuth (in the *LFR - Lead-cooled Fast Reactor*) or helium (in the *GFR - Gas-cooled Fast Reactor*).

The advantages in using fast neutrons are several. A first one is the possibility, as previously mentioned, of burning more efficiently the minor actinides through fission, thus reducing the long-term radiotoxicity of waste [24, 28]. A second advantage is the possibility of breeding more efficiently fissile materials from the more abundant fertile materials [30], in particular ^{239}Pu from ^{238}U through neutron captures according to:

$$n + {}^{238}U \xrightarrow[capture]{} {}^{239}U \xrightarrow[\beta(23.45m)]{} {}^{239}Np \xrightarrow[\beta(2.35d)]{} {}^{239}Pu. \tag{1.21}$$

In fact, using fast neutrons the plutonium production rate and its fission rate are similar, thus the fissile material can be replenished as it burns. Furthermore, since fast neutron induced fissions generally release a higher number of neutrons, in fast systems a neutronic surplus results, capable of further increasing the breeding mechanism to produce even more fissile material than what is used.

These effects eventually results in the possibility of using the more abundant ^{238}U as fuel together with the fissile ^{235}U, thus greatly enhancing the utilization of the mined natural uranium and allaying concerns about its long-term availability. Moreover, in principle, even the spent fuel of LWRs could be employed as fuel in order to use the residual uranium and burn the other actinides. Even more, instead of the conventional uranium/plutonium cycle, this breeding mechanism is under study in application to the thorium/uranium cycle, where the fertile ^{232}Th, that makes up nearly all the natural thorium, can be transmuted in the fissile ^{233}U

according to:

$$n + {}^{232}Th \xrightarrow[capture]{} {}^{233}Th \xrightarrow[\beta(21.83m)]{} {}^{233}Pa \xrightarrow[\beta(26.98d)]{} {}^{233}U. \tag{1.22}$$

Among the advantages of this cycle, thorium is three to four times more abundant than uranium in the Earth's crust and its employment should reduce the building up of plutonium and transuranics [28]. Conversely, one of the problems to face is the building up of ^{233}Pa that is a neutron poison.

A third advantage of some fast reactors designs regards eventually the increased safety. For example, using molten lead as coolant should prevent, in case of accident, the leakage and the dispersion of radionuclides, since lead rapidly freezes in contact with air, and the thermal explosions related to the high pressure, since lead has an extremely high boiling point and cooling is naturally guaranteed by convection.

Furthermore, these Generation IV reactors are thought in a cogeneration perspective, i.e. they are thought to additionally exploit the 60-70% residual heat not transformed into electricity for purposes such as district heating or carbon-free hydrogen production [31].

Despite the several advantages, fast reactors have some disadvantages to handle. Apart from the high costs, the nuclear fuel requires a higher enrichment of fissile materials to start the chain reaction, the higher neutron density have bad effects on the reactor structures and the stability of the reactor is harder to control because of the faster time scale over which the reactor state changes, due to the fewer delayed neutrons produced by fast fissions.

ADS

The *ADSs* (*Accelerator Driven Systems*) are an other kind of fast neutron systems first suggested by C. Rubbia as "energy amplifiers" [32] that can be used both to produce power and to incinerate actinides.

The basic concept of ADSs consists in coupling a proton accelerator with a sub-critical reactor, that is not able to self sustain a chain reaction. The accelerator has to deliver high energy particles (typically protons above several hundreds MeV) on a suitable target placed inside the reactor. In the target, usually made of heavy material as lead, bismuth, tungsten or even uranium and thorium, spallation (especially for GeV protons) and other proton-induced reactions release a high number of fast neutrons in the reactor core. These fast neutrons are employed to induce fission reactions to produce power and transmute the long-lived actinides and capture reactions to breed fissile fuel from the fertile material, just as a fast reactor described above. In the same way, ADS should allow in principle the usage of natural uranium as fuel as well as thorium and LWR spent nuclear fuel.

The advantage with respect to the critical fast reactors described above is that the nuclear fuel does not have to be enriched to sustain a chain reaction alone because additional neutrons are externally supplied. This implies an even greater advantage of ADS: the enhanced inherent safety. In fact, since the reactor cannot sustain the chain reaction without the external neutron supply (i.e. it is subcritical), it automatically turns off when the input current is switched off, thus preventing the possibility of runaway reactions.

On the other hand, disadvantages mainly regard the greater complexity of these systems, the volatile radionuclides produced by spallation and the higher "energetic cost" of spallation neutrons that require to spend energy in accelerating protons, even if a beam gain power between 10^2 and 10^3 seems reachable [33].

One of the most advanced ADS projects under construction is *MYRRHA* (*Multipurpose hYbrid Research Reactor for High-tech Applications*) [34], developed by the belgian nuclear researh center (SCK.CEN). In details, it consists of a 400 m linear accelerator delivering 600 MeV protons on a liquid lead-bismuth target and a lead-bismuth cooled reactor able to work both in sub-critical or critical mode. It is scheduled to start operation in 2026 and it is aimed to demonstrate for the first time the full ADS concept feasibility. Among the other research objectives the study of waste transmutation, material irradiation and radioisotopes production.

Nuclear fusion

The other great interest for carbon-free electricity production in an inherent safe way and practically without long-lived radioactive waste is nuclear fusion. Entering the details, the advantages and the challenges related to the nuclear fusion would take too long and is outside the aims of this work. What is important in the perspective of this chapter is that the most feasible and near future promising fusion reaction, the deuterium-tritium fusion in helium, additionally releases a 14 MeV neutron carrying most of the energy produced in the process. These neutrons are extremely important in the process because they can escape the confined plasma and transfer their energy to the blanket as heat that in turn will be collected and used to produce electricity. Moreover, interacting with the suitably chosen blanket material, neutrons should be able to breed the tritium used as fuel. However, at the same time they inevitably activate and potentially damage the reactor components.

For these reasons, neutron cross sections have a key role even in the nuclear fusion research field. Their knowledge is important indeed to foresee the overall effects of neutron in the blanket and to choose the best materials to improve breeding and heat transfer on one hand and on the other to reduce the structural damages and the long-term induced radioactivity due to the neutron irradiation.

1.3.2 Other applications

Nuclear astrophysics

If fusion reactions account for the nucleosynthesis of elements up to ^{56}Fe in the stars, neutron induced reactions are responsible for the nucleosynthesis of all the other heavier elements. In particular, depending on the condition of the star and on the available free neutron density, two different processes can occur: the *r-process* and the *s-process*, respectively meaning *rapid* and *slow*. Both are based on subsequent neutron capture reactions and beta decays.

In the s-process, as the name suggests, the capture rate is low and the unstable isotopes produced by capture almost always undergo beta decay before they can capture other neutrons. This process indeed synthesizes the nuclei along the valley of stability from iron up to lead and bismuth.

Conversely, in the r-process several subsequent neutron captures occur at a high rate before a beta decay takes place. For this reason, this process is responsible for the synthesis of the neutron-rich isotopes and the nuclei heavier than bismuth. Especially regarding these latter, there is also the possibility that the unstable isotopes produced by captures undergo spontaneous or induced fission. In this case, the fission fragments can act as new seeds for new cycles of rapid neutron captures. This overall process is called *fission recycling* [35].

The pathways of these processes are not unique, but have branching points: particular isotopes for which the conditions in the star (such as neutron density or temperature) make the capture rate comparable to the decay or fission rate. Both the processes are then available for the evolution of the isotope with a probability defined exactly by the condition inside the star and by the decay and reaction rates, that are nothing but the cross section. Provided this probability by the measurement of the isotopic abundances, the accurate knowledge of cross sections at branching points is essential to determine the internal condition of the stars and consequently improve the star evolution and nucleosynthesis models [36].

Medical applications

Neutron induced reaction data are of key importance in medicine for two main reasons.

First, they are required in neutron irradiation facilities for the production of the radioisotopes used in diagnostic and in some cancer treatments, such as the metastable ^{99m}Tc or the emergent ^{177}Lu [37].

On the other hand, neutron cross sections are extremely important for the accurate and precise knowledge of neutron transport in the human body needed to determine the optimum irradiation parameters in hadron-based tumor treatments. In fact, even in the widespread proton and heavy ion therapies, neutrons can be

generated as secondary particles by the direct reactions induced by protons or heavy ions and deliver a significant dose outside the beam area [38].

Eventually, a special mention is deserved by the *Boron Neutron Capture Therapy* (*BNCT*) [39]. It directly exploits thermal neutron irradiation on the tumor, previously enriched with ^{10}B, a neutron absorber. Tumoral cells uptake a higher boron concentration than healty ones. In this way, the particles ejected by the boron neutron captures release a large amount of energy directly in the tumor area with an enhanced probability to kill the cancer while sparing healthy cells.

Neutron imaging

Neutron imaging [38, 40] is a non-destructive analysis method that is gaining importance and spreading for industrial applications. Because of the different reaction mechanism, neutron imaging provides indeed complementary information with respect to the conventional x-ray imaging. In particular, x-rays attenuation increases with denser material since they mainly interact with atomic electrons and then are sensitive to high Z atoms. Conversely, neutrons, and especially fast neutrons, can easily penetrate thick-walled or metal-shielded samples and allow one to study larger objects. Moreover, according to their different cross section, neutron imaging can distinguish elements with close atomic numbers or even isotopes of the same element and it is particular sensitive to low atomic number materials such as hydrogenous materials, important moderators.

Especially for this last reason, neutron imaging is not only used to check materials and industrial components, but also to detect explosives and for geological purposes, for example to study the porosity of rocks (detecting water inside them) [41].

Chapter 2

The n_TOF facility

The previous chapter dealt with the theory and some of the applications of neutron cross sections, showing how their accurate knowledge plays a key role in fundamental and applied nuclear science as well as in nuclear engineering and medicine. Although nuclear theories can provide estimates of cross sections, experimental measurements are mandatory to reach the precision and the accuracy required by the applications. For instance, the *Nuclear Data High Priority Request List* [29] drawn up by the Nuclear Energy Agency (NEA) of the OECD summarizes some important reactions whose data need experimental evaluation or improvement in terms of energy range and uncertainty.

For this reason there are lots of facilities around the world producing neutron beams devoted to these measurements and the n_TOF facility [36], part of the fixed target experimental program at CERN, is an important example. This chapter discusses its main features.

2.1 Overview of the facility

The n_TOF facility (acronym of *neutron Time-Of-Flight*) is a pulsed white neutron spallation source conceived by C. Rubbia in 1998 [42] in order to provide accurate measurements of neutron induced reaction cross sections useful for basic nuclear sciences, nuclear astrophysics and advanced nuclear technologies as described in the previous chapter. Thanks to its high instantaneous flux, to its extremely wide neutron energy range covering up to 11 orders of magnitude from thermal to GeV and to its high energy resolution, the n_TOF facility has been one of the most active facilities since the beginning of its operations in 2001. Indeed, many cross section measurements carried out during its three experimental campaigns (2001-2004, 2009-2012, 2014-2018) were included in the major public nuclear data libraries such as JEFF, ENDF/B and JENDL [38, 43]. In particular,

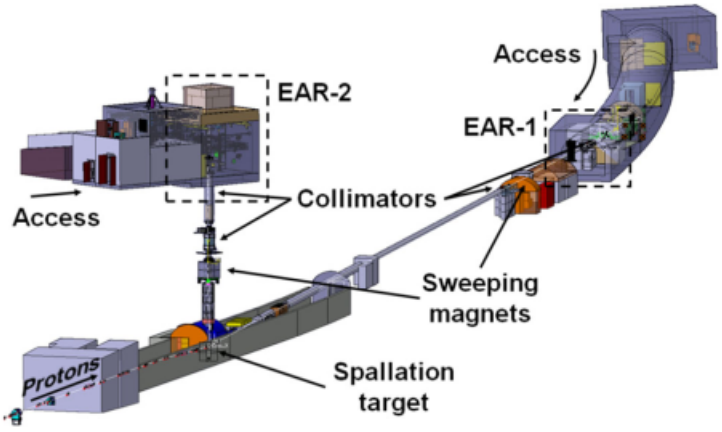

Figure 2.1: Layout of the n_TOF facility showing the spallation target, the two experimental areas and the main elements on the beam lines. Protons delivered on the target come from the CERN PS [35].

radiative capture and fission have been the mostly studied reactions, but in the recent years neutron induced reactions on medium and light nuclei emitting charged particles, such as (n,α) reactions, have been also studied. Now the facility is ready to start its fourth experimental campaign with a new spallation target that became operational in July 2021.

A layout of the n_TOF facility is shown in Figure 2.1. The facility is based on the CERN Proton Synchrotron (PS). In its supercycle the PS accelerates protons injected from the PS Booster (PSB) to be delivered with the required features to different facilities (ISOLDE, the AD and n_TOF) or to the larger SPS and LHC.

In particular, in the n_TOF dedicated cycles [44], bunches of up to $8.5 \cdot 10^{12}$ protons of momentum 20 GeV/c and concentrated in a time interval of 7 ns are fast-extracted and delivered to the n_TOF lead spallation target, that will be discussed in details in the section 2.2.1. These three characteristics of the proton bunches respectively guarantee the high intensity, the wide energy range and the high resolution of the neutron beams produced. The minimum time period of the dedicated pulses is 1.2 s, correspondent to a maximum repetition rate of 0.8 Hz, but a smaller rate (about 0.25 - 0.40 Hz) is usually used to contain the temperature and the radioactivity of the target area. Apart from these dedicated bunches, the n_TOF facility also receives parasitic bunches of lower intensity (approximately $3.5 \cdot 10^{12}$ protons) with the other features unchanged. Overall, approximately the 15% of the protons accelerated by the PS are dedicated to the n_TOF facility [45].

The beam position, the profile and the intensity of the proton pulses delivered to the facility are monitored before impinging on the spallation target. In particular, a Wall Current Monitor, just upstream the target, provides the so-called *PKUP*

signal. The amplitude of this signal is proportional to the proton beam current and it is used to directly monitor the intensity, the effective delivery of protons by the PS and for timing purposes.

Neutrons produced by spallation are then moderated to further enlarge the neutron energy spectrum and driven to the two experimental areas through two vacuum tubes equipped with shieldings, a sweeping magnet, a filter box and collimators. The first experimental area (*EAR1*) is placed along the the horizontal beam line at approximately 182.5 m from the target. In 2014 a second experimental area (*EAR2*) was also built vertically at 18.2 m from the target. The measurement of the arrival time of the neutrons in the experimental areas provides the determination of their energy and the measurement of neutron cross sections as function of energy according to the *time-of-flight technique* (discussed in detail in section 2.3). Both the experimental areas are classified as *class A laboratories* with a series of enhanced safety and monitoring systems in order to allow the handling of unsealed radioactive samples and fully exploit the potential of the facility. The modification in the target shielding during its last replacement in 2019-2020 also allowed the design of a further experimental area just behind the target shielding wall and then very close to the target, called NEAR. More details about the experimental areas will be given in the section 2.4.

2.2 Spallation

Spallation [46] is a high energy nuclear reaction in which a target nucleus hit by an incident particle of energy higher than a few hundreds of MeV disintegrates ejecting several lighter particles such as nucleons, pions or other nuclear fragments. Since neutrons cannot be directly accelerated, spallation is a suitable and widely exploited process to produce high energy neutron beams through the collision of accelerated charged particles on a heavy material target.

The process occurs in two main steps. In the first step, within the nuclear characteristic time of 10^{-22} s, the incident particle undergoes a series of direct interactions with the single nucleons inside the target nucleus in a so-called *intranuclear cascade*. This leads to the forward peaked ejection of mainly high-energy protons, neturons and pions with energy from tens of MeV up to the energy of the incident projectile.

After this step, the target nucleus or its fragments are left in a high excited state and this implies the second step of spallation: the nuclear de-excitation or *evaporation*. Actually, the de-excitation can occur immediately after the intranuclear cascade before the nucleus has reached the equilibrium (*pre-equilibrium phase*) or after the excitation energy left in the nucleus has been shared among all the nucleons reaching a thermal equilibrium, typically after 10^{-18} s. In this case the

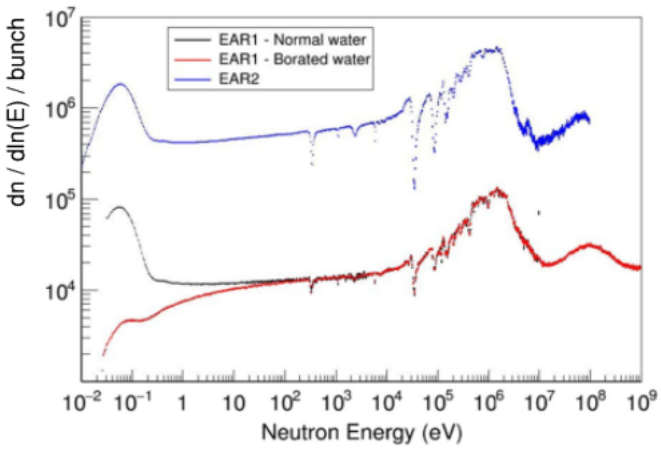

Figure 2.2: Isolethargic evaluated neutron flux in both the experimental areas according to the 2014 commissioning. The peaks corresponding to the neutron evaporation at equilibrium and at pre-equilibrium can be seen respectively around 1 MeV and 10-100 MeV in both the experimental areas. The thermal peaks are due to moderation when water is used. The high energy neutrons (>100 MeV) emitted in the forward direction are present only in EAR1 [35].

nucleus de-excites preferentially fissioning or evaporating neutrons, that are emitted isotropically and with energies around MeV. A subsequent γ de-excitation usually occurs, too.

Anyway, this is what happens to a single target nucleus. Actually, in a thick target the secondary high-energy particles ejected in the intranuclear cascade can hit in turn other nuclei and trigger other secondary spallation reactions until their energy is high enough and so on. This generates a so-called *internuclear cascade* or *hadronic shower*. In particular, the maximum energy and the number of the particles produced in this process increase with increasing the energy of the projectile.

In total, in the n_TOF target approximately 350 neutrons per incident 20-GeV/c proton are emitted. Their spectrum consists of the high energy neutrons up to the energy of the incident protons (> 100 MeV) peaked in the forward direction and of two peaks, around 1 MeV and between 10 - 100 MeV, corresponding to the neutron evaporation in the equilibrium and pre-equilibrium phases respectively. This typical energy spectrum is shown in the neutron flux reaching the experimental areas in Figure 4.19. The energy spectrum of spallation neutrons can be widened employing a moderator coupled to the target to slow down the fast neutrons up to thermal energies.

Beside neutrons, spallation reactions also produce γ rays and charged particles, such as protons, pions and muons (from the pion decay). In particular, the

prompt component of these ionizing particles, made of γ rays and ultrarelativistic charged particles released in the first step of the spallation process, constitutes the so-called γ-*flash* that is detected at the beginning of each neutron bunch in the two experimental areas. A weaker delayed component of γ rays mainly from capture reactions in the moderator, but also in the target and in the surrounding material, is also observed. However, its contribution is approximately one order of magnitude lower than neutrons [44].

2.2.1 The n_TOF spallation target

The new third-generation target [47, 48] is characterized by a revolutionary design aimed at preserving the excellent physics performances of the previous targets in terms of flux and background while improving some aspects.

The previous spallation target was a lead cylinder 60 cm in diameter and 40 cm in length cooled by 1 cm water layer placed around. Its main limitations were the reduction of the achievable neutron fluence and a low energy resolution in EAR2 due to the non-optimized geometry, the erosion-corrosion phenomena and the contamination of the cooling water with spallation products due to the direct contact with lead.

The new target consists of six pure lead flat-top slices host in an aluminum-alloy anti-creeping structure and cooled by a forced flow of gaseous nitrogen in between. The slices are 60 cm wide and 5 cm thick, with the exception of the last one (towards EAR1) that is 15 cm thick to reduce the γ background in EAR1. For the same reason, concerning EAR2, a lead plate is also placed on the top of the target in correspondence of the vertical beam line. The layout of the new target is shown in Figure 3.6.

The choice of pure lead (with a minimum purity of 99.9 wt%), unchanged since the first generation target, is due to its superior physics performances in terms of reduced photon background because of its very low neutron capture cross section. However, it is not a good structural material because of its relatively low melting point, its low corrosion resistance and the easy occurrence of creeping effects. Hence, an anticreeping structure and a powerful cooling system are needed. The upgrade from water to nitrogen cooling should solve the problems of corrosion and contamination of water, but required slicing to increase the surface exposed to the coolant in order to balance the nitrogen lower cooling efficiency. If undesired chemical reactions between nitrogen and lead arise during operation, the cooling system will be able to work even with inert argon, although with a slight further reduction of the cooling efficiency.

Two separated moderators, one for each experimental area, also belong to the target assembly. They constitute the last component crossed by neutrons before entering the beam lines. They are made of alluminum alloys and connected to two

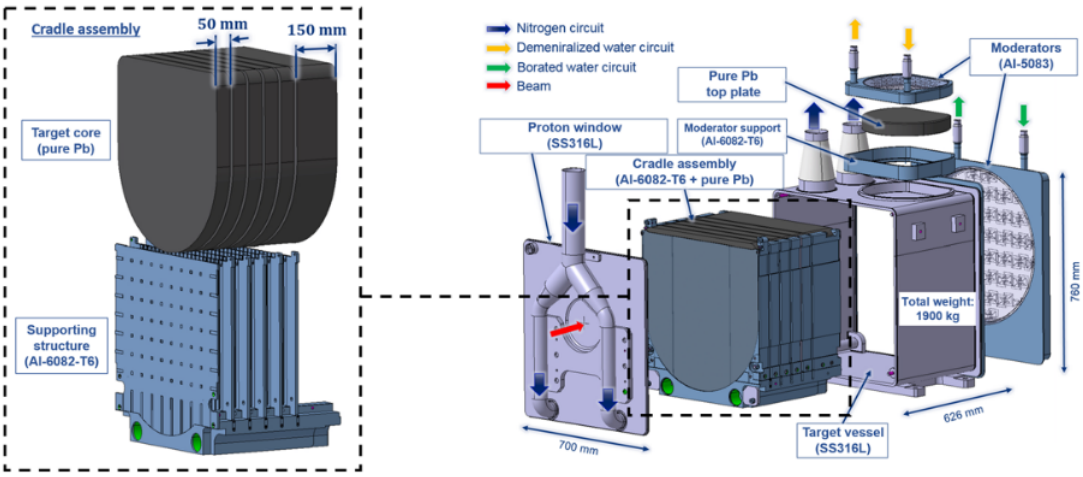

Figure 2.3: Exploded view of the n_TOF third generation spallation target. On the right the whole target assembly including the vessel and the moderators, on the left the cradle assembly enlarged [47].

separate water circuits with a nominal pressure of 2.5 bar. In this way, the moderator for each experimental area can be chosen independently among borated water, water or demineralized water. In details, borated water (1.28 wt% 10-boron enriched at 99%) reduces of about one order of magnitude the 2.2 MeV delayed photon background caused by the radiative neutron capture in the hydrogen contained in water. According to some evaluations, it indeed accounts for nearly 40% of the total delayed photon background in EAR1 [44]. However, the drawback in using boron is the reduction of the neutron intensity at thermal energy due to its huge capture cross section. Conversely, the delayed γ background in EAR2 mainly arises from the interaction of neutrons in the collimator at the entrance of the experimental area and in the dump, therefore demineralized water or water are still suitable as moderators [48].

All the target assembly (except for the top lead plate and the moderator for EAR2) is hosted inside a stainless steel vessel (required by radioprotection issues) with thinner windows designed in correspondence of the incoming proton and outcoming neutron beam impact points.

2.3 The time-of-flight technique

High energy spallation and further moderation allow the production of white neutron beams covering a wide energy range. Consequently, neutron cross sections as a function of the energy can be measured with high resolution using the *time-*

of-flight technique. This method requires pulsed beams and possibly long flight paths [49].

More in details, this technique consists in the determination of the neutron velocity v from the measurement of the time spent by the neutron (the time of flight ΔT exactly) to travel a given distance L according to:

$$v = L/\Delta T. \tag{2.1}$$

This value is eventually used to calculate the neutron kinetic energy E through the relativistic formula:

$$E = mc^2\,(\gamma - 1) \;\text{ where }\; \gamma = \frac{1}{\sqrt{1 - (v/c)^2}}. \tag{2.2}$$

However, this is not easy as it may appear. Indeed, if L refers to the distance between the outer surface of the spallation target and the detector (along L the neutron speed is constant) and can be easily measured in principle (even if it is not the case as will be seen), the evaluation of the corresponding time of flight ΔT is not so immediate. It is expressed as the difference:

$$\Delta T = \Delta t_{obs} - t_m. \tag{2.3}$$

Δt_{obs} represents the time interval between the arrival of the proton beam on the target (which corresponds to the time of neutron productions) and the neutron detection in the experimental area. Indeed, it can be measured in turn as the time difference between the neutron detection (t_s) and the PKUP signal: (t_{PKUP})

$$\Delta t_{obs} = t_s - t_{PKUP} + t_0, \tag{2.4}$$

with an offset (t_0) due to the different cable lengths that will be determined from the measurement of the γ-flash time in section 4.2. Conversely, t_m represents the time spent by the neutron in the target-moderator assembly and cannot be directly measured, but only estimated via Monte-Carlo simulations.

Instead of using the moderation time interval t_m, in the following a more convenient formulation will be used by defining an "effective moderation length" $\lambda = v \cdot t_m$. The neutron velocity can be then equivalently expressed as:

$$v = \frac{L}{\Delta t_{obs} - t_m(E_n)} = \frac{L + \lambda(E_n)}{\Delta t_{obs}}. \tag{2.5}$$

As equation (2.5) outlines, either the moderation time t_m or the effective moderation length λ are shown by simulations to depend on the neutron energy, hence on its velocity. Therefore, time-to-energy conversion can be accurately performed only using equation (2.5) recursively until an ideal constant value for the velocity is found among subsequent iterations.

Furthermore, both t_m and λ are neither univocal functions of the energy, but statistically distributed according to the so-called *resolution function* and only its mean or most probable value at each energy are used in the equations (2.5).

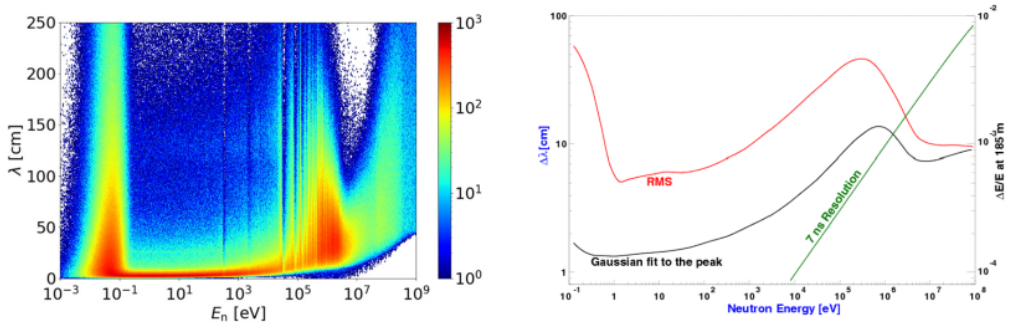

Figure 2.4: Left: the resolution function expressed as the distribution of the effective moderation length λ as function of the neutron energy for EAR1 and the second-generation target. It includes the 7 ns proton-bunch length. Simulations for the current target are still ongoing [35]. Right: the contribution of the 7 ns proton bunch length (green) and of the distribution of the effective moderation length (RMS of the distribution in red, RMS from a gaussian fit of the peak in black) reported separately as a function of the neutron energy. While the effect due to the finite bunch length dominates at high energy, that due to moderation dominates at lower ones [44].

2.3.1 The resolution function

Neutrons of the same energy, produced in the spallation target, do not travel the same length neither arrive at the same time in the experimental area. In fact, neutron moderation is a stochastic process and therefore neutrons follow different paths in the target-moderator assembly [35]. The resolution function describes exactly the probability distribution of the effective moderation lengths $\lambda(E)$ or equivalently of the moderation time $t_m(E)$ for each given neutron energy; it can be expressed equivalently in term of lengths or time according to the conservation of probability [50]. The resolution function is the convolution of different contributions, such as the finite duration of the primary proton bunches, the neutron transport in the samples and in the detectors, but the moderation contribution far dominates in most of the spectrum [49]. The resolution function cannot be directly measured, therefore it is determined via Monte-Carlo simulations of the neutron transport in the target-moderator assembly and indeed strongly depends on its characteristics. The graphical representation in Figure 2.4a shows that it is a non gaussian and rather asymmetric distribution whose shape depends on the neutron energy.

An accurate knowledge of the resolution function is particularly important in the resonance analysis. In particular, its mean or peak value at each energy account for energy shifts of resonances and are indeed employed in the equation (2.5) for

an overall accurate time-to-energy calibration. On the other hand, the shape and the spread of the distribution are responsible for broadening the resonance shapes and are employed in estimating the overall energy resolution.

Indeed, taking the derivative of equation (2.2) and considering the uncertainty related to the measurement of velocity according to equation (2.5), the overall energy resolution can be evaluated as

$$\frac{\Delta E}{E} = \gamma(\gamma+1)\frac{\Delta v}{v} = \gamma(\gamma+1)\sqrt{\left(\frac{\Delta L_{eff}}{L_{eff}}\right)^2 + \left(\frac{\Delta t_{obs}}{t_{obs}}\right)^2} \tag{2.6}$$

where the L_{eff} stands for the sum $L + \lambda(E)$. ΔL_{eff} is exactly dominated by the uncertainty on the effective moderation length $\Delta\lambda(E)$ given by the resolution function and is dependent on the neutron energy. The time uncertainty is dominated by the 7 ns duration of the primary proton bunch. As shown in Figure 2.4b, the former is the main limiting factor at low neutron energy, while the latter at high neutron energy.

According to the equation (2.6), it can be eventually concluded that long flight paths L can considerably improve the energy resolution, but at the price of a lower neutron flux, that depends on the inverse square of the target distance. The distance between the spallation target and the experimental areas is then a compromise between these two factors and the different distances of the two n_TOF experimental areas were indeed chosen to be complementary, as will be explained in the next section.

2.4 The experimental areas

2.4.1 EAR 1

The first experimental area EAR1 [44, 50] is placed underground between 182.3 m and 190.2 m from the spallation target. A stainless steel vacuum beam line with reducing diameter departing from the spallation target leads neutrons to it. The beam line is tilted 10° with respect to the incoming primary proton beam to reduce the background of charged particles and photons, produced in the first step of the spallation process mainly in the forward direction, arriving in the experimental area. At the same time, this relatively small angle still allows the most energetic neutrons to reach the experimental area, ensuring one of the distinctive features of EAR1: the wide available neutron energy range from 25 meV to approximately 1 GeV.

Along the beam line different iron and concrete shieldings, a filter box, a sweeping magnet and two collimators are present, listed in Figure 2.5a. The filter

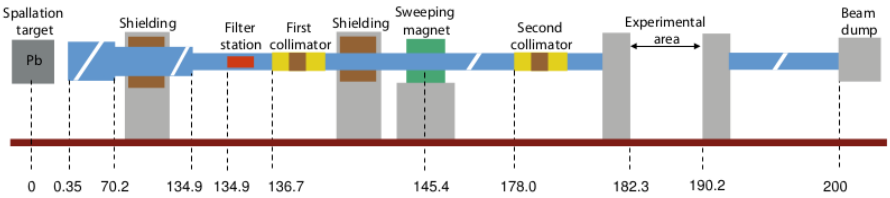

(a)

(b)

(c)

Figure 2.5: Elements along the beam line towards EAR 1. Top: sketch of the beam line [50]. Left: the old sweeping electromagnet (green) and the new permanent SmCo sweeping magnet (blue). Right: the new second movable collimator system, including the fission and the capture collimators.

box, placed just before the first collimator at 135 m from the spallation target, contains different filters made of materials with strong neutron resonances capable of completely filtering out the beam at the corresponding energy. They can be remotely moved in and out of beam and are used to study the background. The sweeping magnet at 145 m, currently a SmCo permanent magnet shown in Figure 2.5b, is used to reduce the background of charged particles in beam, by deflecting them out. On the other hand, the collimators shape the neutron beam and are placed respectively at 137 m and 178 m (just before the experimental area) from the spallation target. They are made of blocks of stainless steel and borated polyethylene to stop the non collimated neutrons. The first collimator has an inner diameter of 11 cm, while the second one can be changed to accommodate the needs of each measurement: the fission collimator has an inner aperture of 80 mm, while the capture one of 18 mm. This second collimator was upgraded during the last shutdown to enhance the reproducibility of the position between capture and fission configurations, as well as to reduce the time needed for its exchange and to

further reduce the photon background in EAR1 [51]. It is shown in Figure 2.5c.

Due to the huge distance from the spallation target, the neutron beam in EAR1 is characterized by an excellent energy resolution ranging between $10^{-2} < \Delta E/E < 10^{-4}$, but lower than 10^{-3} in most of the energy range, particularly in the resonance region. Furthermore, its instantaneous intensity was about $2{\cdot}10^5$ neutrons/bunch/cm^2. Given this features of the beam, EAR1 is particularly suited for high resolution measurements of reaction cross sections on stable or long-lived ($t_{1/2} > 100$ y) radioactive isotopes [38].

At the end of the beam line, the beam dump (a 49×49×47 cm^3 block of borated polyethylene) is placed 12 m after EAR1 in an other room to reduce the photon and the backscattered neutron background in the experimental area.

2.4.2 EAR 2

The second experimental area EAR2 [52] is placed at the ground level at 18.2 m above the spallation target. Similarly to EAR1, the vertical beam line leading neutrons to the experimental area crosses a filter box, a permanent sweeping magnet (10.4 m from the target) and two collimators (respectively at 7.4 m and 15 m) to reduce the charged particles background and shape the neutron beam. In details, the first collimator is an iron cylinder with an inner aperture of 20 cm. The second collimator is made of different layers of steel, borated polyethylene and boron carbide approximating a conical shape with an aperture decreasing from 70 mm to 21.8 mm in order to reduce the beam divergence in the experimental area and the induced photon background. Nevertheless, the neutron beam halo is expected to diverge of 1 mm each 10 cm. The detectors for capture measurements are usually placed at 1.6 m from the ground where the neutron beam is expected with a FWHM of about 21 mm. A different geometry is available for the second collimator in the fission setup with an exit diameter of 66.7 mm: in this case the beam diameter is expected to be approximately 8 cm at the measurement position.

The neutron beam of EAR2 with respect to EAR1 has a slightly narrower energy spectrum limited to 250 MeV. Because of the shorter distance from the spallation target, it is characterized by a lower energy resolution, even if still remarkable ranging between $10^{-2} < \Delta E/E < 10^{-3}$. On the other hand, the shorter distance from the spallation target gives the advantage of a higher instantaneous neutron intensity, greater than 10^6 neutrons/bunch/cm^2 with a gain on the intensity of EAR1 of a factor 35 in the eV and keV region and of 20 above 1 MeV. The new spallation target, thanks to its flat-top geometry optimized for EAR2, is expected both to improve the flux of a factor two above a few keV and to improve the energy resolution [38].

Especially thanks to its higher neutron flux, EAR2 is complementary to the characteristics of EAR1 and particularly suited to perform measurements on small

Figure 2.6: The marble shielding on the target shielding wall in the NEAR. In the center the circular hole (closed in the picture) that drives neutrons to the experimental station can be seen.

mass samples (sub-mg), on reactions with small cross section and on radioisotopes with half-life as short as a few months. In fact, in this latter case, the background related to the radioactivity of the sample would dominate over the signals in the measurements performed in EAR1, while the higher flux of EAR2 provides an increase of the signal-to-background ratio of more than two orders of magnitude [38].

2.4.3 NEAR

The modification of the shielding around the spallation target, implemented during the shutdown to inspect and replace the target, allowed the setup of an experimental station very close to the target called NEAR [53]. Due to the proximity of the target, the main feature of the neutron beam expected in the NEAR is the high intensity, exceeding 10^8 neutrons/bunch/cm^2. The measuring point is placed just behind the target shielding wall and it is equipped with a further shielding made of a marble layer, shown in Figure 2.6. Neutrons are lead there simply through a hole in the shielding wall that can be equipped with suitable and movable collimator/moderator and filtering systems. Multifoil activation measurements on extremely small-mass samples and on radioactive isotopes can be performed through irradiation at the NEAR measuring point and further off-line analysis using a High Purity Germanium detector (HPGe). In particular, suitable moderator and filters

can be chosen in order to reproduce the Maxwellian neutron spectra found in the stars or the neutron spectra found in fission and fusion reactors to carry out relevant measurements in the field of astrophysics and advanced reactor technology.

In addition to this experimental measuring point (called NEAR OUT) placed at approximately 3 m from the spallation target, two additional irradiation points have been realized [54]. One (NEAR IN) is directly attached to the target vessel to perform long-term irradiation to test the behaviour of non-metallic materials (as grease, oil,...) used in accelerators and experiments under intense radiation fields. The other is placed on the wall behind the shielding, after the NEAR OUT point in front of the hole driving neutrons. It is mainly used to irradiate and test the behaviour of electronics in neutron fields.

So far, tests and preliminary characterizations were performed during the commissioning of the new spallation target and a dedicated commissioning is going to be carried out.

2.5 The Data AcQuisition system (DAQ)

The n_TOF data acquisition system [55] was last upgraded in 2014 and is aimed at the digital acquisition of the detector output signals through flash analog-to-digital units. It consists of about 140 acquisition channels with a 12 to 14-bit resolution working simultaneously at sampling rates up to 3600 MHz for time acquisition windows up to 100 ms. This is indeed the time taken by thermal neutrons to reach the first experimental area. Overall, the amount of data to be handled by the DAQ can reach peaks of several GB/s.

In details, its architecture consists of three different chassis (the so-called DAQ units) per experimental area. They are equipped with a host controller running Linux CentOS 7 and house up to six Data Acquisition Cards (DAC) as well as a high writing speed local storage, able to sustain the raw data bandwidth related to the maximum acquisition time window and to guarantee a data buffer. The DACs are SPDevices ADQ412DC and ADQ14DC-4C modules each one providing 4 acquisition channels. They digitize input analogic signals with a maximum sampling frequency of 1.8 GHz (4 channels) or 3.6 GHz (2 channels) for the first model and 1.0 GHz for the second one with a resolution of 12 and 14 bits respectively. For both models the input full scale can be set from a minimum of 0.1 V or 0.05 V to a maximum of 5 V peak to peak and an offset can be additionally set within the full scale range. All these settings can be configured remotely from the Graphical User Interface running on the computers both in the experimental areas and in the control room. In particular, the sampling rate and the time acquisition window can be set separately for each DAC, while the full scale and the offset even for each acquisition channel.

Furthermore, the "Beam" or "Calibration" DAQ operation modes can be set. In the first case, the DAQ is synchronized with the PS that sends a digital signal in correspondence of the proton beam extraction towards n_TOF simultaneously triggering all the DACs: it is the already mentioned PS trigger. This signal is distributed to the trigger input of each DAC by a fan out buffer in order to ensure the same timing delay for each card, a crucial issue especially in the detection of signal coincidences exploited in this thesis. In the second case, an internal trigger is generated at the frequency specified by the user. It can be used in order to calibrate the detectors without the beam.

The raw data obtained consist in the sampled analogue waveforms of the detector output signals in the whole time acquisition window and for each neutron pulse. They are temporarily written to the local storage, that can supply a data buffer for 3 days of acquisition in nominal conditions, and later transferred to the CERN Advanced STORage manager (CASTOR) where they are stored and can be retrieved for the subsequent off-line processing and analysis.

In order to reduce the amount of the stored data, a fast "zero suppression" algorithm is also implemented after the acquisition to discard much of the background. In details, it can be configured from the GUI for each acquistion channel setting an amplitude threshold on the leading or falling edge of the signals and the number of pre-samples and post-samples to memorize.

The DAQ system GUI also enables to remotely monitor and configure the voltages powering the detectors and the operation of the filter boxes along the beam lines.

2.6 The Pulse Shape Analysis (PSA)

The *Pulse Shape Analysis* (*PSA*) is the first step of the off-line data analysis and consits in processing the raw data in order to extract information as the amplitude, the area and the arrival time of pulses from the digitized waveforms. These information are eventually written and stored in ROOT files ready for the analysis.

At n_TOF this procedure is based on a common generic routine [56, 57] capable of being applied to the different type of signals from variety of detectors. To reach this universality, this routine is characterized by a minimal number of explicit assumptions about the nature of signals and indeed 23 parameters have to be set externally for each detector in order to carry out the processing. This routine can be decomposed in three steps respectively aimed at the signal recognition, at the baseline computation and finally at the extraction of the output information.

The first step is based on the discrete signal derivative d, computed in each

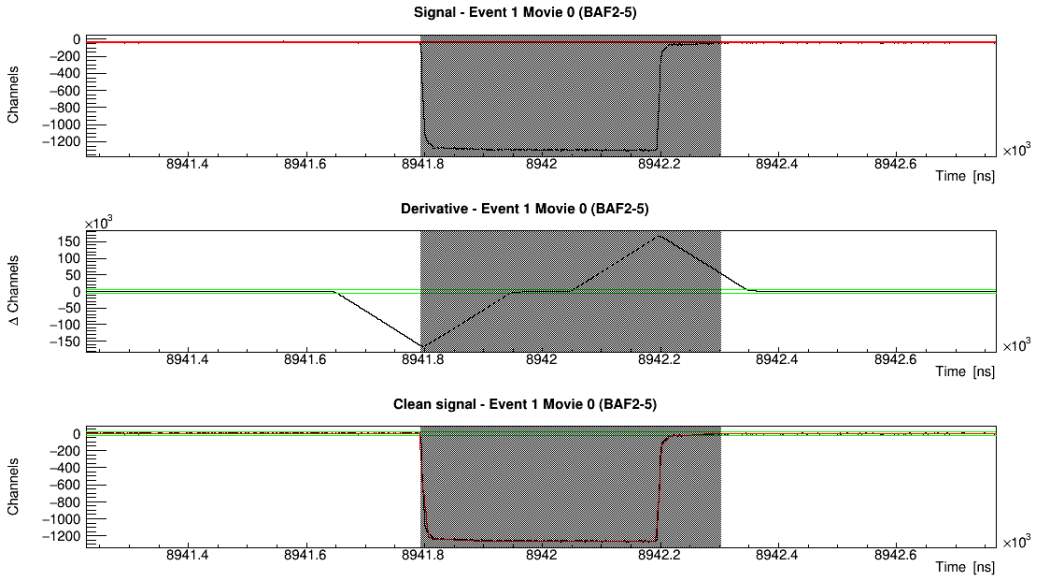

Figure 2.7: Graphical outcome of the PSA of a square signal from the DAQ Commissioning. In the top panel the original signal is shown with the baseline in red, the second panel shows the computed signal derivative with the two thresholds in green and in the bottom panel the red line represents the final result obtained by fitting the pulse with a customized shape.

point i according to:

$$d_i = \sum_{k=1}^{N} (s_{i+k} - s_{i-k}) \tag{2.7}$$

considering N samples with signal s_j at both the sides of the point i. The step-size N is one of the parameters that have to be set externally considering that a step-size larger than the period of noise in the waveform, but smaller than the characteristic pulse length, results in a smoother derivative improving the signal-to-noise ratio. Pulses are recognized when the derivative crosses two consecutive times an upper and a lower thresholds, defined by default as ± 3.5 times the root mean square of the derivative baseline noise. The use of the derivative instead of the signal itself make it possible to disentangle the pulse recognition from the baseline variation and to identify more easily pile-up. Constraints in terms of the signal width can be applied in this step to preliminary suppress background.

The second step takes into account the parts of the waveform not classified as signals in the previous step and making their average calculates the signal baseline. Different methods are actually implemented to calculate the baseline: the constant baseline method described above is the most frequently applied, followed by the "weighted moving average" method for the evaluation of adaptive baselines

mainly in the initial region of the waveform where distortions due to the γ-flash usually occur.

Finally, in the third step the signal amplitude is evaluated over the baseline by finding the maximum height of the pulse, by a parabolic fitting at the top of the pulse or even by fitting the entire pulse with a customized shape (Pulse Shape Fitting). Hence, the signal area is evaluated by integration and the time of the signal is determined as the time when the signal crosses a fixed fraction of its amplitude (30% by default). All the other useful information for the analysis can be extracted in this step and written in the output ROOT file. A preliminary selection on signal area and amplitude can be additionally performed to reduce the amount of saved background. An example of processed signal can be found in Figure 2.7.

Chapter 3

Commissioning

The n_TOF facility, described in the previous chapter, provides neutron beams with complementary characteristics in the two (near future three) experimental areas. The accurate measurement of neutron cross sections requires these neutron beams to be well characterized. For this reason, in addition to a dedicated detector continuously monitoring the neutron flux, an extensive measurement campaign, the so-called *commissioning* phase, was performed as first step after the installation of a new spallation target.

During the commissioning, the neutron beams are fully characterized in terms of neutron flux, spatial beam profile, kinetic energy distribution, resolution function for time-to-energy calibration and background. Experimental measurements are additionally flanked by Monte Carlo simulations performed in FLUKA and MCNP in order to predict the beam characteristics and to provide the non measurable quantities such as the resolution function. This information is indeed essential for the planning and the accurate analysis of the measurements to be carried out in the subsequent experimental campaigns.

This work deals with the commissioning of the third n_TOF spallation target that took place between July and November 2021 [51]. More in detail, a first phase of the commissioning was devoted to the measurements aimed at the characterization of the flux, the beam profile and the kinetic energy distribution. This is the focus of this work and will be trated in details in the following. A second phase was devoted to the measurements of well known isolated resonances, such as those present in the ^{197}Au or ^{56}Fe neutron capture cross sections, aimed at the validation of the simulated resolution function. These capture data can be also used to estimate the background.

3.1 Detection of neutrons

Despite of the advantages of the electrical neutrality of neutrons in fundamental nuclear physics discussed in the first chapter, a disadvantage regards their experimental detection.

In fact, neutrons cannot produce direct ionizations as in the case of charged particles, thus cannot be directly detected. Conversely, they are indirectly detected using *converters*, i.e. materials where, through nuclear reactions, neutrons are "converted" in charged particles or γ rays which can be detected by the common radiation detectors [58, 59].

Converters are chosen according to the energy of the neutrons to be detected according to the reaction cross section value at the energy of interest and the Q-value. In fact, the former has an impact on the detection efficiency and therefore on the dimension of the converter, while the latter determines the energy of the reaction products [17].

For example, fast neutrons are usually detected using materials containing hydrogen: at high energy elastic scattering is usually the dominant process and only using light nuclei as targets a considerable energy can be transferred resulting in a recoil charged proton that can be detected. For instance, this is the working principle of the *Recoil Proton Telescopes* (*RPT*), recently used at n_TOF indeed for the measurement of the neutron flux in the measurement of ^{235}U(n,f) cross section at high energy [17].

Conversely, slow neutron detection usually exploits nuclear reactions in light nuclei, whose cross sections go with $1/v$ (being v the neutron velocity) and do not present resonances up to hundreds of keV or even some MeV. Among the most exploited reactions providing the needed conversion characteristics are the ^{10}B(n,α)^{7}Li and the ^{6}Li(n,α)^{3}H. The former releases an α particle and a lithium nucleus in its ground state or in an excited state with a total kinetic energy of approximately 2.5 MeV. The latter releases an α particle and a tritium nucleus with a higher Q-value of 4.78 MeV, but a lower cross section. These reactions can be also used to detect fast neutrons previously slowed down in a moderator, but loosing the information on the initial energy.

Neutron induced fission in ^{235}U is an other exploitable conversion reaction especially efficient at thermal energy and in the high energy region (above 20 MeV). In fact, the ^{235}U(n,f) cross section, already shown in Figure 1.7, also presents the typical $1/v$ behaviour and is rather high at low energy, exceeding 580 b in the thermal region. Moreover, it is characterized by an extremely high Q-value (around 200 MeV) that makes the emitted fission fragments easily detectable, also because of their large electric charge. Due to the importance of neutron induced fission reaction in this thesis, refer to section 1.1.3 for a more detailed description.

Another technique of neutron detection, mentioned regarding the NEAR sta-

Table 3.1: Neutron cross sections standards and corresponding energy intervals according to the 2017 release [61]. Those denoted with (*) are used in the n_TOF flux evaluation.

	Cross section	Energy range standard
	^{1}H(n,n)	1 keV - 20 MeV
	^{3}H(n,p)	0.0253 eV - 50 keV
(*)	^{6}Li(n,t)	0.0253 eV - 1 MeV
(*)	^{10}B(n,α); ^{10}B(n,$\alpha\,\gamma$)	0.0253 eV - 1 MeV
	C(n,n)	10 eV - 1.8 MeV
(*)	^{197}Au(n,γ)	0.0253 ev, 200 keV - 2.5 MeV
(*)	^{235}U(n,f)	0.0253 ev, 150 keV - 200 MeV
		(reference in 200 MeV - 1 GeV)
(*)	^{238}U(n,f)	2 MeV - 200 MeV

tion, is the *activation technique* [60]. In this case the "neutron converter" is a sample of material irradiated in-beam and consequently activated by neutron captures. The resulting radionuclides decay releasing γ rays that are typically detected by high-energy resolution detectors as for instance HPGe. Measurement of the induced activity determines the number of the radionuclides produced, that in turn, knowing the cross section responsible for their production, leads to the measurement of the neutron flux. The difference with the other methods is that the measured radiation is not prompt.

Neutron cross section standards

The common drawback of all these different neutron detection methods lies in the dependence on an intermediate converter reaction. The cross section of this reaction needs to be known with particular accuracy both in terms of absolute value and dependence on energy. In fact, it can be the limiting factor when an accurate evaluation of a neutron flux as function of energy is sought (as in the case of n_TOF) and affect the measurement of the cross sections.

For this reason, a set of reaction cross sections independently evaluated with a particular good accuracy in some energy intervals is defined: they are the so-called *Neutron Cross Sections Standards* [61], reported in Table 3.1. The energy interval where each reaction is defined as standard usually corresponds to the energy regions where the cross section has a smooth behaviour and does not present resonances (that are indeed difficult to evaluate with high precision).

These standard cross sections are used as reference for the accurate evaluation of neutron fluxes and consequently for the measurement of all the other neutron

cross sections. In summary, measured cross sections are not expressed in absolute terms, but relative to the standards.

3.1.1 The neutron flux

The neutron flux was already generally defined in the first chapter as the number of neutrons flowing per unit time across a unit area. However, in pulsed neutron sources such as n_TOF it is more convenient to redefine the neutron flux $\Phi(E)$ as the number of neutrons per incident proton pulse (neutrons per bunch) and integrated over the full spatial beam-profile arriving at the experimental areas with a given energy E [62]. From now on the term "flux" will refer to this latter definition.

Since neutron detection needs a converter, the flux can be calculated introducing the *yield Y* of the converter reaction, that is the fraction of the total impinging neutrons converted by the nuclear reaction [50, 63]. This yield can be experimentally evaluated as:

$$Y_{exp} = \frac{C - B}{\epsilon \cdot \Phi}, \tag{3.1}$$

where C and ϵ are respectively the total detected counts per neutron bunch and the efficiency of the detector used. B are the counts due to the background that have to be subtracted from the total number of counts.

On the other hand, theoretically the yield does not depend on the neutron flux, but only on the areal density of nuclei in the target n and on the neutron cross sections of the converter, both the total σ_t and that referred to the conversion reaction σ_r. It can be expressed as:

$$Y_{th} = (1 - e^{-n\sigma_t})\frac{\sigma_r}{\sigma_t}, \tag{3.2}$$

where the term in brackets accounts for the total number of reacting neutrons in the target, while the term outside brackets for the fraction of the reacting neutrons that undergo the particular conversion reaction. In the case of thin targets, the exponential can be Taylor expanded at first order and the theoretical yield becomes even independent on the total neutron cross section according to:

$$Y_{th} = (1 - e^{-n\sigma_t})\frac{\sigma_r}{\sigma_t} \approx n \cdot \sigma_r. \tag{3.3}$$

The accuracy of this approximation is of the order of 0.01% for the targets used in this work.

The comparison between the equations (3.1) and (3.3) for the experimental and theoretical yield allows the determination of the neutron flux as:

$$\Phi(E) = \frac{C(E) - B(E)}{\epsilon(E) \cdot (1 - e^{-n\sigma_t(E)})\frac{\sigma_r(E)}{\sigma_t(E)}} \approx \frac{C(E) - B(E)}{\epsilon(E) \cdot n \cdot \sigma_r(E)} \tag{3.4}$$

where the dependence on the neutron energy has been underlined for the flux, the efficiency, the cross section and the counts and where, as previously said, σ_r is usually a standard cross section.

As anticipated, substituting this formula in the "operational" definition of cross section (1.2) one obtains that the cross section measurements depend on the one used for the flux evaluation. This is why at the n_TOF facility neutron cross sections are typically not measured in absolute terms, but relative to the standard cross sections. In details, the measurements can be performed directly measuring the ratio between the number of events recorded for the reaction investigated and for the reference standard reaction, corrected for the areal density of the samples and the detection efficiency (this is the so-called *ratio method*). Since the two reactions are usually investigated simultaneously and in a very similar experimental condition (even inside the same detector), this method has the advantage of minimizing some systematic uncertainties that, affecting both measurements, cancel out taking the ratio [35].

Lethargy and lethargy units

Neutron lethargy u is defined as the logarithm of the ratio between a defined energy E_0 and the energy of the neutron E according to:

$$u = \ln E_0 - \ln E = \ln \frac{E_0}{E}. \tag{3.5}$$

This quantity is usually employed in the treatment of neutron moderation [64], where in each collision neutrons lose a fraction of their initial energy E_0 rather than a definite amount. Therefore, the difference between the logarithms of the initial and the final energy is constant. In other words, the gain in lethargy is directly proportional to the number of collisions in the moderator. Even more, a moderated neutron flux is often approximately constant in energy if expressed in lethargic units.

This is also the case of the n_TOF facility [65], where the neutron fluxes in both the experimental areas show an isolethargic behaviour between some fractions of eV and some tens of keV. Indeed, the n_TOF neutron flux is usually displayed in units of lethargy as:

$$\frac{d\Phi}{d\ln E} = E\frac{d\Phi}{dE}. \tag{3.6}$$

Moreover, because of the energy ratio considered in (3.6), the flux in lethargy units is independent on the energy units used.

Experimentally, the neutron flux necessarily is referred to finite energy bins ranging from an E_{min} to an E_{max} rather than a single energy E, the neutron flux in

lethargy units can be eventually written as:

$$\frac{d\Phi(E)}{d\ln E} = E\,\frac{d\Phi(E)}{dE} = \left(\frac{C(E) - B(E)}{\epsilon(E)\cdot n\cdot \sigma_r(E)}\right)\frac{1}{\ln E_{max} - \ln E_{min}}, \tag{3.7}$$

where E refers to the average energy of the bin and $(C(E) - B(E))/\sigma_r(E)$ refers to the counts in the bin, each divided by the cross section at the corresponding energy.

Anticipating the data analysis section, where the bin width is chosen constant in a 10-logarithmic scale defining a number of bins per decade bpd, the natural logarithmic difference between the limits of the bins can be written as:

$$\ln E_{max} - \ln E_{min} = \ln 10^{1/bpd} = (bpd\cdot \log e)^{-1} \tag{3.8}$$

and consequently:

$$\frac{d\Phi(E)}{d\ln E} = E\,\frac{d\Phi(E)}{dE} = \left(\frac{C(E) - B(E)}{\epsilon(E)\cdot n\cdot \sigma(E)}\right)\cdot bpd\cdot \log e \tag{3.9}$$

This is the formula that is used for the flux evaluation in lethargy units in each energy bin.

3.2 Commissioning of the neutron beam

As already mentioned, the commissioning phase is aimed at the characterization of the neutron beams in both the experimental areas. As anticipated, this section deals with the details of the experimental setup of the first phase of the commissioning, focused on the determination of the neutron flux and the spatial beam profile.

On the model of the previous commissioning of the experimental areas [62, 63], three different neutron standards were used to cover the whole energy spectrum of the n_TOF neutron beams: ^{6}Li(n,t)α, ^{10}B(n,α)^{7}Li and ^{235}U(n,f). The energy intervals where their cross sections are standard are again shown in the table 3.1 where these reactions are highlighted. Neutron induced fission of ^{235}U, designed by the IAEA as a *high energy reference fission cross section*, was also employed in the energy range between 200 MeV and 1 GeV, where no cross section standards are defined.

A lot of precautions were taken in order to identify and possibly correct systematic uncertainties affecting the detection systems and/or the analysis procedure and eventually improve as much as possible the final accuracy on the flux evaluation.

In fact, it is important to note that the energy intervals where the different converter reactions have standard cross sections always at least partially overlap. In particular, this occurs at thermal energy and between 0.15 MeV and 1 MeV with all the three reactions and for boron and lithium reactions in their whole standard energy range. This allows the comparison, the combination and the normalization of the results obtained, for the same energy interval, with different methods and reactions. For the same purpose, in the energy regions where only one reaction has a standard cross section, different detectors based on the same reactions are employed. This is the case for energies above 1 MeV where two or three ^{235}U fission detectors are used: MicroMeGaS [66], PTB [67] and PPAC [17, 68]. The only exception is at energies higher than one hundred MeV where only the PPAC supplies reliable results due to its insensitivity to the γ flash.

In order to allow the detectors to run simultaneously during the measurement, all their components placed on the beam, such as samples, backings, electrodes or windows, must be as thin as possible. This guarantees the highest possible neutron transmission, as well as a low induced background in the experimental area. Nevertheless, the beam attenuation in each detector can be evaluated through the accurate knowledge of the amount of all the isotopes present in the detector and their total neutron cross sections. The corresponding correction in the data analysis can be as high as 3% of the flux value, especially at thermal energies [65].

In each detector the neutron flux is independently evaluated as function of energy using the formula (4.4). If the importance of the accurate knowledge of the neutron converter cross section σ_r as a function of the energy has been already discussed in details providing standards and references, the energy dependence of the detector efficiency $\epsilon(E)$ is a crucial parameter as well. In fact, they both contribute equally to the evaluation of the neutron flux.

The evaluation of the absolute neutron flux is additionally carried out through the activation measurement of two irradiated gold foils in the second phase of the commissioning [63].

The convolution between the results of the different detectors, combined in the overlapping regions, together with the Monte Carlo simulations results in the so-called *evaluated flux*.

In the end, the experimental setup chosen for the flux measurement in EAR1 consists of a SiMon housing a ^{6}LiF target, a PPAC monitor, a MicroMeGaS detector equipped with a ^{235}U and a $^{10}B_4C$ target and the PTB detector, placed in this order along the neutron beam. Both the PPAC and the PTB are equipped with ^{235}U targets.

Similarly, in EAR2 the experimental setup includes, in order, SiMon, a MicroMegas detector and a PPAC monitor. The targets housed in each detector are made by the same materials discussed for EAR1, except for PPAC that here is equipped with a ^{238}U target beside a ^{235}U target.

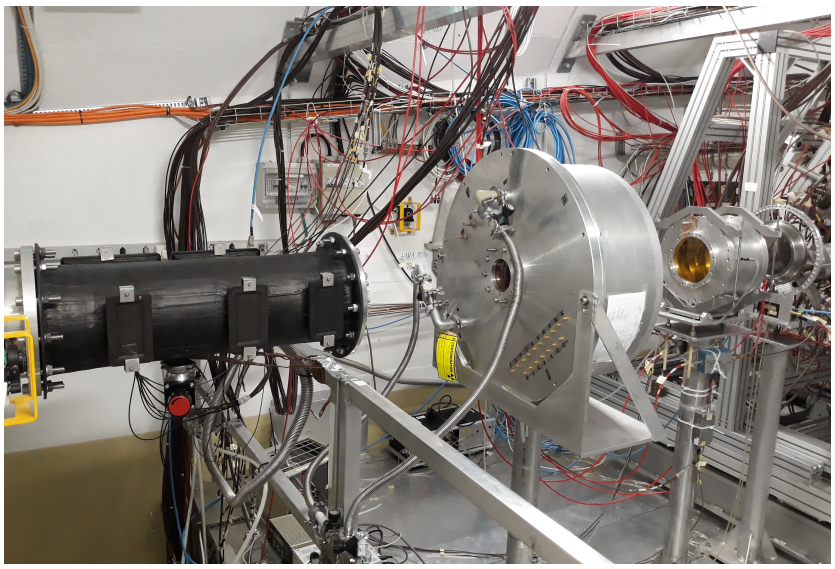

Figure 3.1: The experimental setup in EAR1 during the first phase of the commissioning. From the left to the right: SiMon (black chamber), the PPAC Monitor, the MicroMeGaS detector and the PTB detector.

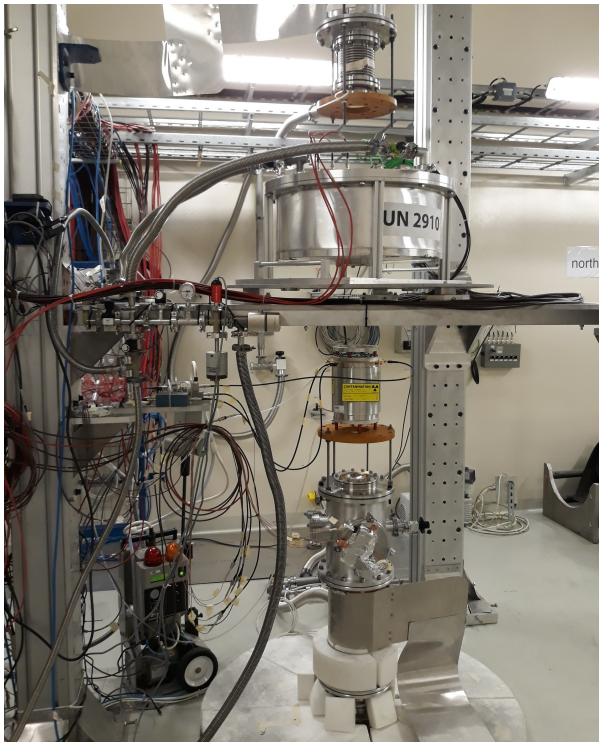

Figure 3.2: The experimental setup in EAR2 during the first phase of the commissioning. From the bottom: SiMon, the MicroMeGaS detector and the PPAC Monitor.

In both the experimental areas the capture collimator was mounted in this phase, with an exit diameter of 21.8 mm and 18 mm in EAR2 and EAR1, respectively. Borated water was used as moderator for EAR1, while demineralized water for EAR2.

The Figures 3.1 and 3.2 show the described setups.

In this phase, the spatial beam profile, the other focus of this work, is reconstructed from the data collected by the PPAC monitors in both the experimental areas. In fact, as will be described in details, beside counting the fission reactions, these detectors are also capable of reconstructing the positions where fission occurs, hence the impact position of neutrons.

In conclusion, just few words about the setup in the second phase of the commissioning. As anticipated, it is mainly devoted to the validation of the resolution function through the comparison between the simulated and the measured shapes of some well-known neutron resonances. Four liquid C_6D_6 scintillators, particularly suited for neutron capture measurements, were placed out of the beam around a in-beam target.

A detailed descriptions of the detectors employed and here only mentioned can be found in the following sections with a particular emphasis on the PPAC, whose data analysis is the subject of the next chapter and thus deserving the exclusive section 3.3.

3.3 Parallel Plate Avalanche Counters (PPAC)

Parallel Plate Avalanche Counters [17, 68] are gas detectors that operate in proportional mode thanks to the choice of the gas pressure and of the electric field.

PPACs, as the name suggests, employ thin plates in a parallel configuration as electrodes (Figure 3.3). In particular, a central anode at high positive voltage is flanked by two grounded cathodes placed at a small distance along which a homogeneous constant electric field up to 10^6 V/m is created. In this configuration the avalanche region occupies the full gap between the electrodes producing a worse energy resolution with respect to the common proportional counters, but, since the gap is kept as small as possible, very fast timing response and excellent time resolution even below ns are reached [58].

In the case of the PPACs used in this work [17], built at the *Institute de Physique Nucléaire d'Orsay* (France), both the anodes and the cathodes consist of 1.7 μm thick mylar foils coated by evaporation with 700 nm of gold to make them conductive and with an active area of 20 cm $\times$ 20 cm. The anodes are connected to a high voltage chosen in order to maximize the signal amplification without saturate the acquisition system. In particular, for the PPAC used in EAR1 it ranges between 580 and 600 V, while in EAR2 from 500 to 520 V, correspond-

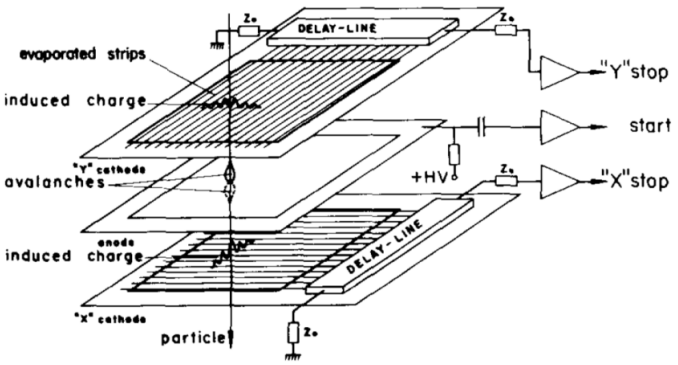

Figure 3.3: Sketch of a PPAC: a central anode at HV surrounded by two stripped grounded cathodes. The electric field in between is responsible for the formation of electronic avalanches. From [69].

ing to electric fields around 10^5 V/m. The gap between the electrodes is 3.2 mm and is filled by octofluoropropane (C_3F_8) at a pressure of 4 mbar, a gas providing a high gain and fast signal risetimes.

3.3.1 The working principle

The working principle of PPACs is the same as other proportional counters [58, 64]. An ionizing particles that enters the detector ionizes the atoms of the gas producing ion-electron pairs. Due to the electric field between the electrodes, electrons and ions drift respectively towards the anode and the cathodes with different mobility determined by their mass: electrons are indeed approximately hundred times faster than ions. When the electric field is high enough, in the so-called avalanche region, the primary electrons can gain sufficient energy to ionize other gas atoms along their path, freeing additional electron-ion pairs that in turn can trigger further ionizations. This multiplication process results in the proportional amplification of the original signal through the formation of a *Townsend avalanche*, where the number of electrons is proportional to the energy deposited by the primary particle.

As anticipated, the main disadvantage of the PPAC with respect to the cylindrical counters lies in the fact that the electric field between the electrodes is constant and therefore the avalanche region occupies all the gas volume. In this way, the avalanche amplification gain does not only depend on the energy deposited, but also on the position where the primary ionization occurs. Therefore, the typical output signal produced by an ionizing particle crossing the detector actually consists of a mix of amplification factors due to the different positions of the primary ionizations along its trajectory. This results in a worse energy resolution, seldom

better than 20%, that however still allows the separation of different types of particles with widely different specific energy loss such as α particles and fission fragments [58].

Pulse production and timing

Talking about the output signals, it has to be underlined that they are actually produced by induction due to the drift motion of the charges, rather than by the collection of the charge itself [64].

The detector can be indeed sketched as a capacitor placed at a certain equilibrium voltage and storing a certain energy. Since the movement of the charges in the gas is faster relative to the response time of the external circuit connected to the detector, the system can be thought as isolated and its energy conserved. Therefore, the variation of the potential energy of the drifting charges must be supplied by a corresponding variation of the energy stored between the electrodes, where indeed an induced voltage perturbation, or equivalently an induced charge, appears until all the moving charges are collected. This produces the rising part of the output signal, while the time constant of the preamplification circuit is responsible for its decreasing part [58].

In principle, the signal shape should consist of a fast rising component due to the electrons, rapidly collected at the anode, and a much slower component due to the motion of the positive ions. However, for timing purpose, PPACs are usually only electron-sensitive, i.e. only the motion of the electrons contributes to the output signals in both the anode and the cathodes because the slow component is suprressed by a shorter time constant of the collection circuit. Together with the very small distance between the electrodes, this implies the excellent timing response of PPACs: the output signals are nearly immediate, characterized by a fast risetime and the resolution is on the order of nanoseconds or even less [68].

The fast time response of these detectors implies the possibility to neglect, during the analysis, corrections due to the dead time as no pile-up effects are present, at least for the count rates expected in this work in EAR1.

Detection efficiency

An other advantage of PPACs lies in the detection efficiency, especially when used to track or detect intermediate energy heavy ions such as the fission fragments.

In fact, due to their high ionization power, fission fragments of approximately 1 MeV/A energy can knock out 100 to 200 electrons when crossing the coated mylar electrodes entering the detector. These electrons act as a seed for the formation of the avalanche even before the ionization in the gas and therefore guarantee a close-to-one efficiency for fission fragment detection [68].

On the other hand, the low pressure of the gas, the small detection volume and the thinness of the electrodes make PPACs almost insensitive to long-range particles such as γ rays and minimum ionizing particles (MIPs). This is a very important advantage at the n_TOF facility, because it means that PPACs are almost insensitive to the high γ-flash signal, that conversely largely affects the other detectors and limits their performance at high energy. For this reason and for their fast time response, PPACs are indeed the only detectors among those employed in the commissioning that can detect fission signals even at very short times of flight corresponding to neutron energy up to 1 GeV.

Moreover, PPACs are suited for in-beam employment since they are not damaged by radiation and high counting rates, disadvantages usually affecting solid state detectors.

3.3.2 Determination of the position of particles

An other advantage of PPACs consists in their capability of reconstructing the X and Y position of the avalanche and therefore the position of the impacting fission fragment.

In fact, the coating of the cathodes is stripped (Figure 3.3) in 2 mm wide strips separated by a distance of 0.1 mm. In this way, since the avalanche induces a signal only in the strips closer to its position, the centroid of the charge distribution can be determined. Instead of reading each strip separately, each strip is connected to a delay line that is read out at both its ends, thus largely reducing the number of readout channels (two per cathode instead of one per strip).

The delay line consists of a 20 cm plastic rod with a coiled copper wire that propagates the cathode signals to both its ends, where it is directly connected to two integrated preamplifiers. A signal takes 100 ns to run across the whole delay line and, as the name suggests, it is exactly aimed at increasing the time difference between the two readouts of a cathode signal to improve the space resolution to 1.4 mm [17]. More details will be given in the section 4.3.

Since a PPAC is composed of two cathodes, they are stripped in orthogonal directions so that both the X and the Y position of the impacting particle can be retrieved.

In conclusion, since the cathode signals are delayed by the delay line with respect to the reference anode signal, their acquisition can follow a master-slave scheme: the detection of a signal on the anode (master) triggers the acquisition on the four corresponding cathode readouts (slaves). This reduces considerably the size of the raw data files to store.

3.3.3 PPAC Monitors setup

The PPAC Monitors used at the n_TOF facility are built in order to count fission events by detecting in coincidence the two fission fragments emitted back to back. For this reason, the elementary detection cell of these detectors consists of a central target of fissionable material surrounded by two PPACs aimed at the fission fragment detection. It is sketched in the Figure 3.4.

In particular, the detectors used in the commissioning consist of two of these detection cells, so three PPACs at a distance of 34.2 mm with two ^{235}U targets placed in between, as shown in Figure 3.5. The central PPAC is common to both the cells. The entire detectors are enclosed in a cylindrical aluminum chamber provided with two 75 μm thick kapton windows in correspondence of the beam and are positioned in order to ensure that the neutron beam impinges perpendicularly on the targets.

The detection in coincidence of both the fission fragments is a rather advantageous feature of PPAC Monitors since it allow the rejection of much of the background, mainly due to the α particles from the decay of the actinides in the targets. High signal-to-background ratios can be therefore achieved even for highly radioactive samples [35].

Furthermore, since PPACs are sensitive to the position of the fission fragments, it is possible to reconstruct their trajectory and the position where the fission reaction occurs in the targets. This is done simply connecting the impact points of the fission fragments on the two PPACs through a straight line. This procedure is actually exact only for the fissions induced by neutrons with energy lower than approximately 100 MeV. In good approximation, below this energy fission can be considered at rest and fragments emitted back to back. At higher energies this is not true due to the linear momentum transfer, even if simulations show that the procedure described above still can be applied as a good approximation [35]. In the end, this leads to the reconstruction of the neutron beam spatial profile. More details and formulae about these procedures will be given in the section 4.3.

On the other hand, the required coincident detection of the fission fragments limits the overall efficiency of the PPAC Monitors. In fact, as said, PPACs have a close-to-one efficiency for fission fragment detection and their active area is chosen not to limit this efficiency. The main limiting factor lies exactly in the fact that both the fission fragments have to reach the PPACs, in particular the forward-emitted fragment has to cross the sample backing without being stopped in it. For this reason, great efforts are made in order to realize sample backings as thin as possible, from 2 μm to even 0.75 μm thick. However, due to their high stopping power, the fission fragments emitted at large angles with respect to the perpendicular to the backings are stopped anyway. This limiting angle is usually approximately 60° and limits the overall efficiency of the PPAC Monitor to ap-

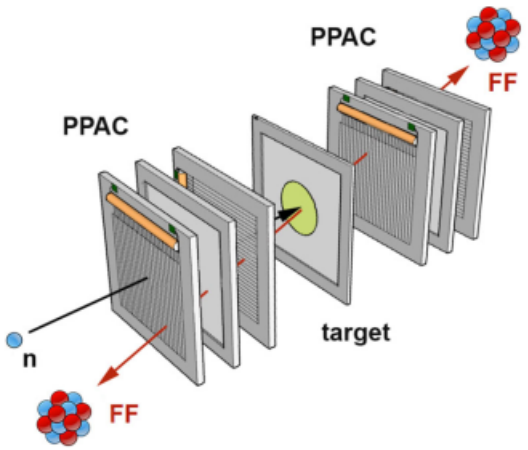

Figure 3.4: Scheme of the elementary detection cell of a PPAC monitor, made of a central target surrounded by two PPACs aimed at the coincident detection of the two fission fragments emitted back to back.

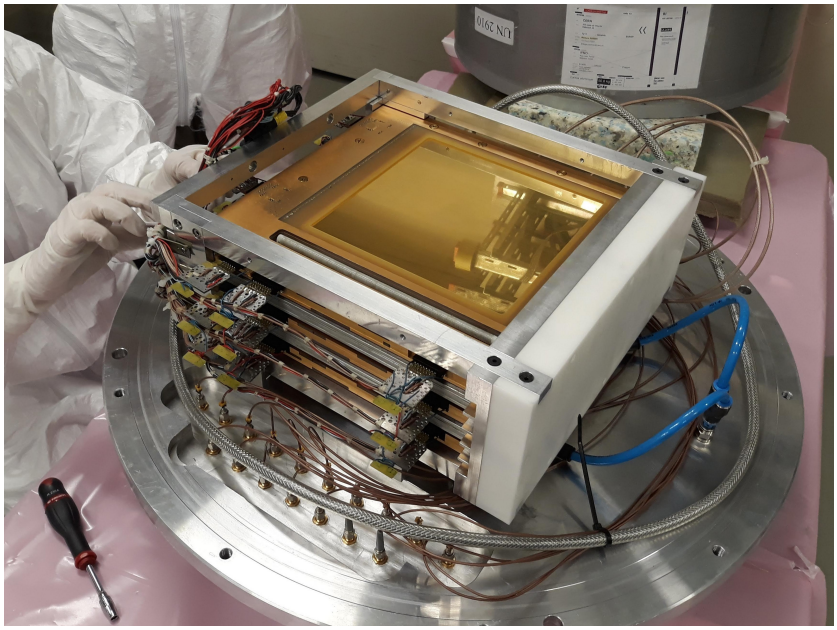

Figure 3.5: View of the PPAC Monitor, made of three PPACs with the two uranium targets in between. The connection to the integrated preamplifier can also be observed on the side as well as the delay line for one of the cathodes.

proximately 65% at maximum. The efficiency also depends on the neutron energy since it is affected by the anisotropy of the fission fragment angular distribution and by the Lorentz boost at high energies. Again, more details will be given in the next chapter.

In conclusion, some technical details: the detectors are powered by three different high voltages (from 500 V to 600 V as previously said), one for each anode, and by a common low voltage (6 V) supplied by a dedicated generator for the integrated preamplifiers. They use 15 acquisition channels, corresponding to the three anodes and the four cathode readouts per anode, in a master-slave configuration.

Description of the targets

Two ^{235}U targets produced at the IPN d'Orsay (Figure 3.6) were used at EAR1 [17]. They consist of 14 mg of uranium deposited as a thin 80 mm diameter circular layer over a 2 μm thick aluminum foil. The resulting average areal density is 280 μg/cm^2 or equivalently $4.17 \cdot 10^{-7}$ at/barn.

The method of molecular plating was used to create the uranium deposition on the target. In details, uranium nitrate is dissolved in isopropyl alcohol with a small amount of water, then a difference of potential is applied to obtain the electrodeposition of the element on the aluminum support, employed as electrode. The target is stoved to remove residual alcohol and water. The resulting deposits are in the form of uranium dioxide (UO_2).

After preparation, the deposits were characterized in terms of isotopic composition by a mass spectrometry analysis and one of them even in terms of thickness by counting the α radioactivity in different portions of the target and by Coulomb scattering of protons. The ^{235}U isotopic purity was evaluated to be 92.699(5)% (in number of nuclei), the remaining part being made of impurities of ^{238}U (6.283(6)%), ^{234}U (0.7472(15)%) and ^{236}U (0.2696(5)%) mainly. The fission cross section used for the evaluation of the flux takes into account this isotopic composition, especially at high neutron energy where the correction on the pure ^{235}U(n,f) cross section is maximum.

The targets in EAR2 are ^{238}U and ^{235}U with an average areal density of 280 μg/cm^2 and 220 μg/cm^2, respectively. Apart from the flux evaluation over MeV, the ^{238}U target is needed in EAR2 for the time-to-energy calibration, provided by the identification of the fission threshold.

3.3.4 Gas regulation

The choice of the gas and its characteristics is a crucial issue in gas detectors. In PPACs, octafluoropropane (C_3F_8) is used and it must be kept at a low pressure of 4 mbar to guarantee the correct operation of the detector. Moreover, the gas must

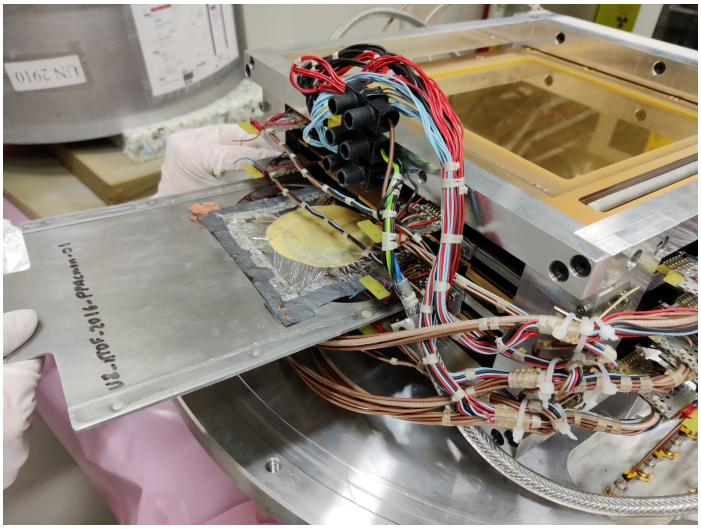

Figure 3.6: One of the ^{235}U targets extracted from the the PPAC Monitor used in EAR1.

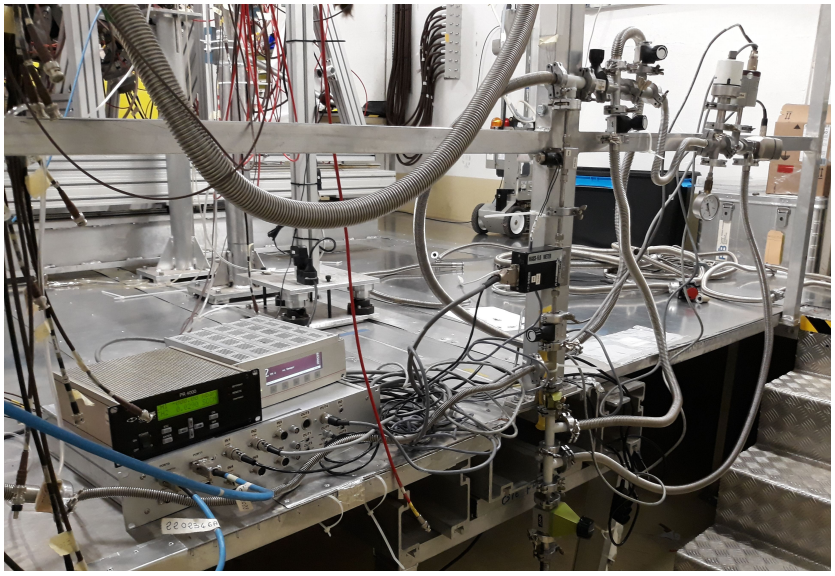

Figure 3.7: The gas regulation circuit for the PPAC in EAR1. In the foreground the Arduino Due device (bottom) with two additional modules to power the sensors. Proceeding to the right, the flow sensor and valve (placed in the vertical direction), the systems of manual valves to connect the circuit to the chamber and the pressure regulation system with the two pressure sensors (above), the mechanical manometer and the Pfeiffer EVR 116 valve. At the bottom, the green valve leads the exhaust gas to the pump.

be forced to flow at 2 to 10 sccm (standard cubic centimeters per minute) in order to evacuate the molecular radicals produced during the ionization process and the oxygen desorbed by the mylar electrodes that, if accumulated, would cause electrical discharges. The purpose of the gas regulation is exactly to maintain these constant flow and pressure in the detector.

The PPAC Monitors used in the commissioning were provided with an external dedicated and automatic gas regulation system, shown in Figure 3.7, that can be monitored and controlled remotely by PC.

In details, it consists of an upstream flowmeter and a downstream pressure sensor (a Pfeiffer TPR280 or a MKS Baratron) connected to an Arduino Due device. According to the input values given by these sensors, the device automatically regulates the aperture of a flow regulation valve (a MKS 248 A solenoid valve) and a pressure regulation valve (a Pfeiffer EVR 116 valve) in order to maintain the values set for flow and pressure, respectively . Additionally, the Arduino Due device is connected through a serial port to the PC in the DAQ area, where a dedicated software allows the monitoring and the setting of the parameters of the gas regulation, even remotely.

The gas system additionally includes other connections and two other pressure sensors sensitive to the atmospheric pressure (a simple mechanical manometer) and vacuum ranges, respectively. These are mainly employed in the preliminary operations such as purging the gas line, pumping and venting the chamber and/or the gas lines and testing the gas system.

A pump is eventually needed to keep the low pressure in the gas system and drive the exhaust gas out.

3.4 Other detectors

3.4.1 SiMon

SiMon [70, 71] (that stands for *Silicon Monitor*) is a flux monitor that uses the ^{6}Li(n,α)^{3}H reaction to detect neutrons up to 1 MeV.

It consists of an in-beam target deposited on a 1.5 μm thick mylar foil and made of ^{6}LiF The thickness of the deposit can be chosen between 10 μg/cm^2 and 400 μg/cm^2 as a compromise between the counting rate and the energy straggling in the target that can worsen the separation of the reaction products.

The tritons and the α particles from the ^{6}Li(n,α)^{3}H reaction are both detected by an array of four 300 μm thick silicon detectors (Figure 3.8), placed outside the beam some centimeters after the target and at 45° with respect to the beam direction.

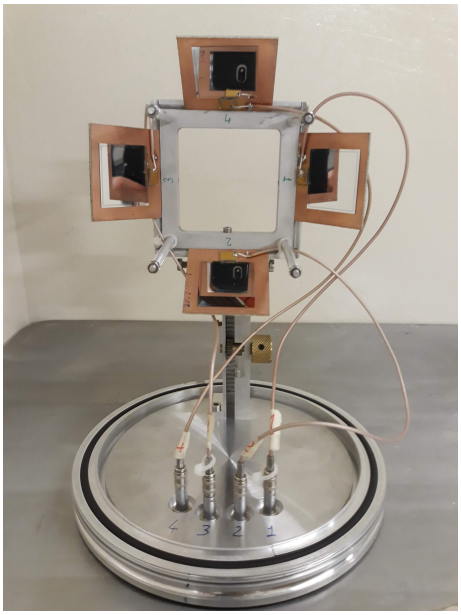

Figure 3.8: The array of four silicon detectors of SiMon2.

An overall geometric efficiency of approximately 9% below 1 keV (where the isotropy of the reaction products can be assumed) can be estimated, as confirmed by Monte Carlo simulations. At higher energy, particles are preferentially emitted in the forward direction and the efficiency increases up to 12% - 15%, but since their angular distribution is not so well characterized even the uncertainty on the efficiency raises up to 3% or more [62].

Due to the very small amount of material placed in the beam, SiMon induces a particularly low γ background in the experimental areas that makes it especially suitable as neutron monitor during (n,γ) measurement campaigns.

The detector is host in a vacuum chamber (made of carbon fiber in EAR1) to further reduce the induced background.

3.4.2 MicroMeGaS

MicroMeGaS, *Micro-Mesh Gaseous Structures*, are parallel plate proportional gaseous detectors characterized by low noise, high radiation resistance and low mass and therefore suitable for in-beam measurements and as flux monitor [66].

They consist of a gas volume divided into two regions separated by a thin (some μm) conductive micro mesh. The first 5 mm thick region is the drift or conversion region, where the charged particles lose their energy ionizing the gas. A low electric field (approximately 1 kV/cm) is applied here to enable the electron drifting. In the the second region, between the anode and the mesh and with a thickness between 25 μm and 50 μm, a larger electric field is applied (> 10 kV/cm) in order to produce the avalanche amplification of the signal. The anode and the mesh constitute a single integrated structure realized with the so-called Micro-Bulk technology, that consists in a grid of kapton pillars sustaining the copper micro-mesh produced through the chemical etching of a coppered kapton foil [72]. This technology reduces the amount of the in-beam material improving the detector neutron transparency and the induced background. The gas used is a mixture of argon, CF_4 and isobutane (iC_4H_{10}) at atmospheric pressure. In order to detect neutrons, a neutron converter material layer is deposited on the cathode.

During the commissioning, two MicroMeGaS were used in each experimental

area along the beam, one equipped with a $^{10}B_4C$ deposit on the cathode coppered kapton electrode, the other with an enriched ^{235}U deposit on the cathode aluminized mylar electrode. In the first case, either α particles or the ^7Li nuclei from the $^{10}B(n,\alpha)^7Li$ reaction are detected for the analysis of flux. In the second case only one of the two fragment from the ^{235}U fission is detected with a constant efficiency near 94% [62].

However, even with the uranium converter, MicroMeGaS cannot measure neutrons with energy higher than approximately 1 MeV because it is blinded by the γ-flash for several microseconds.

3.4.3 PTB fission chamber

The so-called *PTB detector* is a fission parallel plate gaseous ionization chamber, named after the German *Physikalisch Technische Bundesanstalt* (*PTB*) that developed it [67].

It is the only fission chamber employed in the commissioning that works in the ionization regime. This means that the output signal is given exactly by the charge produced by the primary ionizations induced by the fission fragments in the gas, without avalanche multiplication. The chamber consists of a stack of alternate six tantalum and five platinum electrodes of 0.125 mm thickness placed along the neutron beam with a pitch of 5 mm. The platinum electrodes are coated on both their sides with 500 $\mu g/cm^2$ ^{235}U deposits. Only one fission fragment per fission is detected in the gas, where the induced ionization electrons are collected by the tantalum electrodes with an efficiency of approximately 93% [62]. The gas is a mixture of argon and methane. The detector is very well characterized and usually used as reference for the absolute flux measurement in EAR1.

Platinum and tantalum are chosen to minimize the neutron beam perturbation, since they do not present particularly pronounced structures in their neutron induced cross sections. However, when they are hit by the γ-flash, they produce a large background that blinds the detector and consequently limits the detection of neutrons with energy higher than 150 - 200 MeV.

3.4.4 C_6D_6

The *C_6D_6 detectors* [73] are liquid scintillators consisting of duterated benzene (C_6D_6) and directly coupled to a photomultiplier hosted in the same carbon fibre structure. An expansion volume is also attached to the detector to allow the thermal expansion of the liquid (Figure 3.9). These detectors are largely used at the n_TOF facility to detect the γ ray cascades following the neutron capture reactions, therefore they were used in the second phase of the commissioning.

Differently from the detectors described so far, essentially counters, the C_6D_6 are *Total Energy Detectors* (*TED*). In fact, their output pulse height is related to the fraction of the γ cascade energy deposited in the scintillator. Therefore, a suitable weighting function enables the retrieval of the total energy of the γ ray cascade.

The choice of deuterated benzene is due to its excellent timing properties and to its low neutron sensitivity [74].

Figure 3.9: A C_6D_6 detector during a test in EAR1.

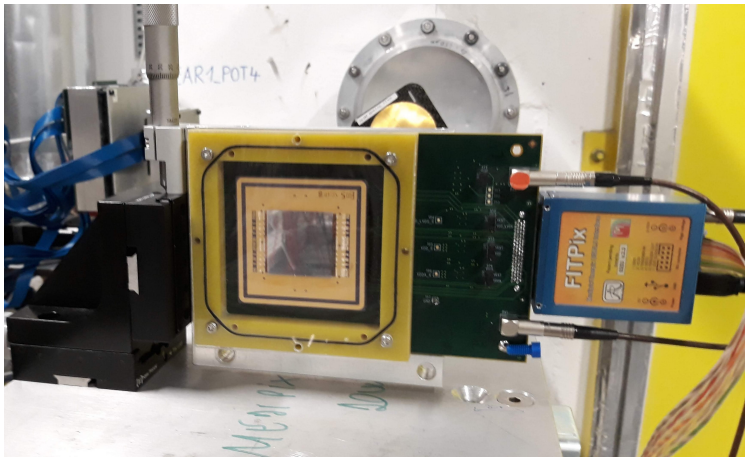

Figure 3.10: The Timepix Quad detector.

3.5 Timepix

The *Timepix* detectors [75] were used in both the experimental areas before the beginning of the physical data taking in order to identify the actual position of the neutron beam and accordingly align the detectors.

Timepix detectors were built by the Medipix2 CERN based collaboration. They consist of a pixellated silicon sensor of 256 $\times$ 256 pixels attached to an underlying specific integrated circuit. The sensor is 300 μm thick and its pixels are 55 μm wide. The electronics for each pixel includes a preamplifier, a discriminator and a digital counter, it is provided with a common external clock signal and can be configured in three different acquisition modes. In the first acquisition mode each pixel simply counts the number of hits, while the other two respectively measure the time-of-arrival of the first hit or the time-over-threshold that is related to the total energy deposited in the pixel. The acquisition thresholds for each pixel are configured performing a preliminary equalization to compensate the variations due to local transistor threshold voltages and current mismatches or more global effects like on-chip power drops.

A single Timepix detector is too small to cover the whole beam, hence in the commissioning four Timepix detectors arranged in *Timepix Quad* detector were actually used, covering an active area of 28 mm $\times$ 28 mm divided in 512 $\times$ 512 pixels (Figure 3.10). Only the counting mode was exploited. When the detector is placed in the neutron beam, produced charged particles induce electron-hole couples crossing the sensor. Due to the electric field provided by a suitable bias applied to the silicon, these secondary particles drift towards the electrodes and induce a signal in the hit pixels, usually activating a cluster of pixels. In the end, the detector counts the number of hits in each pixel in a certain time window, just as a camera. The time acquisition window as well as a time delay for the beginning of the acquisition after the trigger (that is the PS trigger) can be set by the user and can be even used to roughly select the energy of the neutrons to detect. The acquisition can be repeated over many bunches providing many superimposed photographs of the neutron beam profile. Hence, a simple and quick analysis can provide both the beam centroid with a resolution of a tenth of millimeter and the beam dimension (see section 4.3).

Moreover, since two Timepix Quad detectors are employed in each experimental area, the direction of the neutron beam and its divergence can be estimated.

Chapter 4

Data Analysis

This chapter deals with the analysis of the data from the PPAC Monitor.

As anticipated in section 3.3, each PPAC employs five acquisition channels (one for the anode and two for each cathode), for a total of fifteen acquisition channels for the three PPACs in the detector. They are set to acquire data for 100 ms after the PS trigger in order to detect neutrons down to thermal energy. The master-slave acquisition mode is used: only when the anode (master) is triggered a data acquisition window of few hundreds ns is opened for the four correspondent cathode channels (slaves).

The raw data from each channel are then processed with the PSA routine (described in the section 2.6) to recognize the signals and extract their time and their amplitude, beside other information not used in this analysis.

The analysis consists of the reconstruction of the fission events as a function of the neutron energy and of the spatial position where the reactions occur (described in sections 4.1, 4.2 and 4.3). Consequently, the spatial neutron beam profile and the detector efficiency, important information for the neutron flux determination, are measured and estimated from the experimental data (section 4.4). Finally, knowing the ^{235}U(n,f) cross section, the neutron flux as a function of energy is extracted (section 4.5).

4.1 Fission events building

The ^{235}U fission is the neutron conversion reaction exploited by the PPAC Monitors. As already anticipated, in these detectors both the fission fragments, emitted back to back, can be detected. Therefore, fission events are identified by the coincidences of two signals from the two PPACs surrounding a target. This method strongly reduces the background due to the α radioactivity of the samples and to the other neutron-induced reactions. However, one of the fission fragments some-

times can cross two detectors and this results in the observation of coincident signals in all the three PPACs. In this case, timing considerations are carried out in order to discriminate the target where the fission occurred.

Before entering into these details, it is important to outline that the search for time coincident signals in different detectors relies on the synchronization between the different acquisition channels. This is guaranteed by the n_TOF DAQ system through the common clock and the common trigger distributed in each card.

4.1.1 Anode signals coincidences

The first step for the reconstruction of the fission events consists in the search for the time coincidences in the anode signals of the different PPACs.

In details, the central PPAC is assumed as reference since common to both the detection cells. For each of its anode signals, coincident signals are searched for in the anodes of the other two PPACs, within a time window of 20 ns. If no coincident signals are found, the signal is discarded as background. Conversely, if two or more coincident signals are found in the same PPAC, only the one having the maximum amplitude is saved: this assumption relies on the fact that fission fragments are expected to deposit a larger amount of energy with respect to the other background particles.

When a coincident anode signal is found in one PPAC only, the event is saved and classified as a fission in the target surrounded by the two detectors in coincidence.

Conversely, if coincident signals are found in all the three PPACs, the event is still saved (as a multiplicity three configuration), but the identification of the target where the fission occurred requires a further analysis. Since these configurations correspond to the fission events where one fragment crosses two detectors, considerations about the detection timing in the different PPACs are exploited. In fact, the two PPACs surrounding the target where the fission occurs are expected to detect the fragments nearly simultaneously, since they have to travel the same distance. Conversely, the PPAC non-adjacent to the target is expected to detect that fission fragment with a larger delay due to the larger distance it has to cover to reach the detector. This is shown in Figure 4.1: the configurations where the absolute value of the time difference between the signals in the first two PPACs is smaller than the absolute value of time difference between the signals in the last two PPACs are classified as fission events in the first sample, otherwise they are classified as fission events in the second sample. Once the target has been identified, only the signals from the two surrounding PPACs are saved for the analysis.

Figure 4.2a is a representative result of the coincidences selection. It shows

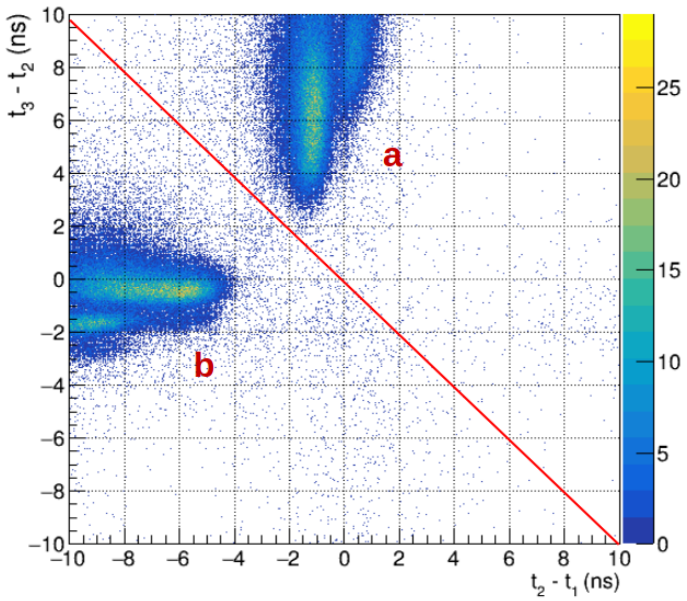

Figure 4.1: Time differences between the signals in the second and first PPAC (x) and in the third and second PPAC (y) for multiplicity three events. The red line distinguishes the fission events ascribed to the first target (a) and to the second target (b). In case (a) the signals are nearly simultaneous in the first two PPACs (t_2 - t_1 ~ 0), while considerably delayed in the third PPAC (t_3 - t_2 > 4 ns), in case (b) the opposite occurs.

the amplitude of the selected anode signals in the first PPAC as a function of the difference in time between the signals in the first two detectors. The figure also includes the fission fragments coming from the third target, that are identified and discarded.

It can be observed that, despite the coincidence technique, signals are still dominated by the low-amplitude background due to α radioactivity of the samples and to spallation reactions in the detector materials. In particular, in the first case the α particles emitted by the second target towards the central detector can cross both the central and the first PPACs producing coincidences that are saved. Since the energy of the α particles is fixed and they have to travel approximately the same distance, these events are concentrated at a specific time difference between - 9 ns < t_2 - t_1 < - 2 ns.

For what concerns spallation reactions, they are induced in the dead layers of the detectors by the high energy neutrons and charged particles reaching the experimental area. These reactions release a lot of light particles that can cross different detectors or even produce random coincidences due to their high counting rate. These reactions are mainly responsible for the background at small time of flight, while the α radioactivity contribution is constant over all the neutron

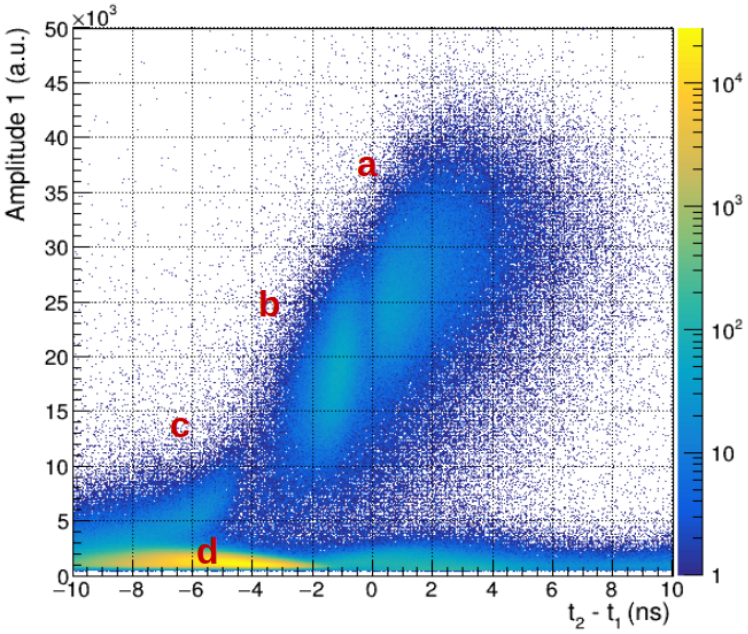

(a)

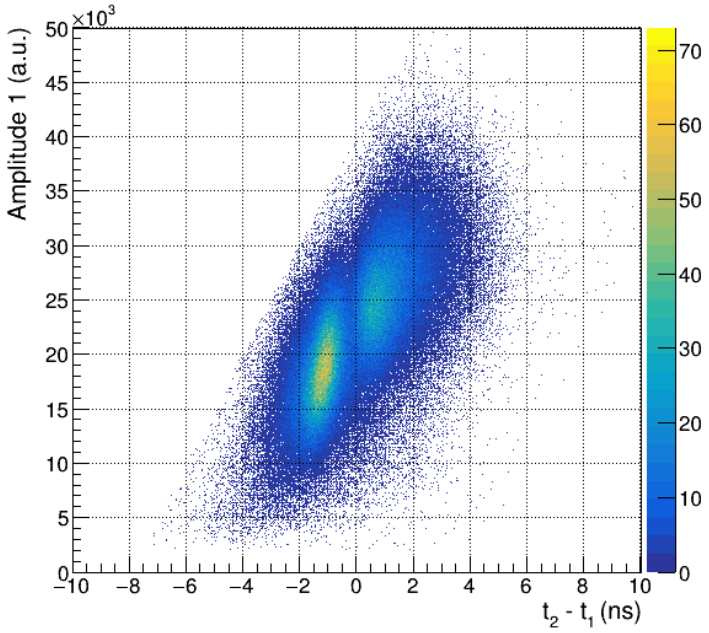

(b)

Figure 4.2: Amplitude of the coincident anode signals in the first PPAC as a function of the difference in time between the coincident signals in the first two PPACs. The two bumps corresponding to the light fission fragments (*a*) and the heavy fission fragments (*b*) can be distinguished, as well as the fission fragments (*c*) and the α particles (*d*) from the third target. Figure *b* is the result after the selection of the fission events from the first target.

energy range, as shown in Figure 4.3.

Most of the background can be easily distinguished from the fission fragments thanks to its lower amplitude, therefore it is discarded setting a suitable threshold. In particular, since the energy released in fission reactions is non-equally shared among the fission fragments, the threshold is set on the sum of the coincident signals amplitudes rather than on the amplitude in a single detector. A representative spectrum is shown in Figure 4.3 for the detectors surrounding the first target.

In order to discard the little background left over the threshold, a condition on the signal amplitude as a function of the difference in time between the coincident signals is finally applied.

Figure 4.2b shows the result of the selection conditions applied to the previous figure 4.2a: only the two regions corresponding to the fission fragments are left. In details, the left bump corresponds to the heavy fission fragments (HFF) reaching the first PPAC, while the right bump to the light ones (LFF). In fact, since the velocity of the fission fragments is inversely proportional to their mass, the heavy fragment emitted towards the first PPAC takes more time to reach the detector and consequently t_2 - t_1 gets smaller (negative) with respect to when the light fragment, faster, is emitted towards the first PPAC. Additionally, the signal amplitudes are also consistent with this interpretation: the HFF signals have an amplitude lower than the LFF signals since they deposit a smaller amount of energy, as expected. In fact, the fission fragments are characterized by a factor $\beta < 0.05$ (being β the velocity over the speed of light) where the stopping power is directly proportional to the particle velocity [58].

Of course, when the light fragment is emitted towards the first PPAC, the heavy one is emitted towards the central PPAC and viceversa and this is well reproduced by the correlation between the amplitudes of the coincident signals in the two detector surrounding the target, shown in Figure 4.4.

4.1.2 Cathode signals coincidences

Once the fission events have been selected through their anode signals, the second step involves the cathode signals. They were used for the spatial localization and the determination of the trajectory of the fission fragments, providing the neutron impact point on the targets. In addition, the cathode signals provide the angular efficiency of the PPAC Monitor.

It is worth recalling that each PPAC has two cathodes stripped in perpendicular directions surrounding the anode. Each strip is connected to a 100 ns delay line that is read out at both its ends. Therefore, four delayed cathode signals are expected for each selected anode signal within 100 ns, as shown in Figure 4.5. Since the two signals from a same cathode are produced simultaneously, the sum

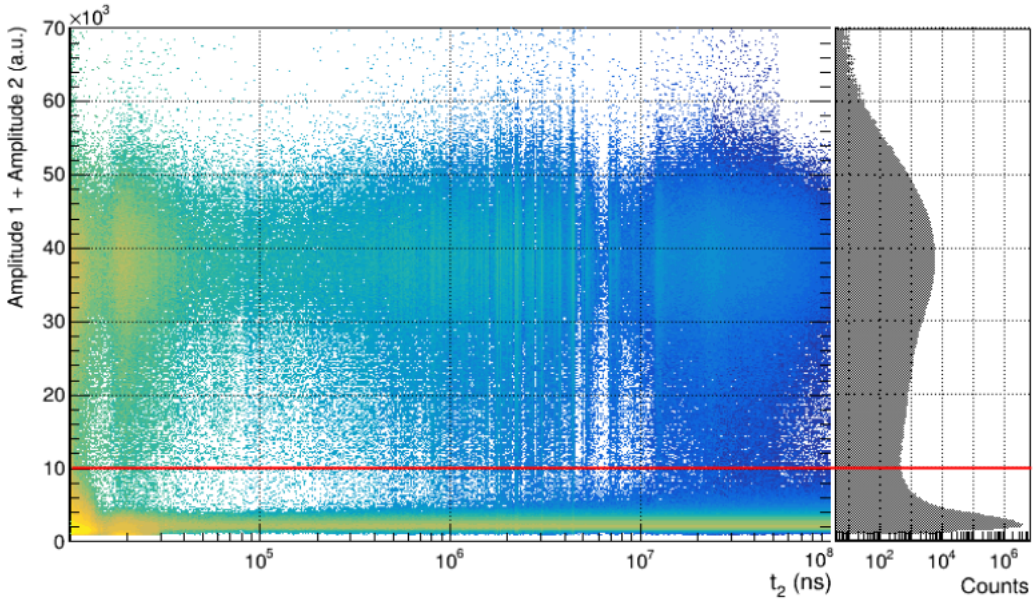

Figure 4.3: Sum of the amplitudes of the coincident signals in the first and second PPAC as a function of the detection time in the second detector (time starts from the PS trigger). The distinction between fission and background events can be observed as well as the two main contributions to the background: a constant one related to α radioactivity and one peaked at small times related to spallation reactions. On the left the amplitude spectrum is projected. The red line represents the threshold set in the analysis.

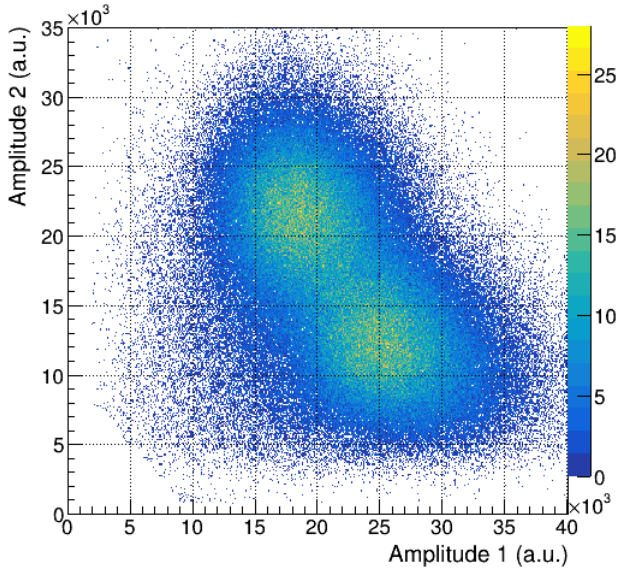

Figure 4.4: Correlation between the amplitudes in the first and in the second PPAC for fission events from the first target. In particular, the higher bump corresponds to the events where the HFF reaches the first PPAC and the LFF the second one, while the lower bump corresponds to the opposite situation.

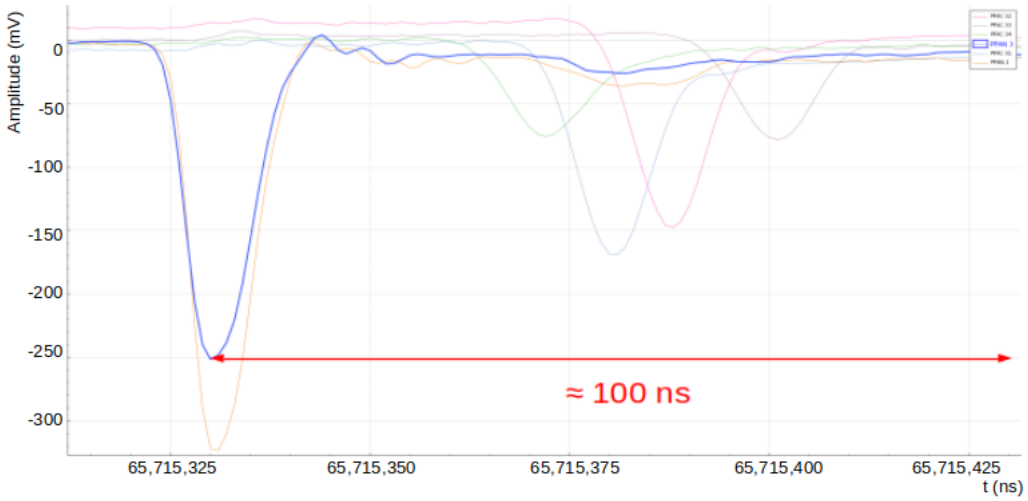

Figure 4.5: Raw signals showing a coincidence between two anodes followed by the four cathode signals in a PPAC within 100 ns.

of their time delays with respect to the anode signal must be equal to the total time length of the delay line (DLT).

Hence, the algorithm implemented proceeds in two steps. First, for each selected anode signal, coincident signals are searched for in the four corresponding cathodes, within a time window of 120 ns. Secondly, all the possible combinations of signals in each cathode are required to satisfy the condition:

$$t_{Ch1} + t_{Ch2} - 2 \cdot t_{An} \sim DLT, \tag{4.1}$$

where t_{Ch1} and t_{Ch2} are the times of the two cathode readouts and t_{An} is the time of the signal in the anode. The tolerance on the equation is of few ns, as shown by the spectra in Figure 4.6. The time difference between the two selected signals in each cathode is saved for the event spatial reconstruction.

In the end, for each fission event two anode and eight cathode signals are saved. If one of the eight cathode signals is missing, for example because of the absorption of the fission fragment in an intermediate dead layer, the whole fission event is discarded. This happened approximately in the 30% of the events previously selected considering only the anodes.

In conclusion, it is interesting to observe the effect of the geometry of the PPACs on the cathode signals. In fact, when a fission fragment crosses a PPAC, a signal is produced simultaneously in the anode and in the first encountered cathode, as described in section 3.3.1. On the other hand, the signal in the other cathode is delayed by the time needed by the fission fragment to travel the gap between the first two electrodes, from a fraction to a few ns. This is the reason

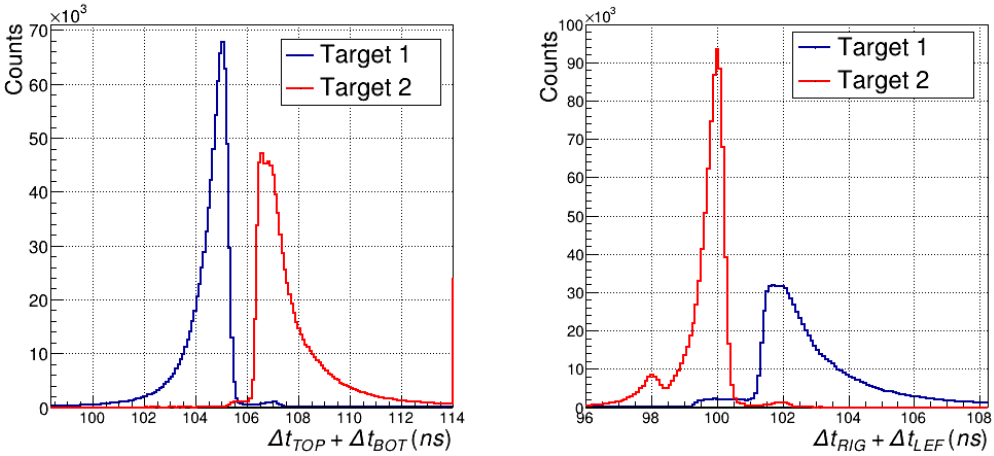

Figure 4.6: Sum of the time delays with respect to the anode of the two selected signals in the Y-stripped cathode (*a*) and in the X-stripped cathode (*b*) of the central PPAC. The signals from the fission events in the first target and in the second target are respectively blue and red. In first approximation the sums are peaked around the total time length of the delay line with a width of few ns. The effect of the PPAC geometry is also observed, see text for details.

why, in the same cathode, the sum of the time delays of its readouts with respect to the anode signal ($t_{Ch1} + t_{Ch2} - 2 \cdot t_{An}$) depends on the target in which the detected fission fragment is produced, as still shown in Figure 4.6. In particular, since the Y-stripped cathode is always placed upstream while the X-stripped one downstream with respect to the neutron beam, in the Y-stripped cathode of the second PPAC the signals of the fission fragments from the second target are delayed with respect to those from the first target (Figure 4.6a). The opposite situation occurs in X-stripped cathode (Figure 4.6b).

In the same figures, the effect of the stochastic energy loss and consequent slowdown of the fission fragments crossing the PPAC is also observed. In fact, the peak of the counts of fission fragments from the first target is strongly smeared passing from the Y cathode (the first encountered) to the X cathode. Conversely, the peak of the signals from the second target is smeared passing from the X to the Y cathode, because of the opposite order in which they are crossed. Moreover, in the X cathode of the second PPAC, the peak of the counts of fission fragments from the second target is the highest one since they do not encounter any obstacle before. Conversely, for example, the fragments from the first target have to cross the sample backing before reaching the Y cathode of the central PPAC.

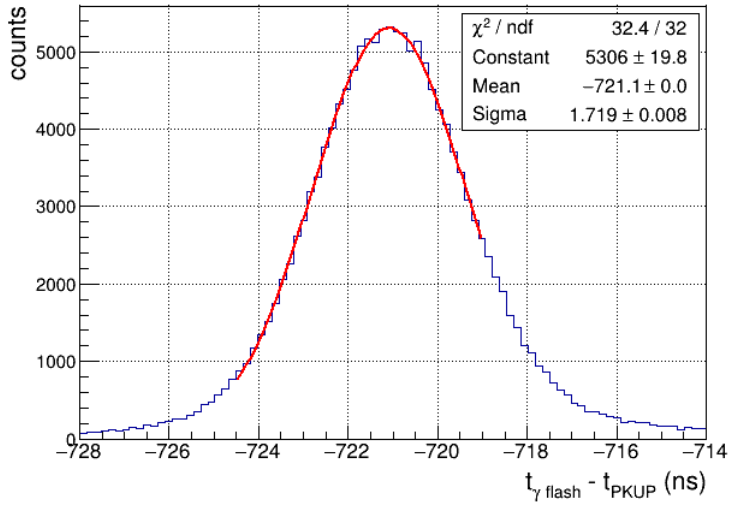

Figure 4.7: Time difference between the γ-flash signal in the central PPAC and the PKUP signal ($t_\gamma^{Meas} - t_{PKUP}$) fitted with a gaussian distribution.

4.2 Time-to-Energy conversion

The calculation of the kinetic energy of the neutrons inducing the fission reactions is a crucial point for the determination of the energy spectrum of the neutron flux. As discussed in details in the section 2.3, the neutron energy is estimated through the time-of-flight technique, using the time difference between the neutron detection in the experimental area (t_s) and the PKUP signal (t_{PKUP}) in the final formula

$$E = mc^2 \left(\frac{1}{\sqrt{1 - \left(\frac{1}{c} \frac{L+\lambda(E)}{t_s - t_{PKUP} + t_0} \right)^2}} - 1 \right). \tag{4.2}$$

However, if some of the factors, such as the neutron mass m or the speed of light c, are well known constants, the other terms involved need a further discussion, carried out in the following.

Starting from the time variables, the PKUP time does not need further explanations, while the neutron detection time t_s is identified with the time of the fission fragment signals in the anode of the central PPAC. Indeed, the time between the neutron arrival, i.e. the fission in the target, and the detection of the fragments in an adjacent detector is smaller than the proton bunch time length (7 ns), thus negligible.

However, since the two signals t_s and t_{PKUP} come from different detectors, a potential non-negligible time offset t_0 due to the difference in the cable lengths has

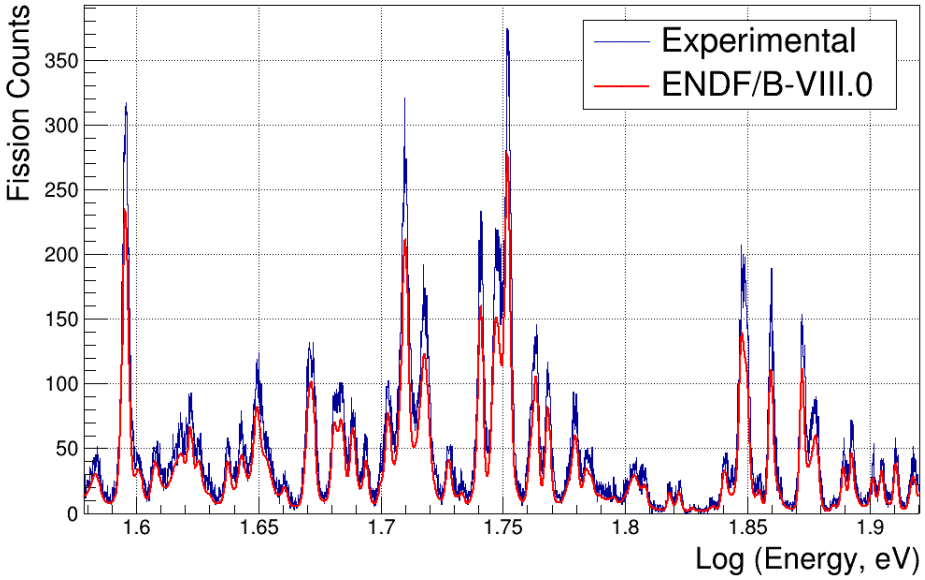

Figure 4.8: Comparison between the detected neutron energy spectrum (blue) and the ^{235}U fission cross section from the ENDF/B-VIII.0 library (red) in the resonance region for an effective total flight path of 183.55 m.

to be considered. This time offset is determined considering a signal whose timing is known *a priori*: it is the case of the γ-flash, expected in EAR1 approximately t_γ^{Th} = 612 ns after the PKUP signal. This time interval corresponds indeed to the flight path between the spallation target and the PPAC divided by the speed of light. In particular, the time offset is determined comparing the measured time difference between the γ-flash and the PKUP signals ($t_\gamma^{Meas} - t_{PKUP}$, shown in Figure 4.7) with the expected t_γ^{Th} according to:

$$t_0 = t_\gamma^{Th} - (t_\gamma^{Meas} - t_{PKUP}) = \frac{L}{c} - (t_\gamma^{Meas} - t_{PKUP}). \tag{4.3}$$

A time offset exceeding 1.3 μs results. The uncertainty related to the t_0 calibration is the width of the distribution in the figure, i.e. few ns, negligible since still lower than the proton bunch time duration.

For what concerns the spatial variables the accurate value of the flight path (comprehensive of the geometric L and of the effective moderation distance λ) is determined comparing the energy spectrum of the detected neutrons and the ^{235}U fission cross section in the resonance energy region, available in literature. The value of the length is tuned with an iterative process in order to achieve the best alignment between the resonances, as shown in Figure 4.8. In this work, the

value set is 183.55 m for neutrons of few tens of eV. The variation of the effective moderation length $\lambda(E)$ with energy modifies accordingly this value for neutrons of different energy.

Actually, since the resolution function for the new target assembly is still not available, in this work λ is neglected and the effective flight path found is assumed constant over the whole neutron energy range. Due to the long distance between the spallation target and the experimental area, the moderation length represents indeed only a second order correction in the analysis in EAR1, corresponding to a maximum of 0.3% for the energy of fast neutrons.

4.3 Fission events spatial reconstruction

The spatial reconstruction of the fission events is a crucial point not only to study the neutron beam profile, but also to study the detector efficiency for the neutron flux determination. In particular, for each selected fission event the eight cathode signals are exploited to determine the position of the two fission fragments as they cross the PPACs, then their trajectory and finally the position on the target where the fission took place. Since this latter is the neutron impact position on the target, the spatial neutron beam profile is also obtained.

4.3.1 Position of the fission fragments in the PPACs

As explained in the section 3.3.2, beyond their simple detection, the design of the employed PPACs allows the spatial localisation of the fission fragments crossing them. In particular, the principle is based on the stripped cathodes and on the double readout of the delay line (one at each end) which each strip is connected to.

With reference to Figure 4.9, suppose a fission fragment crossing the PPAC at a position x. The corresponding cathode readout times at the ends of the delay line are

$$t_{ch1} = t_0 + \frac{1}{v}\left(\frac{L}{2} + x\right) \quad t_{ch2} = t_0 + \frac{1}{v}\left(\frac{L}{2} - x\right) \tag{4.4}$$

where t_0 is the anode signal time, L and v are the length and the signal velocity in the delay line. Subtracting the two equations, the position of the fission fragment can be related to the time difference between the two cathode readouts by:

$$x = v \cdot (t_{ch1} - t_{ch2}) + x_0. \tag{4.5}$$

This procedure is applied to each of the four cathodes involved in each fission event in order to determine the X and Y position of both the fission fragments in the PPACs.

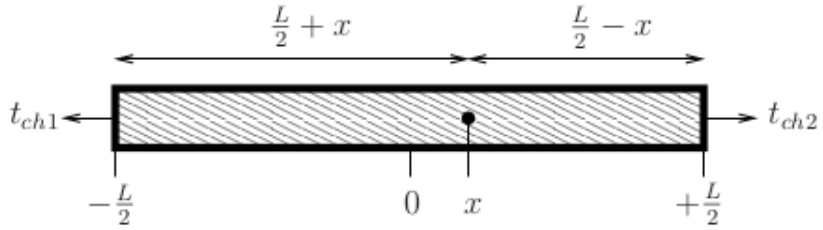

Figure 4.9: Scheme for the cathode delay line read at both the ends.

Since different detectors are involved in the spatial reconstruction of an event, an offset x_0 has to be additionally considered to correct for any potential misalignment of the detectors.

The idea used to set this offset is based on the back-to-back emission of the fission fragments. This implies that the position of the signals from a same fission event in the PPACs surrounding the target should be approximately symmetric with respect to the centroid of the neutron beam, where the highest number of fissions is expected. The cathodes of the central PPAC are assumed as references. Hence, the correlation between the positions of the fission fragments in the adjacent PPACs is found selecting signals in the reference cathode within thin spatial regions and averaging the spatial distribution of the corresponding signals in the homologous cathodes of the other two detectors. Finally, the sought offset is obtained by the intercept of the straight line fitting these correlations, as shown in Figure 4.10. The procedure has to be separately repeated for the X and the Y cathodes and the results are summarized in Table 4.1.

Table 4.1: Offests x_0 used to align the X and the Y cathodes of the different detectors. Values for the central PPAC (PPAC 2) are set by reference.

	X offset (mm)	Y offset (mm)
PPAC 1	-6.64 ± 0.13	0.0 ± 0.2
PPAC 2	-10	0
PPAC 3	-7.3 ± 0.2	-1.37 ± 0.12

4.3.2 Trajectory of the fission fragments

Once the position of the two fission fragments in the PPACs are found, their trajectory can be determined reconstructing the straight line connecting these two points as shown in Figure 4.11. In particular, the trajectory can be described in

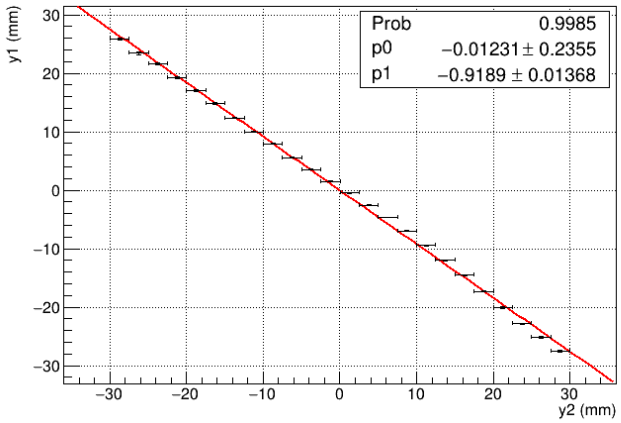

Figure 4.10: Correlation of the Y positions of the signals in the first and central PPACs for fission events in the first target. The offset needed to align the detectors results from the fit intercepts.

terms of the coordinates on the target (X, Y) and of the angle θ between the beam and the fragment emission directions. They result from the following geometric calculations:

$$X = \frac{x_1 \cdot (d+e) + x_2 \cdot (d-e)}{2d} \tag{4.6a}$$

$$Y = \frac{y_1 \cdot (d-e) + y_2 \cdot (d+e)}{2d} \tag{4.6b}$$

$$\cos\theta = \frac{2d}{\sqrt{(x_2 - x_1)^2 + (y_2 - y_1)^2 + 4d^2}} \tag{4.6c}$$

where d and e are the distances target-anode and anode-cathode respectively and x_1, y_1, x_2, y_2 are the coordinates of the fission fragments in the upstream and downstream PPAC with respect to the target. With this procedure, the coordinates of the fission reaction can be evaluated with a spatial resolution of approximately 1 mm, while the simulations show that the uncertainty on $\cos\theta$ amounts at maximum at the 4% for the largest angles [68]. The asymmetry between the formulae for X and Y is still due to the geometry of the PPACs, that causes the x and y coordinates of the fission fragments to be evaluated at different z positions, asymmetric with respect to the target, as shown in Figure 4.11. This effect was considered since produces effects larger than the achievable spatial resolution.

The procedure described is based on the assumption that fission reactions occur at rest in the laboratory frame and the fission fragments are emitted back to back. However, it is the case at low energy only and increasing the neutron energy above about 100 MeV this approximation is no longer valid. In fact, neutrons

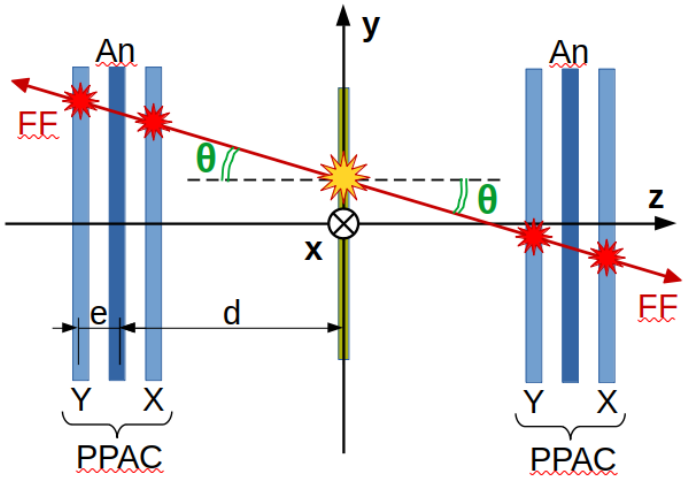

Figure 4.11: Reconstruction of the trajectory of the fission fragments from their positions in correspondence of the PPACs. The different z position where the x and the y coordinates of the fission fragments are measured is also underlined and must be considered in the trajectory reconstruction.

at these energies transfer a non-negligible part of their momentum to the target nucleus, therefore the fission does not occur at rest. In particular, the maximum linear momentum transfer is reached by 1 GeV neutrons and it is estimated at 350 MeV/c [68]. Measurements of the linear momentum transfer for neutrons up to 200 MeV can be found in [76]. Although in the center of mass frame the fission fragments are still emitted back to back at an angle θ_{CM}, in the laboratory frame their emission angles θ_{LAB} are modified by the Lorentz boost, as shown in Figure 4.12. According to the Lorentz transformation, the equation for θ_{LAB} is

$$\tan\theta_{LAB} = \frac{\sin\theta_{CM}}{\gamma(\cos\theta_{CM} + \beta/\beta')}, \tag{4.7}$$

where $\beta = v_{CM}/c$ and the Lorentz factor γ are referred to the velocity v_{CM} of the center of mass of the system with respect to the laboratory frame, while $\beta' = v'/c$ is referred to the velocity v' of the fission fragments in the center of mass frame. Since the actual position where the fission reaction takes place is unknown, the previously described procedure cannot reproduce correctly the trajectory of the fission fragments, neither in terms of the emission angle nor in terms of the position of the fission reaction. In fact, the geometrical calculations referred to Figure 4.12 show that the tangent of the reconstructed angle θ_M is a mean of the tangents of the real emission angles of the fission fragments in the laboratory frame ($\theta_{LAB,1}$ and $\theta_{LAB,2}$)

$$\tan\theta_M = 0.5 \cdot (\tan\theta_{LAB,1} + \tan\theta_{LAB,2}), \tag{4.8}$$

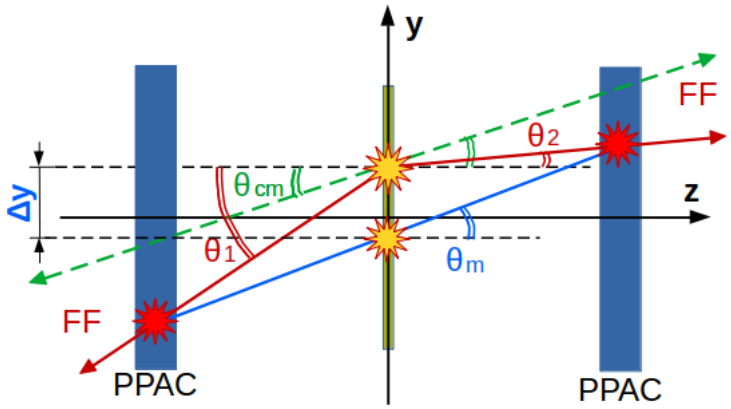

Figure 4.12: Effect of the Lorentz boost on the trajectory of the fission fragments in the laboratory frame (red) at high neutron energy compared to the back-to-back emission in the center of mass frame (dashed green). In blue the trajectories and the angle reconstructed assuming the system at rest.

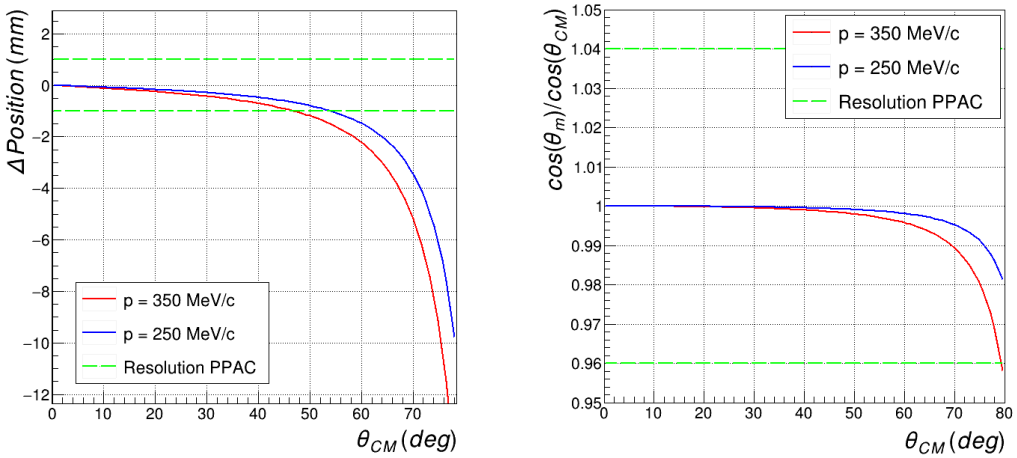

(a) **(b)**

Figure 4.13: Estimates for the deviation between the reconstructed and the real position of the fission reactions (*a*) and for the ratio between the reconstructed and the real fission fragment emission angle (*b*) as a function of the real emission angle in the center of mass frame. The red and the blue curves correspond to a linear momentum transfer of 350 MeV/c (correspondent to 1 GeV neutrons) and 250 MeV/c (100 MeV neutrons), respectively. For the angles accepted by the detector (approximately $< 60°$) the deviations are lower or comparable with the experimental resolution (dashed green lines).

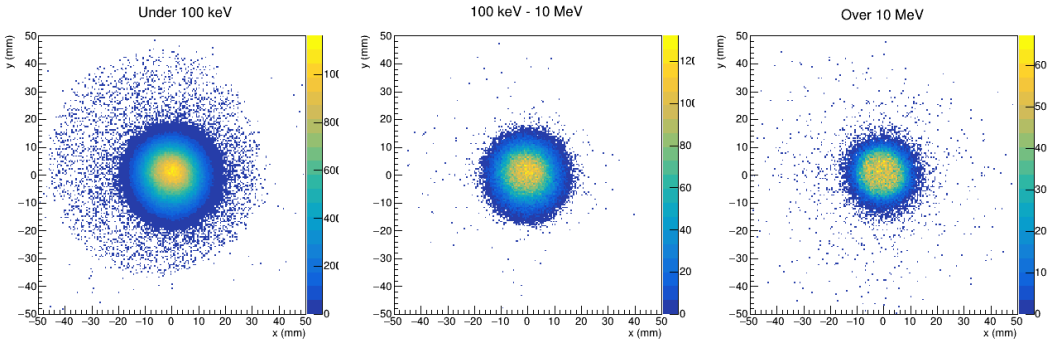

Figure 4.14: Neutron beam spatial profile in EAR1 for neutrons of different energy: under 100 keV (left), between 100 keV and 10 MeV (center) and over 10 MeV (right).

while the reconstructed fission coordinates differ from the real ones by

$$\Delta Position = 0.5 \cdot d \cdot (\tan\theta_{LAB,1} - \tan\theta_{LAB,2}). \tag{4.9}$$

Nevertheless, Monte Carlo simulations have indicated that for the PPAC detectors the described procedure is a good approximation that can be applied even at high energy [68]. In fact, as shown in Figure 4.13, for the emission angles accepted by the detector, the reconstructed $\cos\theta_M$ and fission position reproduce θ_{CM} and the real fission position with deviations lower or comparable with the experimental resolutions.

4.3.3 Spatial neutron beam profile

The reconstruction of the trajectory of the fission fragments allows the determination of the position of the fission reactions on the target. Since this is the neutron impact position, the superimposition of the position of all the fission events in both the targets results in the spatial distribution of the neutrons in the beam, the so-called beam profile.

The beam profile can be even studied varying the neutron energy, as shown in Figure 4.14. In particular, low-energy neutrons are much more diffused, therefore they can trigger fissions in the whole uranium target, whose shape is indeed reproduced by the halo in the the first image of Figure 4.14. Although rarer, fission events are shown to be induced by high energy background neutrons, too. However, the majority of fission events are contained in the circular beam spot, that is clearly visible in all the three figures.

To provide quantitative information about the beam profile, the beam spot is fitted with a two-dimensional generalized gaussian distribution of equation:

$$z(x,y\,|\,\mu_x,\mu_y,\alpha_x,\alpha_y,\beta_x,\beta_y) = A \cdot \exp -\left(\frac{|x-\mu_x|}{\alpha_x}\right)^{\beta_x} \cdot \exp -\left(\frac{|y-\mu_y|}{\alpha_y}\right)^{\beta_y} \tag{4.10}$$

to reproduce the flat top especially at high energy. The normalization factor A and μ, α and β are the adjustable parameters of the fit. The FWHM in both the dimensions is computed as:

$$FWHM = 2\alpha \cdot \sqrt[\beta]{\ln 2}. \tag{4.11}$$

The results are reported in Table 4.2. It can be observed that the dimension of the beam is slightly reduced for high energy neutrons due to their smaller emission region in the spallation target [17].

The beam spot for high energy neutrons (above 100 keV) is compared to the results obtained by the Timepix detector, placed approximately in the same position of the PPAC Monitor during the alignment phase, in Figure 4.15. Table 4.2 also reports the values of the FWHM obtained from the fitting procedure in the two detectors; the results are in agreement within 2%.

Table 4.2: FWHM of the beam profile from the fitting procedure. In the case of the PPAC, the uncertainties from the fit are negligible with respect to the detector spatial resolution (± 1 mm).

	FWHM X (mm)	FWHM Y (mm)
PPAC (Full Energy Range)	15.76 ± 0.07	14.95 ± 0.05
PPAC (E > 100 keV)	15.29 ± 0.05	14.32 ± 0.07
Timepix (E > 100 keV)	15.07 ± 0.03	14.62 ± 0.02

4.4 Efficiency

As already discussed in the section 3.3, the single PPACs have an efficiency close to one in detecting the fission fragments, but the efficiency of the overall PPAC Monitor is strongly limited for the fission events characterized by large emission angles. Indeed, when the fission fragments are emitted at large angles with respect to the neutron beam, they have to cross a larger amount of material and, due to their high stopping power, can be stopped in the detector dead layers or even inside the target itself.

For this reason, the detector efficiency as a function of the fission fragment emission angle θ is expected to have a *plateau* close to one at small angles and then fall rapidly to zero increasing the angle over approximately 60°. This behaviour is indeed well reproduced by the $\cos\theta$ distribution of the selected fission events,

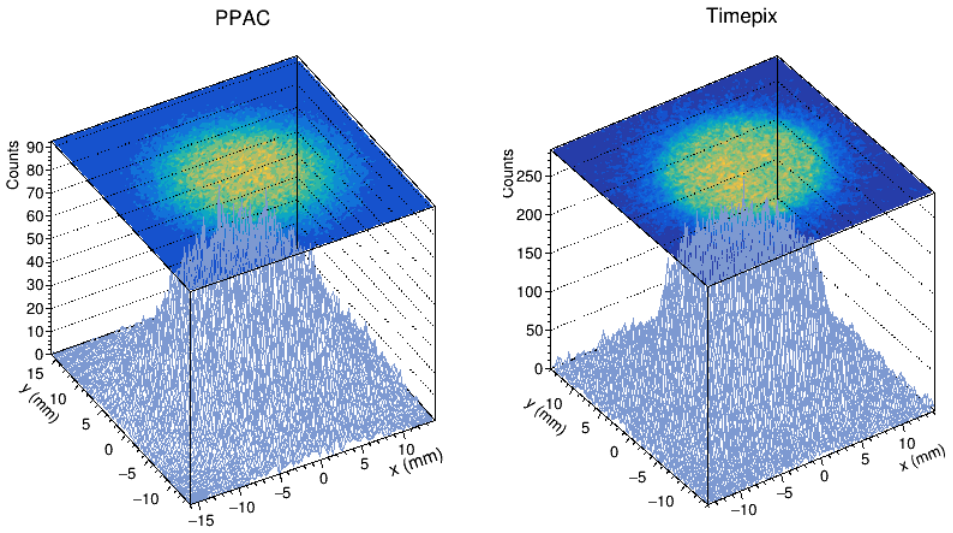

Figure 4.15: Neutron beam profile obtained from the PPAC Monitor (left) and the Timepix Quad detector (right) for neutrons over 100 keV.

well described by a generalized sigmoid function of equation:

$$y(\cos\theta \,|\, p_0, p_1, p_2, p_3) = \frac{p_0}{\left(1 + e^{\,p_1 \cdot (p_2 - \cos\theta)}\right)^{p_3}}, \tag{4.12}$$

where the normalization factor p_0, p_1, p_2 and p_3 are adjustable parameters set by a fitting procedure. The fitted distribution for the fission events in the first target is shown in Figure 4.16a. The value of the detection efficiency is represented by the integral over $\cos\theta$ of the distribution once the *plateau* has been normalized to one.

However, this is true for neutron energies lower than 100 keV only, where the induced fission reactions release the fragments isotropically in space. In fact, increasing the neutron energy, the anisotropy in the fission fragment angular distribution (FFAD) becomes a significant correction to the value of the detection efficiency. At neutron energies over 100 keV the $\cos\theta$ distribution of the selected fission events can be indeed reproduced by a distribution of equation:

$$y(\cos\theta \,|\, p_2, p_3, p_4) = \frac{f(\cos\theta)}{\left(1 + e^{\,p_2 \cdot (p_3 - \cos\theta)}\right)^{p_4}}, \tag{4.13}$$

that entangles both the the detector efficiency and the fission fragment angular distribution $f(\cos\theta)$, as shown in Figure 4.16b. The FFAD reproduces the small-angle behaviour of the distribution (4.13), instead of the previously mentioned *plateau* related to an isotropic FFAD only, and it can be approximately parameterized as the linear combination of the two first even Legendre polynomials [17]

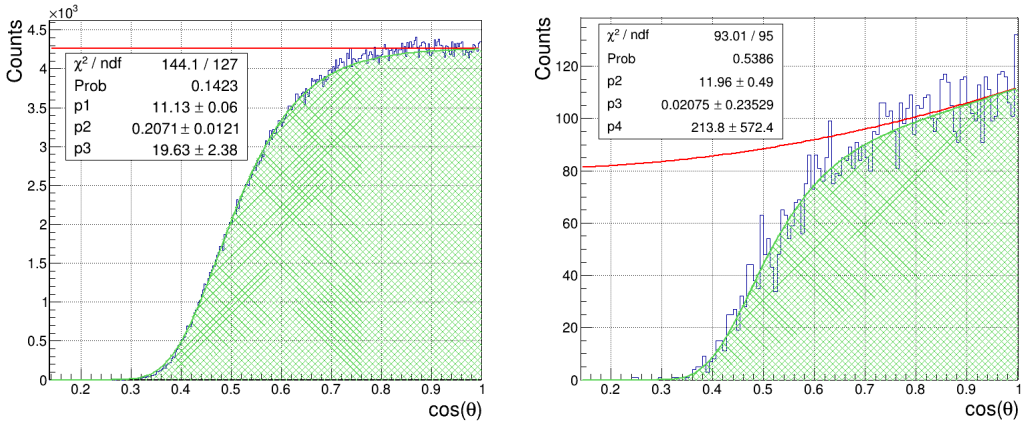

Figure 4.16: Distributions of the cosine of the fission fragment emission angle for fission events in the first target induced by neutrons of energy lower than 100 keV (*a*) and in the range 3.16-10 MeV (*b*). In the first case, the isotropic fission fragment angular distribution (FFAD) results in a *plateau* at small angles, while in the second case, corresponding to the energy region of maximum anisotropy in the FFAD, the small-angle behaviour reproduces the function (4.14). The green curves are the fit with the functions (4.12) and (4.13), respectively. Their integrals, highlighted in the figures, are related to the detection efficiency.

as:

$$f(\cos\theta) \sim a_0 + b_0 P_2(\cos\theta) = p_0 + p_1 \cos^2\theta. \tag{4.14}$$

The terms p_0, p_1, p_2, p_3 and p_4 are adjustable parameters set by a fitting procedure. The detection efficiency is still calculated as the integral of the distribution (4.13) once the FFAD (4.14) has been normalized to one.

The estimated values of the efficiency in the full neutron energy range are shown in Figure 4.17 and range approximately from 0.48 to 0.53 for the first target and from 0.55 to 0.62 for the second one. The maximum values are observed exactly in correspondence of the energy region (approximately between 6 MeV and 20 MeV) where the anisotropy in the fission fragments angular distribution is maximum [76].

At neutron energies over 100 MeV a decrease in the efficiency is expected due to the Lorentz boost [17]. In fact, as already discussed and shown in Figure 4.12, it increases the emission angle (in the laboratory frame) of the backward fission fragments, making those already emitted at large angles more likely to be stopped.

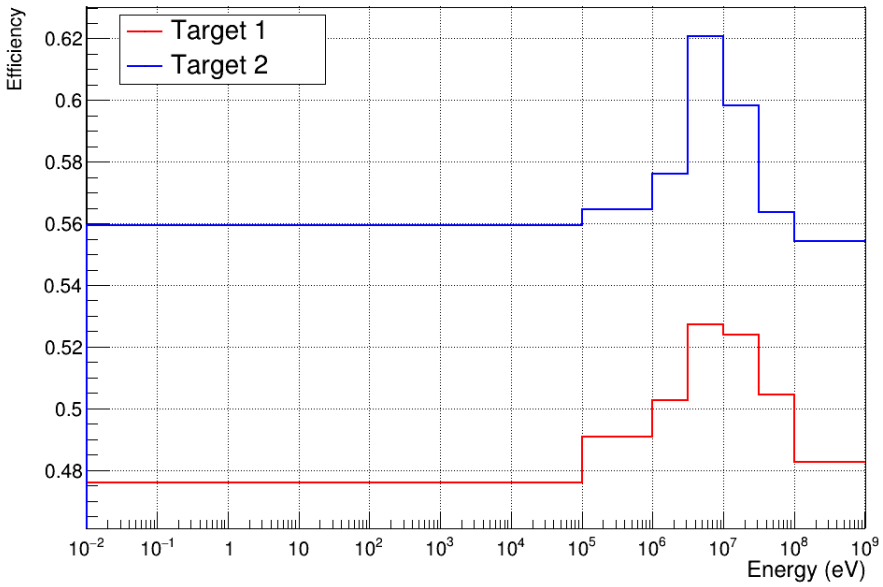

Figure 4.17: Estimated detector efficiency as a function of the neutron energy for the first (red) and the second (blue) target.

4.5 Neutron flux

Finally, as the last step of the analysis, the isolethargic neutron flux as a function of the neutron energy E_n is calculated according to the previously discussed formula (3.9):

$$\frac{d\Phi(E_n)}{d\ln E_n} = E_n \frac{d\Phi(E_n)}{dE_n} = \left(\frac{C(E_n) - B(E_n)}{\epsilon(E_n) \cdot n \cdot \sigma(E_n)} \right) \cdot bpd \cdot \log e,$$

where all the terms are known or provided by the previous analysis. In particular, $\epsilon(E_n)$ is the efficiency as a function of the neutron energy estimated in the previous section, n is the areal density of the samples estimated on average at 7.17 $\times$ 10^{-7} at/barn and $\sigma(E_n)$ is the ^{235}U(n,f) cross section corrected for the sample isotopic composition. $C(E_n) - B(E_n)$ is the number of the selected fission events obtained subtracting background events from the total counts in each energy bin. The counts are normalized for a single bunch, thus divided by the total number of protons delivered during the measurement time (approximately 2.24 $\times$ 10^{18} protons) and multiplied by the nominal bunch size (7 $\times$ 10^{12} ppp).

Firstly, the neutron flux is calculated separately from the two targets, as shown in Figure 4.18. The consistency of the two results is proved by the constant value of their ratio over the full neutron energy range, shown in the bottom panel of Figure 4.18. On the other hand, the difference in the absolute value of the flux is

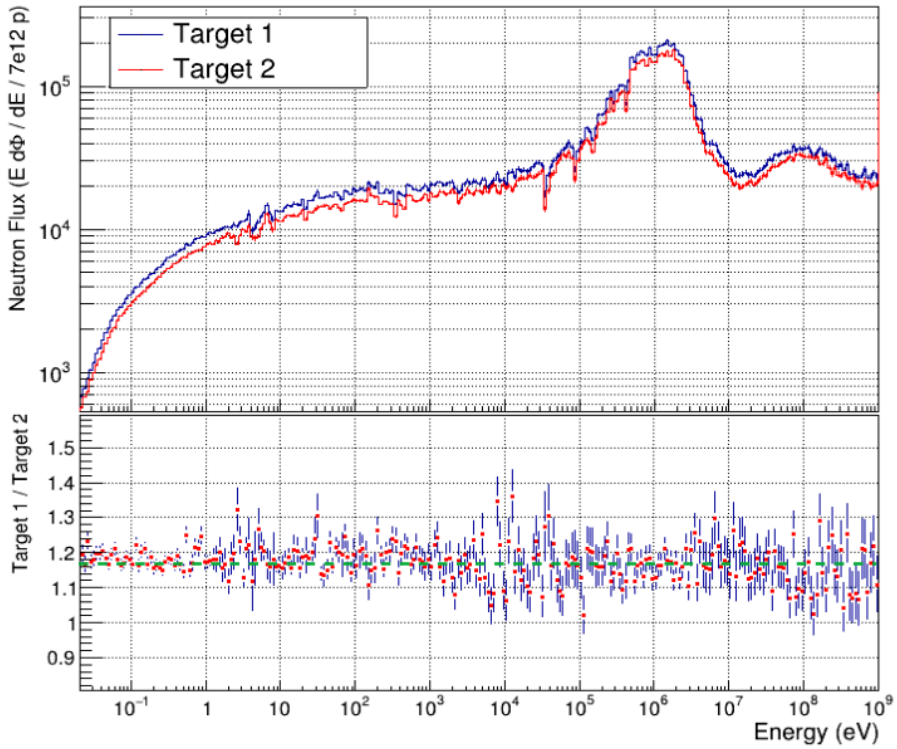

Figure 4.18: Isolethargic neutron flux in EAR1 at 25 bins per decade separately extracted from the two uranium samples. The constant ratio between the two fluxes, shown in the bottom panel, proves the consistency of the results and its value, centered around 1.17 (dashed line), is related to the different areal densities of the samples.

related to the different actual thickness of the samples. In fact, since the second target is not well characterized, the accurate value of its areal density is adjusted in this phase to provide the same absolute value for the flux provided by the first well characterized sample.

Then, the neutron flux is extracted considering both the targets (Figure 4.19) using the sum of their areal densities and adding their counts corrected for the respective efficiencies. At 50 bins per decade the achieved statistical uncertainty, also shown in Figure 4.19 (bottom panel), ranges approximately from 1% at thermal energy to 5% at high energy. Its behaviour is related to the counting rate of fission events, maximum at thermal energies where the ^{235}U(n,f) cross section is huge and minimum at high energy where the probability of the reaction is lower. For what concerns the systematic uncertainty due to the efficiency evaluation and to the accuracy with which the cross section and the areal density are known, it is overall estimated at 2%.

In general, the estimated flux qualitatively reproduces the expected shape: the

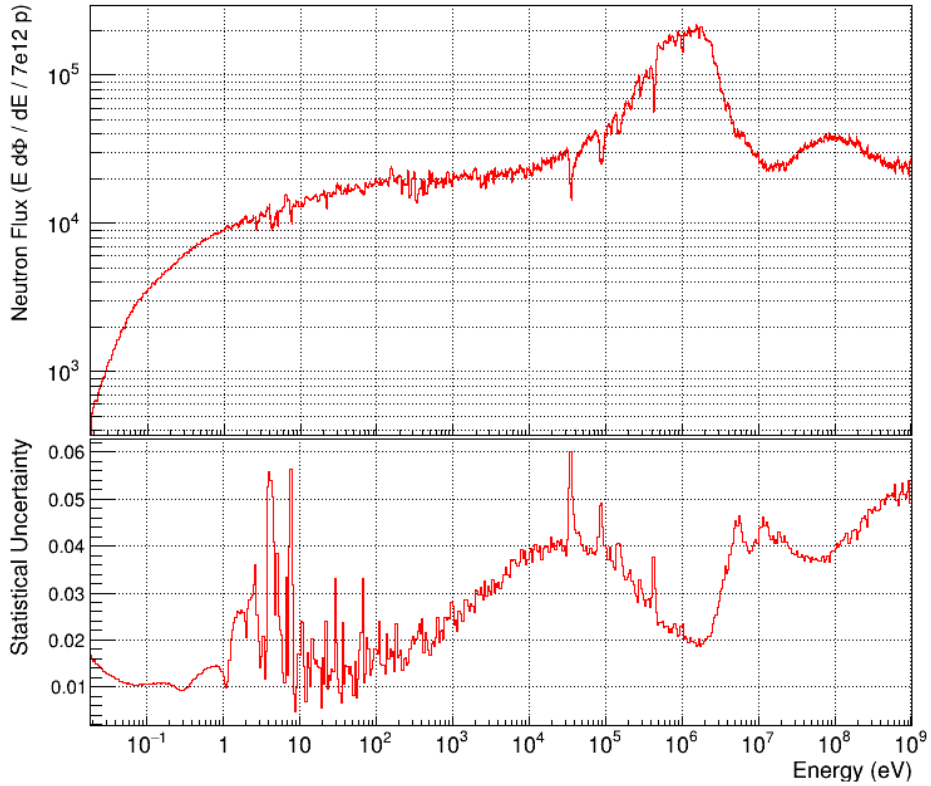

Figure 4.19: Measured isolethargic neutron flux in EAR1 at 50 bins per decade. Both the targets are considered. In the bottom panel the statistical relative uncertainty is plotted.

two peaks corresponding to the equilibrium and pre-equilibrium nuclear evaporation are observed as well as the nearly flat isolethargic region down to thermal energy where the moderator effect is involved. The dips in correspondence of the absorption resonances of aluminum, present along the beam, are also reproduced between 10 keV and 1 MeV. Conversely, the jagged behaviour shown between 1 eV and 10 keV is due to the resonances in the ^{235}U(n,f) conversion reaction cross section, that is indeed not a standard in this energy region.

The neutron flux is also separately achieved for the high-intensity dedicated proton bunches and for the low-intensity parasitic ones, as shown in Figure 4.20. They are both normalized to the dedicated bunch size in order to allow for their comparison. The ratio between the two extracted fluxes is shown in the bottom panel of Figure 4.20. The consistency between the results, within the experimental uncertainty, proves that pile-up does not occur, hence dead-time corrections are not needed. In fact, since the pile-up depends on the intensity of neutrons, the

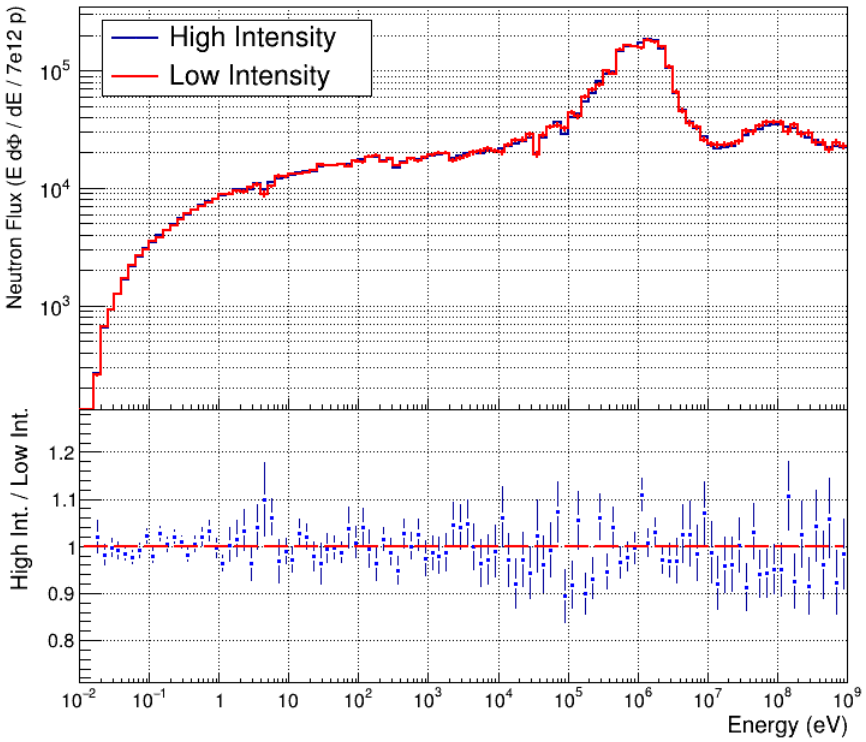

Figure 4.20: Comparison between the measured isolethargic neutron flux in EAR1 at 10 bin per decade from the high-intensity dedicated proton bunches (blue) and from the low-intensity parasitic ones (red). Both are normalized to the dedicated bunch nominal size (7 $\times 10^{12}$ ppp) to allow for comparison. Their consistency over the full neutron energy range proves that no pile-up occurs.

related dead-time correction should be different taking into account dedicated and parasitic bunches: higher for the first and smaller for the second ones. Therefore, an observable would be the flux extracted separately in the two cases, which, in case of pile-up events, would be smaller in the case of the high intensity bunches than in the case of the low intensity ones.

In the end, the measured neutron flux is compared to the preliminary results of SiMon and to the Monte Carlo simulations in Figure 4.21. The comparison with SiMon shows the agreement on the shape of the neutron flux in the energy range between the thermal energy region and about 1 MeV with a presence of a scale factor between 10% and 20%, except for the energy region more seriously affected by the ^{235}U(n,f) resonances. The comparison with the Monte Carlo simulations also shows the agreement on the shape of the neutron flux between about 1 eV and 10 MeV (with an exception at few MeV) with a scale factor close to one, on

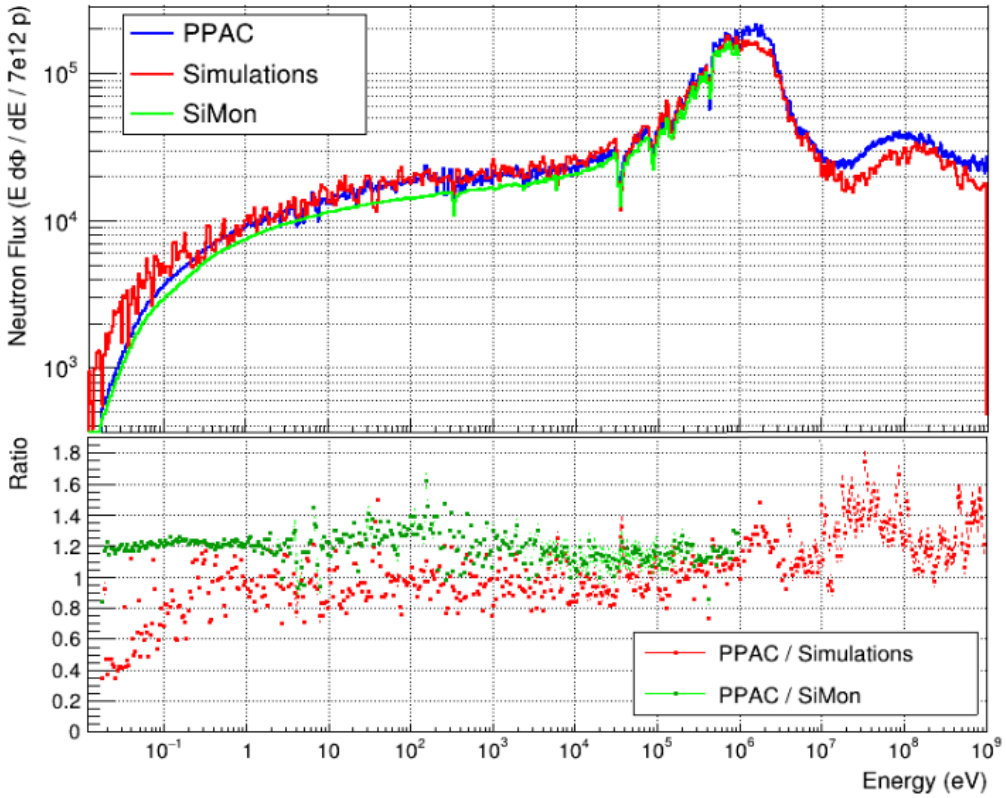

Figure 4.21: Comparison between the results of this work (blue), the results from SiMon (green) and the Monte Carlo simulations (red) for the isolethargic neutron flux in EAR1 at 50 bins per decade. The bottom panel displays the ratios PPAC/SiMon (green) and PPAC/Simulations (red).

average. In particular, the energy region between 0.1 MeV and 1 MeV, where both the ^{235}U(n,f) and the ^{6}Li(n,α) (used by SiMon) cross sections are standard, presents the best agreement between all the three fluxes, within about 10%. In this phase, such constant scale factors between the different fluxes are expected due to systematic effects related, for instance, to the knowledge of the areal density of the targets and of the absolute value of the detector efficiency, but they do not alter significantly the shape of the flux as a function of the neutron energy. However, significant discrepancies, up to 60%, are observed between the results from PPAC and the simulations for energies below 1 eV and over 10 MeV, where neither the shape nor the absolute value of the flux agree. At thermal energy, the consistency between the two experimentally measured fluxes (in terms of the shape) may hint problems in the simulations, due to a non accurate value for the boron concentration in the moderator. At high energy the reasons for such

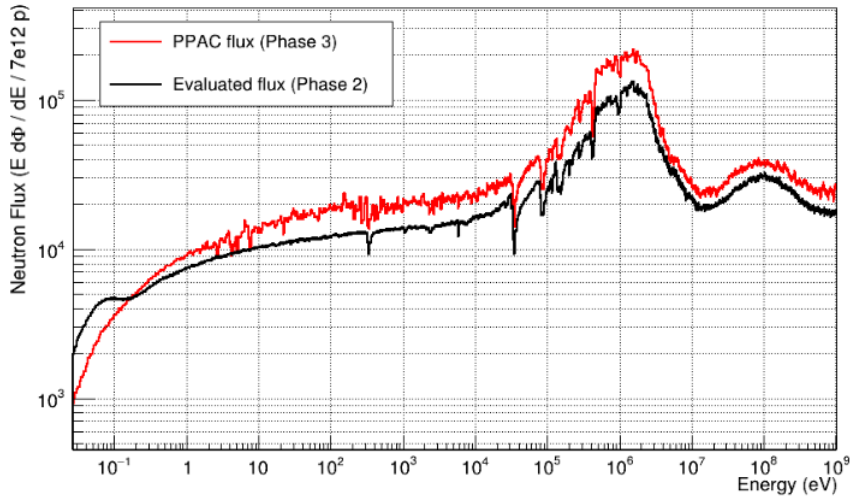

Figure 4.22: Comparison between the results of this work (red) and the evaluated neutron flux in the previous commissioning with the previous target (black).

discrepancies are still not clear.

Finally, the extracted flux is compared to the neutron flux evaluated in the previous commissioning with the previous spallation target [62] in Figure 4.22. With exception for the thermal energy region, the shape of the flux is roughly maintained and an overall increase in its absolute value, up to 80%, is observed over the full neutron energy range.

4.6 First results from EAR2

This last section is aimed at presenting the very first results obtained from the analysis of data from the PPAC Monitor in EAR2, considering the ^{235}U sample only. The different steps of the analysis are exactly those described for EAR1 in the previous sections: the fission events are reconstructed and selected looking for the coincident signals in the anodes and then in the cathodes, the energy of the neutrons inducing the fissions is calculated from the time of the signals and setting the accurate neutron flight path, the trajectory of the fission fragments is determined to provide the spatial beam profile and the detector efficiency, the neutron flux is finally extracted. In particular, the accurate neutron flight path from the spallation target to the detector is found to be 19.66 m and the average detection efficiencies are estimated at 50% for the fission events in the ^{235}U sample and at 63% for those in the ^{238}U one, thinner.

The only difference in analysis regards the calibration of the time offset t_0 used

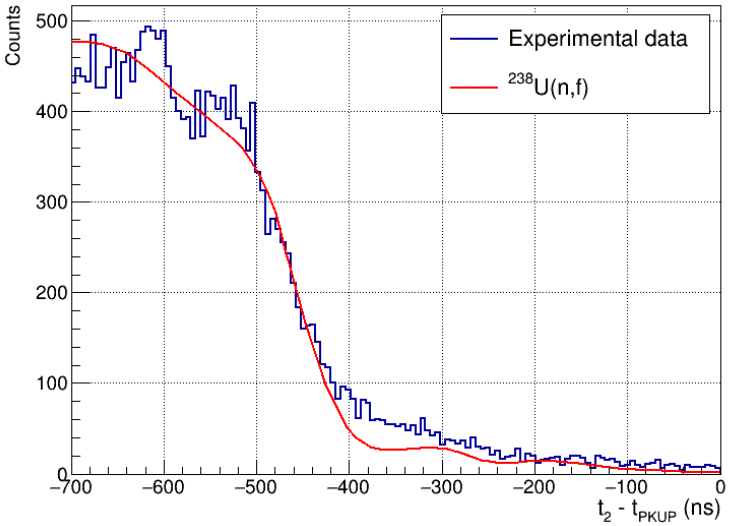

Figure 4.23: Comparison between the spectrum of the detected fission events from the ^{238}U sample and the ^{238}U(n,f) cross section in the threshold energy region as functions of the neutron time of flight, i.e. the difference between the fission detection and the PKUP signal. The time offset t_0 is set at 1.635 μs.

in the time-to-energy conversion (see section 4.2). In EAR1 the γ-flash signal was exploited to determine t_0, but this is not possible in EAR2 where the γ-flash produces an oscillation in the signal baseline of the PPAC Monitor rather than a proper signal. Hence, the fission threshold of ^{238}U, around 1 MeV, is used. Since an exact value for this threshold is not available, t_0 is determined as the time offset providing the best alignment between the spectrum of the detected fission events and the ^{238}U(n,f) cross section in the threshold region as a function of the neutron time of flight, as shown in Figure 4.23. In the following, the notable results of the analysis are presented.

4.6.1 Spatial neutron beam profile

The spatial neutron beam profile in EAR2 for different neutron energy ranges is shown in Figure 4.24. Similarly to EAR1, diffused neutrons, especially at low energy, can induce fissions in the whole uranium target (whose shape is indeed well reproduced in the first image of Figure 4.24), but the majority of the events is concentrated in the beam spot, whose dimensions slightly reduce increasing the neutron energy. However, if the beam spot is circular at low neutron energy, increasing the energy it gets an ellipsoidal elongated shape along the direction of the proton beam incident on the spallation target. This effect can be explained recalling that the high energy neutrons produced in spallation reactions are prefer-

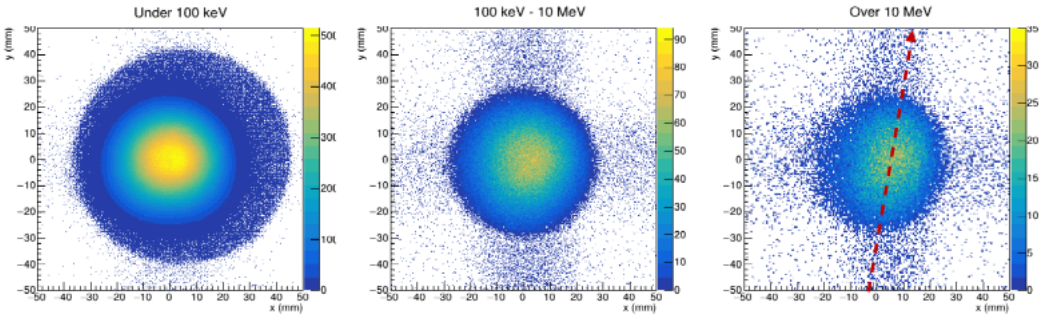

Figure 4.24: Neutron beam spatial profile in EAR2 for neutrons of different energy: under 100 keV (left), between 100 keV and 10 MeV (center) and over 10 MeV (right). In the latter case the direction of the proton beam incident on the spallation target is also shown.

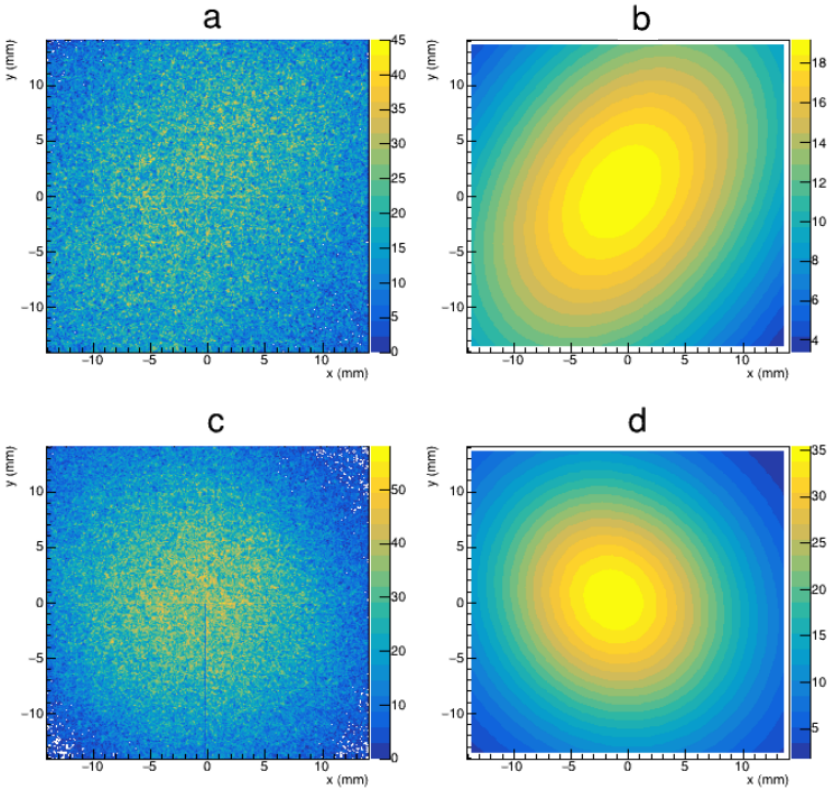

Figure 4.25: Neutron beam spot obtained from the downstream (*a*) and the upstream (*c*) Timepix detectors with respect to the neutron beam for neutrons over 10 MeV. The figures (*b*) and (*d*) represent the fitted two-dimensional gaussian distributions. The opposite rotation angle with respect to the cartesian axis is due to the opposite orientation of the detectors with respect to the beam.

Table 4.3: FWHM of the beam profile in EAR2 from the fitting procedures. In the case of the PPAC, the uncertainties from the fit are negligible with respect to the detector spatial resolution (± 1 mm).

	FWHM X (mm)	FWHM Y (mm)
PPAC (Full Energy Range)	28.775 ± 0.008	26.704 ± 0.007
PPAC (E > 10 MeV)	18.066 ± 0.007	20.964 ± 0.006
Timepix upstream (E > 10 MeV)	14.18 ± 0.02	14.94 ± 0.02
Timepix downstream (E > 10 MeV)	20.45 ± 0.07	23.9 ± 0.1

entially emitted in the forward direction with respect to the projectile. Moreover, the effect increases moving away from the collimator, as confirmed by the high energy beam profiles obtained from the two Timepix detectors placed at different heights in the experimental area, shown in Figure 4.25.

Finally, in order to provide quantitative results, the beam spot for the full neutron energy range is fitted with a two-dimensional generalized gaussian distribution of equation (4.10). The beam spot at high energy (over 10 MeV) is also fitted, but with an ordinary two-dimensional gaussian distribution to account for the rotated beam profile. Because of the different position of the Timepix detectors with respect to the PPAC Monitor and the significant divergence of the neutron beam, differently from EAR1 a direct comparison between the beam profiles at high energy obtained from the two detectors cannot be performed. However, since the PPAC Monitor is placed between the two Timepix Quads, the FWHM estimated with the former consistently lies in between the FWHM estimated with the two latter. The FWHM obtained from the fits are reported in Table 4.3.

4.6.2 Neutron flux

Differently from EAR1, the fission counts from the ^{235}U sample are largely affected by pile-up at high neutron energy in EAR2. This is shown by the comparison between the neutron flux separately extracted from the low-intensity and the high-intensity bunches, shown in Figure 4.26. In fact, if the results are consistent up to about 100 keV, at higher energy the flux estimated from the high-intensity bunches is largely reduced with respect to the other.

Dead-time corrections would be needed to correct for the pile-up at high neutron energy. However, in order to extract a very preliminary flux for EAR2, the effect is minimized in first approximation by considering only the events from the parasitic low-intensity bunches at energy over 100 keV, since less affected by pile-up. The neutron flux calculated in this way is reported in the top panel of

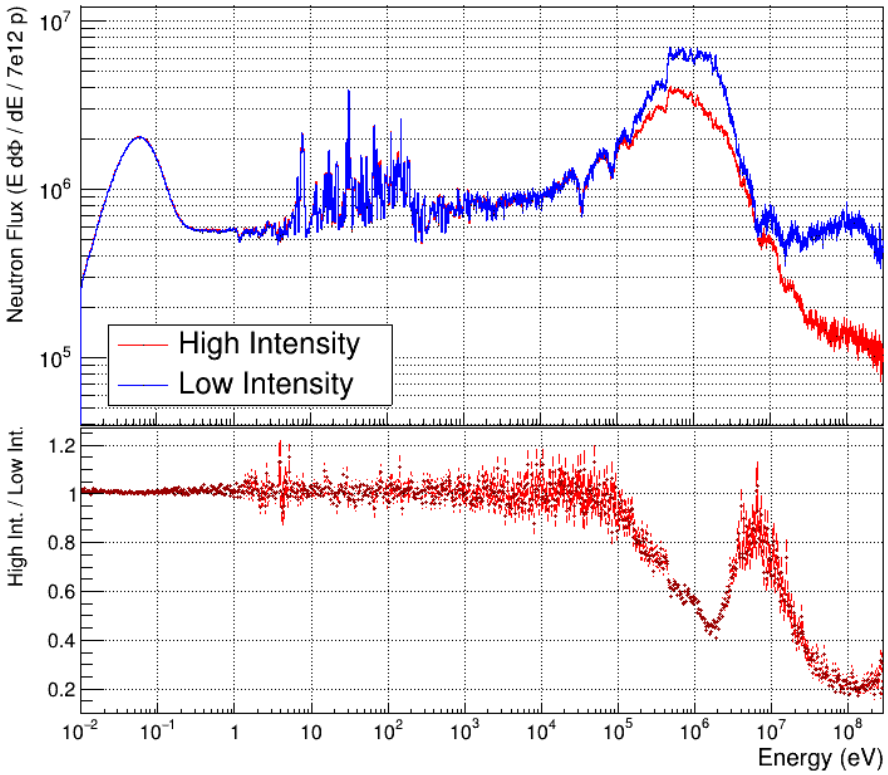

Figure 4.26: Comparison between the measured isolethargic neutron flux in EAR2 at 100 bin per decade from the high-intensity dedicated proton bunches (red) and from the low-intensity parasitic ones (blue). Both are normalized to the dedicated bunch nominal size (7×10^{12} ppp) to allow for comparison. Their discrepancy in the high energy region reveals that pile-up occurred.

Figure 4.27 at 100 bins per decade. The bottom panel shows its relative statistical uncertainty, ranging from less than 0.2% at thermal energy to a maximum of 10% over 100 MeV. As expected, beside the equilibrium and pre-equilibrium neutron evaporation peaks, a peak at thermal energy is also reproduced due to the employment of demineralized water as moderator for EAR2. Moreover, because of the position of EAR2 with respect to the spallation target, the kinetic energy of neutrons is limited at few hundreds MeV, but the value of the flux is nearly two orders of magnitude larger than in EAR1. In the energy region between 1 eV and 10 keV the resonances of the ^{235}U(n,f) cross section are reproduced, as in EAR1.

Finally, the preliminary neutron flux is compared to the preliminary results of SiMon and to the Monte Carlo simulations in Figure 4.28. With exception for the ^{235}U(n,f) resonance region, the comparison shows the agreement on the

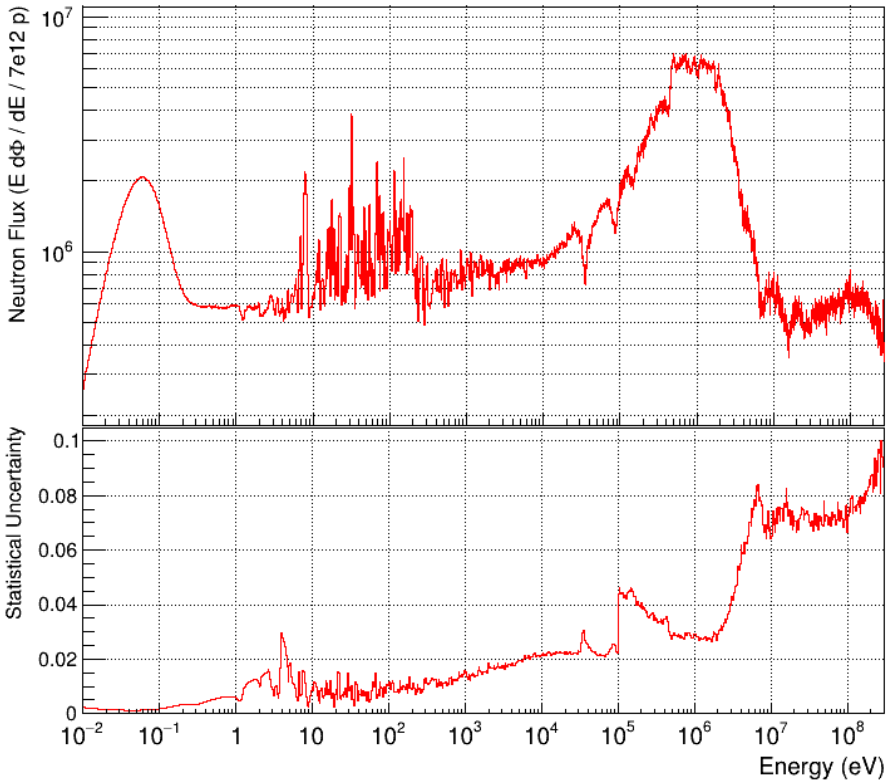

Figure 4.27: Preliminary isolethargic neutron flux in EAR2 at 100 bins per decade. Only the events from the low-intensity bunches are considered at energy over 100 keV to reduce the effect of pile-up. In the bottom panel the statistical relative uncertainty is plotted.

shape of the three neutron flux in the energy range between some fractions of eV and about 100 keV (1 MeV for the simulations) with a presence of a scale factor between 10% and 20%. Similarly to EAR1, at thermal energy the Monte Carlo simulations slightly overestimate the measured flux, while the consistency with SiMon is maintained. At high energy the significant discrepancies observed are probably due to the pile-up effects, that still need to be suitably corrected in a further analysis.

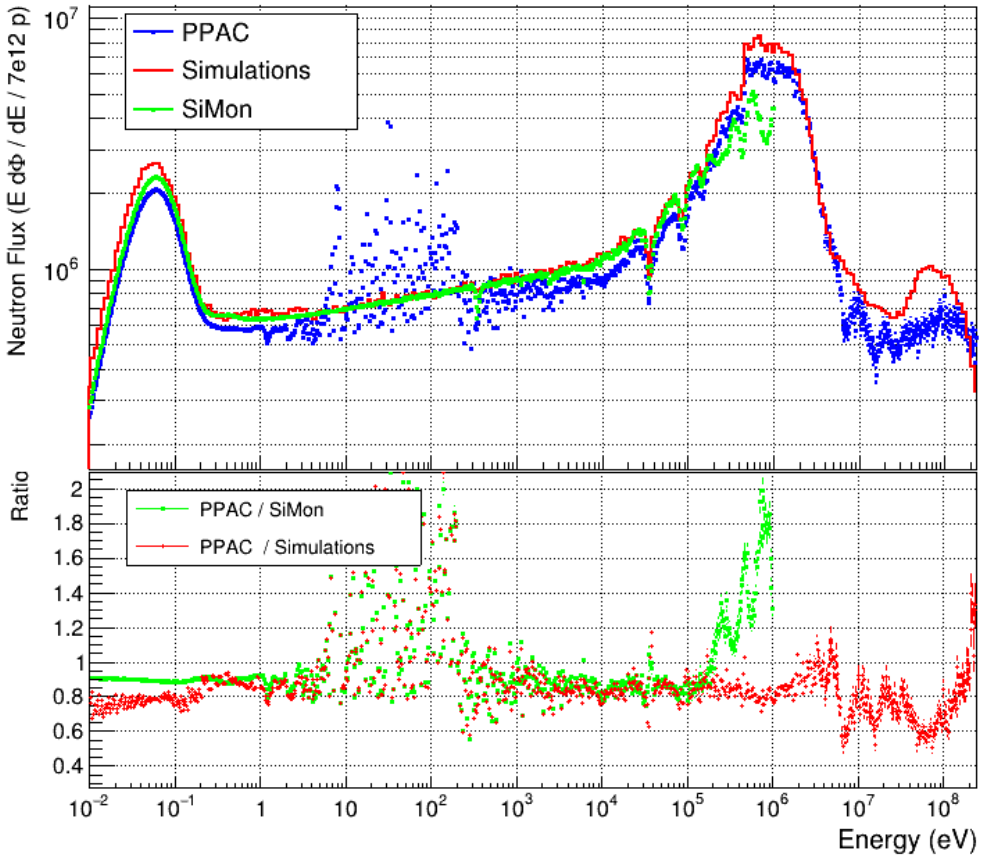

Figure 4.28: Comparison between the preliminary results of this work (blue), the results from SiMon (green) and the Monte Carlo simulations (red) for the isolethargic neutron flux in EAR2 at 100 bins per decade. The bottom panel displays the ratios PPAC/SiMon (green) and PPAC/Simulations (red).

Summary and Conclusion

The applications of neutron-induced reactions have a great impact on society and environment. The electricity generation from nuclear fission has been the leader among the low-carbon energy sources since its introduction and avoided the emission of up to a 50% extra CO_2 in some western countries in the last fifty years. Similarly, nuclear power can significantly contribute, if not even necessarily, to combine in the future the rapid increase of the electricity demand with the fight against the climate change and the fossil fuels. Moreover, the emerging nuclear technologies are designed to address the objectives of an improved sustainability and enhanced safety, which represent the main concerns in the population about the previous generation reactors. For instance, the adoption of closed nuclear fuel cycles associated with partitioning and transmutation techniques and with the new-generation fast reactors and ADS will manage to significantly reduce the amount and the long-term radiotoxicity of nuclear wastes and even burn the wastes from the previous generation reactors. In addition, the efficiency in the utilization of natural resources will be improved breeding the fissile fuel from the more abundant fertile ^{238}U or even ^{232}Th and, in the case of ADS, intrinsic safety will be guaranteed by their operation in a sub-critical regime.

Beyond the field of power production, the study of neutron-induced reactions also plays a relevant role in nuclear astrophysics, where it can help to understand the stellar processes, as well as in medicine, for the production of radioisotopes used in diagnostic and for the improvement of the current hadron-based cancer treatments with Boron Neutron Capture Therapy (BNCT).

The development of all these technologies and applications requires accurate and precise data on neutron cross sections that, especially at high energy, are still missing or known with scarce accuracy and therefore urgently requested by organizations as the OECD (Organization for Economic Cooperation and Development), author of the Nuclear Data High Priority Request List.

The n_TOF facility at CERN plays a central role in providing these data. In fact, thanks to the combination of the excellent energy resolution, the high neutron flux and the unprecedented wide neutron energy spectrum, accurate measurements of neutron-induced reaction cross sections can be performed from thermal energy

up 1 GeV in its two, future three, experimental areas. In particular, EAR1, positioned at 185 m from the neutron source and characterized by an energy spectrum reaching 1 GeV and by an energy resolution $\Delta E/E$ lower than 10^{-3} along nearly all the energy spectrum, is particularly suited for high precision measurements on stable and long-lived isotopes, while EAR2, positioned at 18.5 m from the neutron source, is suitable for measurements on samples available in small quantity, on short-lived radioisotopes and of small cross sections. On the other hand, NEAR will be soon available for neutron irradiation measurements.

The recent upgrade of the facility with the implantation of the new-generation nitrogen-cooled spallation target should guarantee its operations for the next ten years. The subsequent commissioning was a necessary step for the characterization of the performances of the new target in terms of neutron beams and energy resolution in view of the future experimental campaigns.

Entering the details of the first phase of the commissioning, focus of this thesis, it was aimed at the determination of the neutron flux and of the spatial beam profile. In order to cover the whole neutron energy spectrum and possibly correct the systematic uncertainties, three different neutron conversion reactions were used in four different kinds of neutron flux detectors: SiMon, a silicon monitor based on the ^{6}Li(n,t) reaction, MicroMeGaS, a gaseous detector based on the ^{10}B(n,α) and the ^{235}U(n,f) reactions, PTB and PPAC, respectively ionization and proportional gaseous detectors both exploiting the ^{235}U(n,f) reaction (and also the ^{238}U(n,f) reaction in the case of the PPAC in EAR2).

The PPAC Monitor was analyzed in details. This detector is a fission chamber made of three Parallel Plate Avalanche Counters flanking two targets of fissionable material. It allows the detection in coincidence of both the fission fragments produced in fission events, thus significantly reducing the background. Due to the thin gap between the electrodes, PPACs are also characterized by a very fast time response (signal risetime of few ns) and good time resolution (hundreds of ps), while the low gas pressure used implies their insensitivity to long range particles. These characteristics make the detector particularly insensitive to the γ-flash and consequently it is the only one capable of detecting neutron-induced fissions at very short times of flight, corresponding to neutron energies up to 1 GeV. Additionally, thanks to the two stripped cathodes of each PPAC, the detector is capable of localizing the fission fragments with a spatial resolution of 1.4 mm and consequently it also allowed the measurement of the spatial beam profile.

The analysis of the data from this detector in EAR1 was the subject of this work. First of all, the fission events were reconstructed through the selection of the anode signal coincidences between adjacent PPACs and the application of suitable time and amplitude selections. Time considerations were additionally carried out to identify the target where fissions occurred, in case of ambiguity. Secondly, each selected anode signals configuration was completed with the correspond-

ing cathode signals. After the determination of the accurate neutron flight path through the comparison between well-known and measured resonance positions and after a suitable calibration of the signal times through the γ-flash signal, the time information from the anode signals was converted into the corresponding kinetic energy of the detected neutrons. On the other hand, the time information from the cathode signals was converted into the spatial information on the detection position of the fission fragments that, through geometrical calculations, enabled the reconstruction of their trajectory and the determination of the position of the fission reactions in the targets. The two pieces of information were finally combined to study the efficiency of the detector, limited by a cut-off on the fission fragment emission angle with respect to the beam direction. The effect of the anisotropy in the fission fragment angular distribution was also considered studying the efficiency for different neutron energy intervals and finding corrections up to 12% at the energies where the anisotropy is maximum (approximately between 6 MeV and 20 MeV). In the end, the evaluated values for the detector efficiency are found in a range between 48% and 53% for the first target and between 55% and 62% for the second one. Combining all the previous results, the spatial beam profile and the neutron flux were finally determined.

The spatial beam profile resulted rather circular with estimated FWHM of (15.8 ± 1.0) mm and (15.0 ± 1.0) mm in the two directions perpendicular to the incoming neutron beam, slightly decreasing with neutron energy. The comparison with the beam profile obtained from the Timepix Quad detector at high neutron energy (over 100 keV) showed an agreement within 2%.

The neutron flux was evaluated at 50 bins per decade with a statistical uncertainty ranging from about 1% at thermal energy and 5% in the MeV-GeV region and an overall systematic uncertainty estimated at 2%. The consistency of the results obtained separately considering the high-intensity and the low-intensity proton bunches confirmed that no pile-up occurred, therefore dead-time correction are negligible in EAR1. Excluding the resonance region of ^{235}U(n,f) where its cross section is not a standard, the comparison with the Monte Carlo simulation and the preliminary results from SiMon shows a fair agreement on the shape of the neutron flux in the energy range between the thermal energy region and about 1 MeV, with a presence of a scale factor close to one, on average, with respect to the simulation and between 10% and 20% with respect to SiMon. Such constant scale factors are expected in this preliminary phase due to systematic effects related, for instance, to the poor knowledge of the areal density of the samples and of the absolute value of the detector efficiency. However, significant discrepancies, up to 60%, are observed between the results from PPAC and the Monte Carlo simulations for energies below 1 eV and over 10 MeV. At thermal energy, the consistency between the two experimentally measured fluxes (in terms of the shape) may hint problems in the simulations, possibly attributable to a non accu-

rate value for the boron concentration in the moderator. At high energy the reasons for such discrepancies are still not clear.

In addition, following the same procedures, a preliminary analysis was carried out to extract the neutron flux and the spatial beam profile in EAR2, considering only the ^{235}U sample. The spatial beam profile resulted rather circular at low energy with estimated FWHM of (28.8 ± 1.0) mm and (26.7 ± 1.0) mm in the two directions perpendicular to the incoming neutron beam. When the neutron energy is increased, the beam profile gets elongated along the direction of the proton beam incident to the spallation target, that is indeed the direction where the most energetic particles from spallation are emitted. This effect is also confirmed by the beam profiles obtained with the Timepix Quad detectors.

The neutron flux, differently from EAR1, is largely affected by pile-up effects at high energy, where therefore only the events from the low-intensity bunches were considered in first approximation. At 100 bins per decade, the achieved statistical relative uncertainty ranges from less than 0.2% in the thermal region to about 10% in the MeV-GeV region. Except for the ^{235}U(n,f) resonance region, the shape of the flux is consistent with the preliminary results from SiMon and the Monte Carlo simulations in the energy range between some fractions of eV and about 100 keV (1 MeV for the simulations). At higher energies, the large discrepancies are probably due to the pile-up, that still needs to be suitably corrected in a further analysis.

Bibliography

[1] E. Rutherford, "Bakerian Lecture: Nuclear constitution of atoms", Proc. R. Soc. Lond. A 97 (1920) 374-400

[2] E. Rutherford, Phil. Mag. 37 (1919) pp. 538-587

[3] V. Nesvizhevsky, J. Villain, "The discovery of neutron and its consequences (1930-1940)", C. R. Physique 18 (2017) 592-600

[4] W. Bothe, H. Becker, "Künstliche Erregung von Kern–γ–Strahlen", Z. Phys. 66 (1930) 289.

[5] I. Curie, F. Joliot, "Emission de protons à grande vitesse par les substances hydrogénées sous l'influence des rayons γ très pénétrants", C. r. hebd. séances Acad. sci. Paris 194 (1932) 273

[6] J. Chadwick, "Possible existence of a neutron", Nature 129 (1932) 312

[7] J. Chadwick, "The existence of a neutron", Proc. R. Soc. 136 (1932) 692

[8] D. J. Hughes, "Neutron Cross Sections", Pergamon Press (1957)

[9] P. Reuss, "Neutron Physics", EDP Sciences (2008)

[10] N.Bohr, "Neutron capture and nuclear constitution", Nature 137 (1936) 344

[11] N. Bohr, "Transmutation of atomic nuclei", Science 86 (1937) 2225

[12] C. Bertulani, "Nuclear reactions" in "Wiley Enciclopedia of Physics", Wiley - VCH (2009)

[13] M. Kawai, "Nuclear reaction theory", JAERI-Conf 95-008 (1995), Proceedings of the 1994 Symposium on Nuclear Data, 1994, JAERI, Tokai, Japan

[14] G. R. Satchler, "Introduction to nuclear reactions", Macmillan Press LTD (1980)

[15] K. Krane, "Introductory Nuclear Physics", John Wiley & Sons Inc (1988)

[16] L. Meitner and O. Frisch, "Disintegration of uranium by neutrons: a new type of nuclear reaction", Nature 143 (1939)

[17] A. Manna, "Measurement of the ^{235}U(n,f) cross section relative to the neutron-proton elastic scattering up to 500 MeV at n_TOF", PhD thesis, Alma Mater Studiorum Università di Bologna (2021)

[18] E. Segré, "Nuclei and particles", W. A. Benjamin Inc (1965)

[19] H. Feshbach, C. Porter, and V. Weisskopf, "Model for Nuclear Reactions with Neutrons", Phys. Rev. 96 (1954) 448

[20] www.oecd-nea.org/janisweb/

[21] https://www.iea.org/data-and-statistics/

[22] International Energy Agency (IEA), "Nuclear Power in a Clean Energy System", IEA, Paris (2019) https://www.iea.org/reports/nuclear-power-in-a-clean-energy-system

[23] https://www.iea.org/fuels-and-technologies/nuclear

[24] M. Salvatores, G. Palmiotti, "Radioactive waste partitioning and transmutation: achievements and challenges", Progress in Particle and Nuclear Physics 66 (2011) 144–166

[25] Generation IV Forum (GIF): https://www.gen-4.org

[26] https://www.newcleo.com/

[27] https://www.transmutex.com

[28] N. Colonna et al., "Advanced nuclear energy systems and the need of accurate nuclear data: the n_TOF project at CERN", Energy Environ. Sci. 3 (2010) 1910-1917

[29] The High Priority Request List (HPRL), www.oecd-nea.org/dbdata/hprl/

[30] The World Nuclear Organization: https://www.world-nuclear.org

[31] International Atomic Energy Agency (IAEA), "The Use of Nuclear Power Beyond Generating Electricity: Non-Electric Applications", in https://www.iaea.org/newscenter/news/

[32] F. Carminati et al., "An energy amplifier for cleaner and inexhustible nuclear energy production driven by a particle beam accelerator", CERN/AT/93-47-ET (1993)

[33] P. Zhivkov et al., "Accelerator driven system for transmutation and energy production", EPJ Web of Conferences 194 (2018) 08002

[34] `https://myrrha.be`

[35] N. Colonna et al., "The fission experimental programme at the CERN n_TOF facility: status and perspectives", Eur. Phys. J. A (2020) 56-48

[36] n_TOF website: https://ntof-exp.web.cern.ch/

[37] F. Garcia-Infantes et al., "Measurement of the ^{176}Yb(n,γ) cross-section at EAR1 and its application to nuclear medicine", CERN-INTC-2021-037 INTC-P-607 (2021)

[38] E. Chiaveri, "Status and perspectives of the neutron time-of-flight facility n_TOF at CERN", EPJ Web of Conferences 239 (2020) 17001

[39] `https://www.bnct.it/`

[40] M. Bacak et al., "Neutron imaging at the n_TOF facility", EPJ Web of Conferences 239 (2020) 01042

[41] D. Chichester, "Production and Applications of Neutrons Using Particle Accelerators", INL/EXT-09-17312

[42] C. Rubbia et al., "A High Resolution Spallation Driven Facility at the CERN-PS to Measure Neutron Cross Sections in the Interval from 1 eV to 250 MeV", CERN-LHC/98-002-EET (1998)

[43] F. Gunsing et al., "Nuclear data activities at the n_TOF facility at CERN", Eur. Phys. J. Plus 131 (2016) 371

[44] U. Abbondanno et al., "n_TOF performance report", CERN/INTC-O-011, INTC-2002-037, (2002)

[45] M. Calviani, "The n_TOF facility at CERN", in NSTAPP - Neutrons in Science, Technology and Applications, 22 November 2021, CERN, Geneva (CH)

[46] D. Filges, F. Goldenbaum, "Handbook of Spallation Research: Theory, Experiments and Applications", Wiley-VCH Verlag GmbH & Co. (2009)

[47] R. Esposito, M. Calviani, "Design of the third-generation neutron spallation target for the CERN's n_TOF facility", Journal of Neutron Research 22 (2020) 221–231

[48] R. Esposito, "Design of the third-generation lead-based neutron spallation target for the neutron time-of-flight facility at CERN", Phys. Rev. Accel. Beams 24 (2021) 093001

[49] P. Schillebeeckx et al., "Determination of resonance parameters and their covariances from neutron induced reactin cross section data", Nucl. Data Sheets 113 (2012) 3054-3100

[50] C. Guerrero et al., "Performance of the neutron time-of-flght facility at CERN", Eur. Phys. J. A 49 (2013) 27

[51] The n_TOF collaboration, "Commissioning of the third-generation spallation target and neutron beam characteristics of the n_TOF facility", CERN-INTC-2020-072 INTC-P-587 (2020)

[52] C. Weiss et al., "The new vertical neutron beam line at the CERN n_TOF facility design and outlook on the performance", Nuclear Instruments and Methods in Physics Research A 799 (2015) 90-98

[53] The n_TOF collaboration, "the new n_TOF NEAR station", CERN-INTC-2020-073 INTC-I-222 (2020)

[54] A. Bernardes, "The NEAR Station irradiation program", in in NSTAPP - Neutrons in Science, Technology and Applications, 22 November 2021, CERN, Geneva (CH)

[55] A. Masi et al., "The CERN n_TOF facility data acquisition system", in Proc. 16th Int. Conf. on Accelerator and Large Experimental Control Systems (ICALEPCS17) (2017)

[56] P. Žugec et al., "Pulse processing routines for neutron time-of-flight data", Nucl. Instrum. Methods A 812 (2016) 134-144

[57] P. Žugec, "User's guide through Pulse Shape Analysis routines" (2017)

[58] G. Knoll, "Radiation detection and measurement", John Wiley & Sons Inc. (2000)

[59] A. Pietropaolo et al., "Neutron detection from μeV to GeV", Physics Reports 875 (2020) 1

[60] D. Chiesa et al., "Measurement of the neutron flux at spallation sources using multi-foil activation", Nucl. Instrum. Methods A 902 (2018) 14-24

[61] A.D. Carlson et al., "Evaluation of the neutron data standards", Nuclear Data Sheets 148 (2018) 143-188

[62] M. Barbagallo et al., "High-accuracy determination of the neutron flux at n_TOF", Eur. Phys. J. A 49 (2013) 156

[63] M. Sabaté-Gilarte et al., "High-accuracy determination of the neutron flux in the new experimental area n_TOF-EAR2 at CERN", Eur. Phys. J. A 53 (2017) 210

[64] W. Leo, "Techniques for Nuclear and Particle Physics Experiments: A How-to Approach", Springer-Verlag GmbH (1994)

[65] M. Sabaté-Gilarte, "The n_TOF-EAR2 facility at CERN: neutron flux determination and ^{33}S(n,α)^{30}Si cross section measurement", PHD thesis, Universidad de Sevilla (2017)

[66] S. Andriamonje et al., "A transparent detectror for n_TOF neutron beam monitoring", Journal of the Korean Physical Society 59 (2011) 1597-1600

[67] D. B. Gayther, "International Intercomparison of Fast Neutron Fluence-Rate Measurements Using Fission Chamber Transfer Instruments", Metrologia 27 (1990) 221-231

[68] D. Tarrio, "Neutron-induced fission fragment angular distribution at CERN n_TOF: The Th-232 case", PHD thesis, Universidade de Santiago de Compostela (2012)

[69] A. Breskin and N. Zwang., "Timing properties of parallel plate avalanche counters with light particles", Nucl. Instr. and Meth. 144 (1977)

[70] S. Marrone et al., "A low background neutron flux monitor for the n_TOF facility at CERN", Nuclear Instruments and Methods in Physics Research A 517 (2004) 389-398

[71] L. Cosentino et al., "Silicon detectors for the n_TOF neutron beams monitoring" (2015)

[72] S. Andriamonje et al., "Development and performance of Microbulk Micromegas detectors", JINST 5 (2010) P02001

[73] R. Plag et al., "An optimized C_6D_6 detector for studies of resonance-dominated (n,γ) cross-sections", Nuclear Instruments and Methods in Physics Research A 496 (2003) 425-436

[74] A. Borella et al., "The use of C_6D_6 detectors for neutron induced capture cross section measurements in the resonance region", Nuclear Instruments and Methods in Physics Research A 77 (2007) 626-640

[75] X. Llopart et al., "Timepix, a 65k programmable pixel readout chip for arrival time, energy and/or photon counting measurements", Nuclear Instruments and Methods in Physics Research A 581 (2007) 485-494

[76] D. Hensle et al., "Neutron-induced fission fragment angular distributions, anisotropy, and linear momentum transfer measured with the NIFFTE fission time projection chamber", Phys. Rev. C 102 (2020)